University of Luxembourg & University of Cantabria

2020

DISSERTATION

to obtain the degree of

DOCTEUR DE L' UNIVERSITÉ DU LUXEMBOURG

EN PHYSIQUE

DOCTOR POR LA UNIVERSIDAD DE CANTABRIA

by

Mauro António Pereira Gonçalves

Supervisor: Prof. Dr Jorge Íñiguez, University of Luxembourg

Co-supervisor: Prof. Dr Javier Junquera, University of Cantabria

STUDY OF COMPLEX FERROIC OXIDES BY LARGE-SCALE FIRST-PRINCIPLES SIMULATIONS

ESTUDIO DE OXIDOS FERROICOS COMPLEJOS POR SIMULACIONES DE PRIMER PRINCIPIO A GRAN ESCALA

Dissertation Defence Committee:

Committee members:

Prof. Dr Ludger Wirtz, Université du Luxembourg

Prof. Dr Anna Grünebohm, Ruhr-Universität Bochum

Prof. Dr Alessio Filippetti, Università de Cagliari

Dr Jirka Hlinka, Academy of Sciences of the Czech Republic

Expert in an advisory capacity:

A-Prof. Dr Maël Guennou, Université du Luxembourg

Supervisor:

Prof. Dr Jorge Íñiguez, Luxembourg Institute of Science and Technology & Université du Luxembourg

Co-supervisor:

Prof. Dr Javier Junquera, Universidad de Cantabria

Do not alter this page, only fill out the required fields **Affidavit**

I hereby confirm that the PhD thesis entitled xxxxxx has been written independently and without any other sources than cited.

Luxembourg, _____ _____

Name

Acknowledgements

I begin by thanking everyone who has contributed over the years to my academic and personal growth.

Among them, I would like to highlight my supervisors, Prof. Dr Jorge Íñiguez and Prof. Dr Javier Junquera for the trust they placed in me and for the guidance over these years, without which it would have been impossible for me to do this work.

In addition, I would also like to thank Prof. Dr Pablo García-Fernández the help and support over these years, both at the academic level, and with all the constant trips between Luxembourg and Spain.

Agora em Português, de forma um pouco menos formal, gostava de agradecer, em primeiro à minha Mãe, ao meu Pai e ao meu Irmão por toda a ajuda e preocupação, mesmo que nem sempre entendam bem o que eu faço no meu trabalho. Contudo, sem eles nada disto teria sido possível.

Tenho ainda de agradecer, em especial, à Joana M. R. Teixeira que desde o dia em que sai de Portugal esteve sempre presente nos bons e maus momentos, e que foi sem dúvida fundamental (inclusive para manter a minha capacidade de falar Português).

Finally, I would like to thank all the good friends that I have met over the years in Luxembourg and Santander, among which I have to highlight Cosme, Carlos and Javier, not only for all the scientific discussions, but also for all the good times outside the work.

0.1 Summary

The main goal of this thesis was to explore the possibility that ferroelectric materials, characterized by a spontaneous and switchable electric polarization, may present topologically non-trivial structures akin to the skyrmions that occur in their ferromagnetic counterparts. The main tool used in the investigation was atomistic simulation based of first-principles effective models ("second-principles methods"), applied to two model systems: ferroelectric PbTiO3 and ferroelectric/paraelectric superlattices made of $PbTiO_3$ and $SrTiO_3$. More precisely, the simulations were used to analyze multidomain configurations in these compounds, motivated by previous reports that they may present non-trivial structural features. The main finding of the thesis is that, indeed, a simple multidomain configuration in $PbTiO_3$ – namely, a columnar nanodomain with polarization opposed to that of its surrounding matrix – is sufficient to generate a dipole texture – associated to the rotation of the polarization at the domain wall between nanodomain and matrix – with the topology of a skyrmion. This constitutes the first prediction of an electric skyrmion in a simple ferroelectric material. Further, it is shown that the properties and topology of this skyrmion can be tuned by external electric and elastic fields, as well as by temperature, obtaining novel effects such as topological and iso-topological phase transitions. Finally, the investigation of the $PbTiO_3$/$SrTiO_3$ superlattices reveals that the skyrmion structures can be obtained as the ground state solution for such systems. This latter study was developed in the context of a collaboration with experimental groups at UC Berkeley and elsewhere, which led to the first experimental confirmation of electric skyrmions. Hence, in conclusion, the theoretical work in this thesis has been an integral part of the discovery of electric skyrmions in ferroelectric materials.

0.2 Resumen

El objetivo principal de esta tesis es el estudio de las propiedades topológicas no-triviales en sistemas ferroeléctricos mediante simulaciones atomísticas con modelos efectivos de segundos-principios (descritos en el capítulo 2 de la memoria).

Desde hace más de una década se conoce la existencia de texturas magnéticas con una topología no trivial (skyrmiones, merones, hopfiones, etc). Estas estructuras poseen unas propiedades muy llamativas: están protegidas por topología (cuesta una energía destruirlas), y se pueden mover fácilmente con corrientes eléctricas externas lo que las hace candidatas ideales para la fabricación de memorias tipo "pista de carrera" ("race-track memorie"). La fuerza motriz para que aparezcan estas fases no triviales es la presencia de interacciones relativistas quirales tipo Dzyaloshinskii-Moriya, presentes en láminas o interfases magnéticas en la que hay ausencia o ruptura de la simetría de inversión.

Como esta interacción no tiene análogo en sistemas ferroeléctricos, el pensamiento general era que no se podían estabilizar estas texturas con topología no trivial en sistemas polares, caracterizados por la presencia de una polarización espontánea e invertible. Solo en los últimos años se habían mostrados indicios de su existencia en compuestos complejos (nanocolumnas de un material ferroeléctrico de pequeño diámetro embebidas en una matriz dieléctrica), difíciles de caracterizar experimentalmente.

Sin embargo, en la presente tesis se predice teóricamente la existencia de skyrmiones en dos sistemas ferroeléctricos distintos, mucho más sencillos que los anteriores y, por lo tanto, experimentalmente verificables:

- En el caso de un único material (PbTiO3) en el que se puedan escribir nanodominios ferroeléctricos tipo columna con una polarización opuesta a la de la matriz circundante (Capítulo 3 de la memoria). La rotación de la polarización en la pared de dominio entre las dos polarizaciones es la clave para obtener una estructura con una topología no trivial tipo skyrmion. Este hallazgo constituyó la primera predicción de un skyrmion eléctrico en un único material sencillo. Además de predecir su estabilización, en la tesis se dan las claves para poder modificarlo de manera controlada mediante cam-

pos eléctricos, tensiones impuestas por un substrato o por efectos térmicos (temperatura) (Capítulo 4 de la memoria). Se observan distinto tipos de transiciones, tanto skyrmion-skyrmion, como transiciones topológicas entre skyrmiones y sistemas dipolares triviales. Determinadas funciones respuesta (susceptibilidad) divergen en los puntos de la transición.

- En el caso de superredes ferroeléctrico/dieléctrico en las que se intercalan capas de PbTiO3 y SrTiO3 (Capítulo 5 de la memoria). Dependiendo de la tensión epitaxial pueden estabilizarse estructuras tipo vórtice o skyrmiones. En la presente tesis se detallan las condiciones para obtener estas últimas, se procede al análisis riguroso de las propiedades topológicas, y sus propiedades funcionales (susceptibilidades y constantes dieléctricas). Este estudio se ha realizado en colaboración con grupos experimentales de la Universidad de California-Berkeley y la Universidad de Cornell.

La constante retroalimentación entre teoría y experimento ha dado lugar al primer trabajo en el que se observa la estabilización de skyrmiones polares a temperatura ambiente en materiales ferroeléctricos, siendo los cálculos realizados en la presente tesis, una parte integral de los mismos.

Abstract

The main goal of this thesis was to explore the possibility that ferroelectric materials, characterized by a spontaneous and switchable electric polarization, may present topologically non-trivial structures akin to the skyrmions that occur in their ferromagnetic counterparts. The main tool used in the investigation was atomistic simulation based of first-principles effective models ("second-principles methods"), applied to two model systems: ferroelectric PbTiO3 and ferroelectric/paraelectric superlattices made of $PbTiO_3$ and $SrTiO_3$. More precisely, the simulations were used to analyze multidomain configurations in these compounds, motivated by previous reports that they may present non-trivial structural features. The main finding of the thesis is that, indeed, a simple multidomain configuration in $PbTiO_3$ – namely, a columnar nanodomain with polarization opposed to that of its surrounding matrix – is sufficient to generate a dipole texture – associated to the rotation of the polarization at the domain wall between nanodomain and matrix – with the topology of a skyrmion. This constitutes the first prediction of an electric skyrmion in a simple ferroelectric material. Further, it is shown that the properties and topology of this skyrmion can be tuned by external electric and elastic fields, as well as by temperature, obtaining novel effects such as topological and iso-topological phase transitions. Finally, the investigation of the $PbTiO_3$/$SrTiO_3$ superlattices reveals that the skyrmion structures can be obtained as the ground state solution for such systems. This latter study was developed in the context of a collaboration with experimental groups at UC Berkeley and elsewhere, which led to the first experimental confirmation of electric skyrmions. Hence, in conclusion, the theoretical work in this thesis has been an integral part of the discovery of electric skyrmions in ferroelectric materials.

Index

List of Figures

List of Tables

Chapter 1

Introduction

The focus of this thesis will be exotic topological structures in ferroelectric materials. To introduce the topic let me review the basics of ferroelectricity and ferroelectric perovskite oxides and how we can tune their properties.

1.1 Perovskite oxides ABO_3

1.1.1 The structure

The perovskite structure is a simple cubic structure, whose chemical formula is ABO_3. In this structure, atoms A and B are the cations and the atoms of O form an octahedron around the B atom. As we can see in Fig. 1.1 (a), the A atoms occupy the vertices of the cubic structure and atom B is in the center of the unit cell. The atoms of O appear in the center of each face of the unit cell.

This structure, despite being quite simple, presents a wide range of properties depending on the atoms A and B, used for different applications, for example, energy harvesting [9, 10], high-frequency tunable dielectrics [10, 11] or ferroelectric or multiferroic memories [12, 13, 14]. This variety of applications is a consequence of the diversity of deformations to which some of these perovskite oxides may be subject, such as the ferroelectric instability or antiferrodistortive instabilities presented in Fig. 1.1.

In this thesis we will focus on two perovskite materials: PbTiO3 and SrTiO3.

1.1.2 Ferroelectric Perovskite oxides

Some of these perovskites are ferroelectric materials with a spontaneous polarization [15, 16]. In such materials, collective distortions from the ideal perovskite structure are observed involving the relative displacement of the cations (atoms A and B) with respect to the sub-lattice formed by the O atoms (deformation presented in Fig. 1.1 (b)). This distortion is associated with a phase transition, shown in Fig. 1.2 (a), from a high temperature paraelectric phase with an ideal perovskite structure to a low temperature ferroelectric phase. As previously mentioned, in this phase the relative displacement of cations with respect to the O octahedra give rise to a polarization.

In addition to the observed polarization, these ferroelectric perovskites have three more characteristics that are important to mention. The first is related to the dielectric susceptibility around the ferroelectric transition. The susceptibility measures the polarization variation $\mathbf{P}$

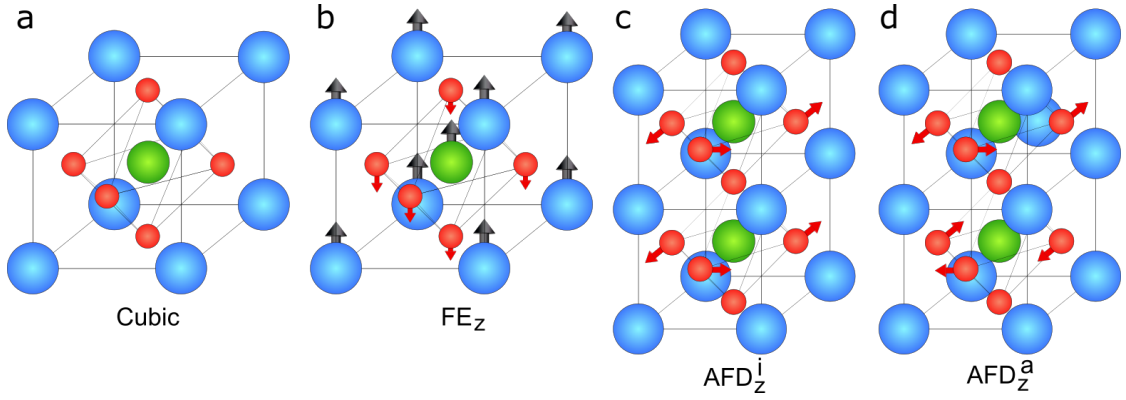

Figure 1.1: Sketch of the most relevant configurations in ABO_3 perovskite oxides. Panel (a) shows the ideal cubic structure of the ABO_3 perovskite; Panel (b) shows the ferroelectric instability (FE_z); Panels (c) and (d) present the antiferrodistortive instabilities with the O_6 octahedra rotation along z in-phase, AFD_z^i (c), and in antiphase, AFD_z^a (d). The arrows represent the atomic displacements.

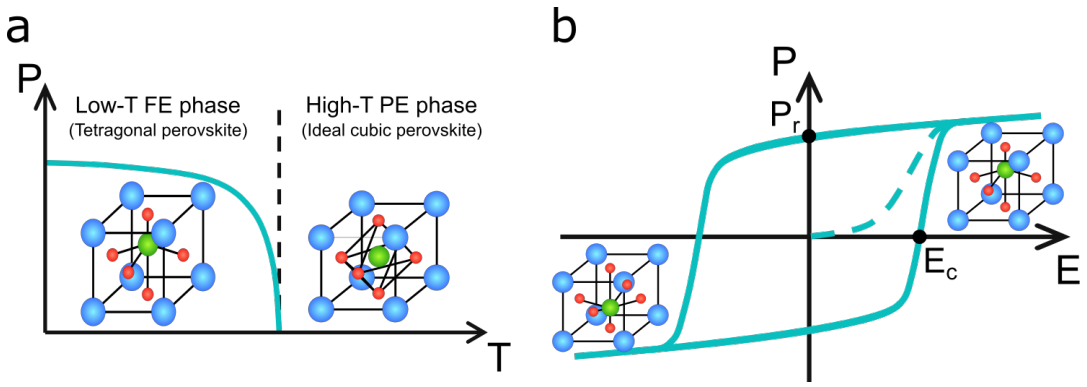

Figure 1.2: Sketch of the ferroelectric transition of a perovskite (a) and the characteristic ferroelectric hysteresis loop of the polarization as a function of electric field (b).

when we apply an external electric field $\boldsymbol{\mathcal{E}}^{\text{ext}}$ according to the expression:

$$\chi_{\alpha\beta} = \frac{1}{\epsilon_0} \frac{\partial P_\alpha}{\partial \mathcal{E}_\beta^{\text{ext}}} \,, \tag{1.1}$$

where ϵ_0 is the vacuum permittivity, and α and β label the spatial components of polarization and electric field. Near the ferroelectric transition, a small electric field produces a huge variation in polarization and therefore a peak is observed in the susceptibility.

As in any other material that is ferroelectric, ferroelectric perovskite must be switchable upon application of an external electric field. In Fig. 1.2 (b) we show the P–E hysteresis loop, consequence of this property. This loop is obtained by applying a positive electric field, increasing the polarization to its maximum (saturation of the polarization). Then we reduce the electric field until it is null and, at this point, we obtain the remnant polarization P_r. Then, we apply negative fields with increasing magnitude until we reach the negative saturation polarization. During this part of the cycle there is a point where the polarization is zero. The magnitude of the electric field at this point is called the coercive field, E_c. Finally, we complete the cycle by increasing the external electric field again.

Finally, all ferroelectric perovskites are also piezoelectric, which implies that when subject to an external electric field, the material undergoes a strain variation. The piezoelectric

coefficients $d_{\alpha\gamma}$ are the key quantity in piezoelectric materials and it is given by:

$$d_{\alpha\gamma} = \left(\frac{\partial \eta_\gamma}{\partial \mathcal{E}_\alpha^{\text{ext}}} \right) \Bigg|_\sigma , \tag{1.2}$$

where η_γ is the strain component in Voigt notation where $\gamma = 1, ..., 6$, α labels the spatial component of the electric field and σ is the external stress.

Several examples of ferroelectric perovskites can be found in the literature showing different competing instabilities and different transition sequences.

$BaTiO_3$

One of the most studied perovskites at the experimental and theoretical level is $BaTiO_3$ [17, 18], which at high temperatures has a cubic structure, but when decreasing the temperature a series of transitions is observed. The first phase obtained is a tetragonal phase where the polarization points along a $\langle 001 \rangle$ direction. When the temperature decreases, the polarization rotates now pointing along a $\langle 011 \rangle$ direction which corresponds to a new transformation from a tetragonal to an orthorhombic phase. Finally, at very low temperatures $BaTiO_3$ presents a final transition to a rhombohedral phase in which the polarization rotates towards a $\langle 111 \rangle$ direction. In this material, the polarization direction is dominated by the Ti displacements and the obtained polarizations are 33 μC/cm^2, 36 μC/cm^2 and 27 μC/cm^2 for the tetragonal, orthorhombic and rhombohedral phases, respectively [19, 20]. Other perovskites such as $KNbO_3$ present the same sequence of transitions.

$PbTiO_3$

Another widely studied perovskite is $PbTiO_3$, which presents only a paraelectric-ferroelectric transition, in which at low temperatures a ferroelectric tetragonal phase with a polarization of 75 μC/cm^2 was observed [21, 22]. The polarization in $PbTiO_3$ is dominated by the displacements of Ti and Pb atoms with respect to the O atom sub-lattice. Therefore, the polarization obtained for $PbTiO_3$ is much higher than that obtained in the different phases of $BaTiO_3$.

$SrTiO_3$

In the case of $SrTiO_3$, it presents not only a ferroelectric instability but also antiferrodistortive instabilities. In this material, at low temperatures, an antiferrodistortive transition was observed [23, 24], with the rotation of the oxygen octahedra. Because the antiferrodistortive and ferroelectric instabilities compete, the condensation of the former suppresses the ferroelectric instability, which is never observed. For this reason, $SrTiO_3$ is sometimes called an incipient ferroelectric. Perovskites like $CaTiO_3$, $GdFeO_3$ or $DyScO_3$ are other examples of materials in which the oxygen octahedra rotations are observed, even if some of these materials present different rotation patterns.

Applications

Now that we have shown some of the main properties of ferroelectric materials, we will show how they are used in different applications. In the case of non-volatile ferroelectric random access memories [12, 13, 14], these are based on the ability of ferroelectric materials to change their direction of polarization between two stable states to which values 0 or 1 are associated. Then, applying a short voltage pulse, it is possible to write new information by changing the polarization. The fact that ferroelectric materials present their polarized state even in the absence of a voltage makes these ferroelectric memories non-volatile.

Ferroelectric-based actuators, sensors and transducers [10, 11] take advantage of the piezoelectricity of ferroelectric materials. Thus, ferroelectric sensors are widely used to detect voltages in the system by measuring the electric displacement field. The actuators are used to alter or impose a state on the system using piezoelectricity. In this case, high voltage conditions with high force are required, for example to start engines or control fuel injection.

1.1.3 Structural domain walls

Ferroelectric perovskite oxides offer another possibility for the construction of new technologies at the nanoscale, the structural domain walls [25, 26, 27].

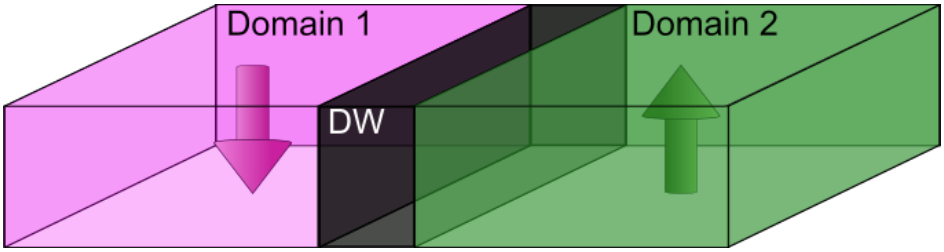

Figure 1.3: Sketch of the ferroelectric multidomain configuration, in which the green and magenta regions represent the domains with polarization up and down respectively, and the black region is the domain wall.

As mentioned above, ferroelectric perovskite oxides are characterized by a break in symmetry due to a structural distortion (which we presented earlier in Fig. 1.1 (b)) that deforms the ideal cubic perovskite phase and this deformation can be switched applying an external electrical field as illustrated in Fig. 1.2 (b).

Thus, in these ferroelectric materials, structural distortions can be oriented differently in distinct regions of the material creating what we call domains with different polarizations. As we show in Fig. 1.3, separating these domains there is a region called domain wall. These walls of the ferroelectric domains tend to be almost two-dimensional objects with a width of few unit cells [26]. These domain walls are generally produced spontaneously in ferroelectric materials during a ferroelectric transition or during the switching process of the polarization. In addition, in several cases the domain walls can be created, moved, erased and even injected [28, 29, 30, 31] using different strategies and means thus allowing devices to be controlled and manipulated.

Until now we have not discussed the intrinsic properties of the domain walls. Since it is an almost two-dimensional object confined between two domains with different properties and subject to different stress conditions, the domain walls in many cases have different properties than those observed in the domains. One of the most interesting examples was observed in WO_3 – which is not a perovskite – in which the domain walls are superconducting, which is not the case in the domains [32]. $BiFeO_3$ domain walls are one of the systems that has attracted the most attention. In this perovskite the domains are insulating, however, it was demonstrated that in the domain walls high conductivity is observed at room tempera-

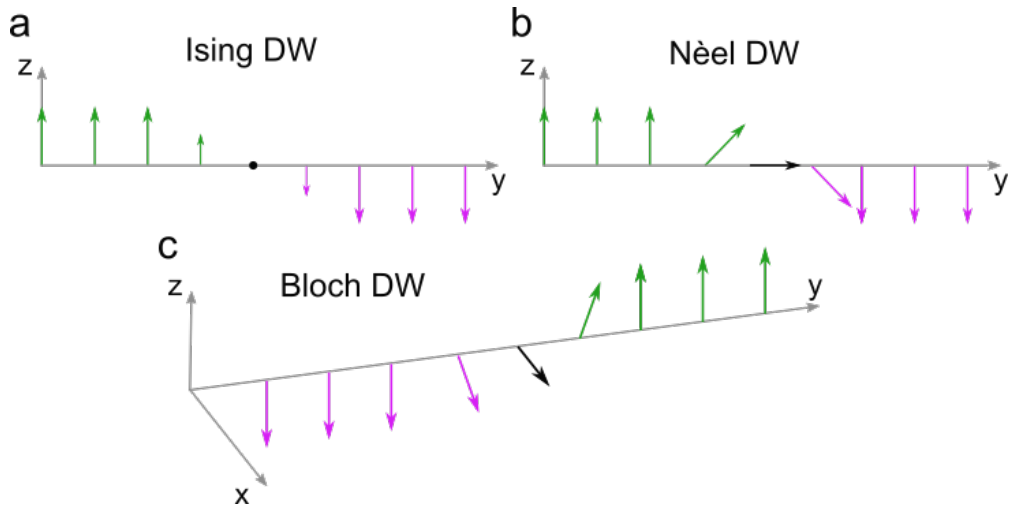

Figure 1.4: Sketch of the possible characters of 180° domain walls, in which we show the evolution of the polarization inside the wall. In panel (a) we show Ising domain walls; panel (b) we have the Néel domain wall; In panel (c) we present the Bloch domain wall.

ture [33, 34]. In the case of $SrTiO_3$, as described above, the domains do not have any polar order, however their domain walls are ferroelectric [35, 36, 37, 38].

Domain walls in $PbTiO_3$

$PbTiO_3$'s domain walls are still among the most studied and play an important role in the work developed in this thesis. Therefore, we will focus on the main advances reported in the literature in the study of these walls concerning: (i) what is their internal structure? and (ii) how does the order parameter (polarization) evolve along the domain wall?

In the beginning of the century, two studies were published defining the guidelines for the study of the structure of domain walls [39, 40], more specifically the ideal and neutral 180° domain walls of $PbTiO_3$. Both studies used first-principles methods to study these structures and they concluded that: (i) these walls are very thin objects with a thickness of about one unit cell and (ii) these walls are centered on the Pb-O planes (the walls centered on the Ti-O planes are unstable).

However, these studies differed in the predicted character of the domain walls. In Fig. 1.4 we show the three different characters that 180° domain walls can present. Fig. 1.4 (a) is an

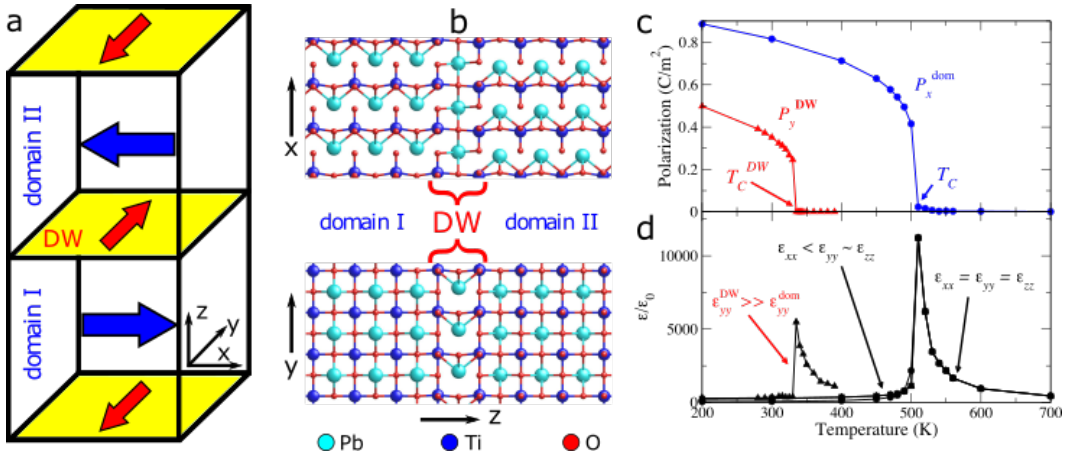

Figure 1.5: (a) Sketch of the supercell used in the simulations with the distortions in the domains and domain walls. Panel (b) shows two views of the atomic structure of our multi-domain configuration. Panels (c) and (d) show the temperature dependent polarization and diagonal components of the dielectric permittivity tensor for the domains and domain walls. The blue circles represent the polarization obtained in the center of the domains and the red triangles are the results at the center of the domain walls. In the case of the dielectric permittivity the circles represent the response of the domains and the triangles are the results of the domain walls. Figure taken from [1]

Ising wall in which the polarization only changes along one direction and is zero within the domain wall between the domains with opposite polarization. In the case of the Néel domain wall, shown in Fig. 1.4 (b), the polarization rotates in a plane perpendicular to the plane of the domain wall. In Fig. 1.4 (c) we show the Bloch domain wall, in which the polarization inside the domain wall is perpendicular to the polarization in the domains and parallel to the domain wall plane. Meyer and Vanderbilt [40] obtained that the domain walls have an Ising character, while Pöykkö and Chadi [39] predicted that the walls have a Bloch character.

More recently in 2014 Wojdeł and Íñiguez [1] studied the same system using first-principles methods and effective potentials, confirming the Bloch character of the domain walls as we can see in Fig. 1.5 (a) and (b). The character of the wall of domains in $PbTiO_3$ has been confirmed experimentally in several works [7, 8].

In addition, in the work of Wojdeł and Íñiguez [1] the behavior of the multidomain configuration was also studied as a function of temperature, suggesting the existence of two transitions, presented in Fig. 1.5 (c) and (d). The first is associated with the ferroelectric

transition in the domains previously described. And around $T = 320$ K they identified a second transition due to the appearance of a polarization confined to the domain wall and the respective peak in the dielectric response.

1.2 Optimization of ferroelectric perovskites

As we mentioned above ferroelectric perovskites are very sensitive to external perturbations, which we can use to our advantage because it allows us to optimize their properties. Here we will discuss some of the basic ways of doing this, in particular the most relevant to this thesis.

1.2.1 Hydrostatic pressure

Perovskite oxides are materials that are very sensitive to deformations or external stresses. In this section we will analyze the effect of hydrostatic pressure (the same pressure is applied across all directions).

When applying positive hydrostatic pressure, the volume of the unit cell and the interatomic distances are reduced and therefore different instabilities are observed in the material.

In the case of $PbTiO_3$, when the hydrostatic pressure is increased at low-temperatures the following sequence of phases was obtained Tetragonal-Monoclinic-Rhombohedral-Cubic, in which the cubic phase is stabilized for pressures above 22 GPa [41]. This result suggests that the increase in hydrostatic pressure suppresses the ferroelectric instability, however, studies at higher pressures [42, 43] revealed the stabilization of an antiferrodistortive distortion accompanied by the rotation of the oxygen octahedra. With the stabilization of this phase, the appearance of a polar distortion was verified, giving rise to a new ferroelectric phase at high pressures.

Íñiguez and Vanderbilt studied the behavior of $BaTiO_3$ when increasing the pressure using a first-principles-based effective potential [44]. The results at low temperatures sug-

gest that the increase in hydrostatic pressure gives rise to the sequence of Rhombohedral-Orthorhombic-Tetragonal-Cubic phases, consistent with experimental determinations.

The effects of negative hydrostatic pressure have also been studied. In the case of $PbTiO_3$ [45] an abrupt transition is found for pressures around -5 GPa, with the observation of a supertetragonal structure with a ratio $c/a = 1.21$ and an increase in polarization. The same behavior was observed in the case of $BaTiO_3$, but in this case the transition was observed for pressure values around -11 GPa.

1.2.2 Thin films and epitaxial strain

With the recent advances in the synthesis and oxide deposition techniques, in the last decade, the interest of the scientific community in the study of thin films has increased.

As we have shown in the section above, perovskite oxides are extremely susceptible to external stresses or strains. The same can be seen in thin films. These structures are formed by a very thin layer of a material deposited on top of a substrate with a much greater thickness than the film. In this way, in epitaxial thin films, the substrate imposes its in-plane lattice constant on the film, changing its properties [46, 47]. Note that in these epitaxial thin films the strain is applied only in-plane, unlike what happens with the hydrostatic pressure, which is the same across all directions.

Using the appropriate substrate it is possible to obtain ferroelectric SrTiO3 at room temperature [48]. In the cases of PbTiO3 [49, 50] or BaTiO3 [51] using different subtractes it was possible to increase and manipulate the polarization and transition temperatures. In addition, it was also possible to stabilize new phases that are not observed in the bulk material.

In addition to the effect of epitaxial strain, it is important to take into account three more factors, especially important in ultra-thin films: (i) the effect of surfaces where the chemical environment is different; (ii) the electrostatic effect that can be very important when the polarization in the film is perpendicular to the surface leading to the depolarization fields that can in some cases suppress the polarization or force the material to break in domains in order to minimize the associated energy penalty; (iii) the effect of the interface between the substrate and the film in which the symmetry break can lead to the appearance of new

properties or the appearance of depolarization fields.

1.2.3 Superlattices

Another way to control the properties of perovskites is by building superlattices. These structures are built by depositing layers of two or more materials periodically on top of a substrate. As in the case of thin films, in superlattices the substrate imposes its in-plane lattice parameters on the different layers. In addition to the effect of epitaxial tension, in superlattices with thin layers the effects of interfaces and electrostatic interaction between the different materials become more relevant to define the final state of the heterostructure.

In the literature several studies show unexpected behaviors in superlattices. For example in $BaCuO_2/SrCuO_2$ superlattices, superconductivity was observed, even though none of the materials is itself superconductor [52], or in superlattices of $SrZrO_3$ and $SrTiO_3$ that show ferroelectricity when none of these materials is ferroelectric [53] and in $LaAlO_3/SrTiO_3$ superlattices, at the interface a two-dimensional electron gas was observed, even though both materials that form the interface are insulators [54]. $BaTiO_3/SrTiO_3$ superlattices show an increase of more than 50% in the polarization magnitude (compared to the polarization of bulk $BaTiO_3$) due to the epitaxial strain constraints and when constructed with the appropriated thickness of the different layers.

$PbTiO_3/SrTiO_3$ superlattices have been widely studied at the theoretical and experimental level with the discovery of 180° stripe domains with polarization vortices around the domain walls [3, 4, 55, 56, 57].

In Chapter 5 we give a more detailed explanation of the different factors to consider in order to understand the behavior of different superlattices.

1.2.4 Nanoparticles

So far, we have mentioned heterostructures formed by almost two-dimensional materials, but in this section we will briefly describe the studies and some advances in ferroelectric nanoparticles.

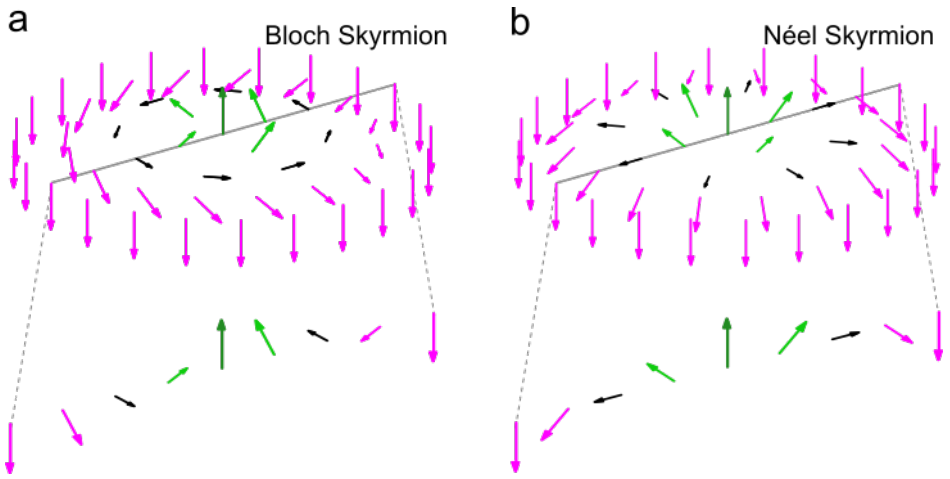

Figure 1.6: Sketches of a typical Bloch-like (a) and Néel-like (b) skyrmions. The arrows represent the normalized magnetization or local electric dipoles.

The size effects were studied in $PbTiO_3$ nanoparticles [58, 59]. The formation of 90° domains in particles larger than 20 nm was predicted. When the size of the nanoparticles is reduced, they undergo a transition to a monodomain phase and finally, for particles smaller than 10 nm, the ferroelectric state is unstable. These results reveal that the effects of size play a fundamental role in the ground state of ferroelectric nanoparticles.

Theoretical studies using first-principles-based effective potentials revealed the formation of polarization vortices in $BaTiO_3$ [60] and $Pb(Zr,Ti)O_3$ [61] isolated nanoparticles. These studies show that these polarization patterns can be manipulated by applying electric fields. The authors suggest that these nanoparticles can be used for storage of information taking into account that the polarization vortices can rotate clockwise or counterclockwise.

1.3 Skyrmions

Skyrmions were initially proposed by Tony Skyrme in an attempt to explain the stability of subatomic particles [62]. In the last few decades, skyrmions have become one of the most relevant and exciting subjects in Condensed Matter Physics, due to their potential for future applications in magnetic systems (so far) [63, 64, 65, 66]. A skyrmion behaves like a particle with a nanometric size and therefore it can be created, moved or annihilated. In Fig. 1.6

we show the typical arrangements of skyrmions, in which in the center of the skyrmions the vectors point up and it is surrounded by vectors pointing down. Between these two regions the vectors rotate forming either Bloch or Néel skyrmions as we show in Fig. 1.6.

These objects are characterized by an integer topological charge (also called Pontryagin invariant) given by:

$$Q = \frac{1}{4\pi} \int \mathbf{u} \cdot (\partial_x \mathbf{u} \times \partial_y \mathbf{u}) dx dy \ , \tag{1.3}$$

where $\mathbf{u}$ is the normalized vector field – is given by $\mathbf{u} = \mathbf{v}/|\mathbf{v}|$ and $\mathbf{v}$ can be the magnetization in magnetic systems or the polarization in ferroelectric materials as we will see in the next sections. When the topological charge is an integer charge and is different from zero the vector field is topologically protected, which implies that these arrangements are local minima of the energy, and a barrier must be overcome to destroy the skyrmion.

1.3.1 Skyrmions in magnetic materials

Magnetic skyrmions have been discovered in materials where the competition between Dzyaloshinskii-Moriya interactions and ferromagnetic exchange is observed [67, 68, 69]. The Dzyaloshinskii-Moriya interaction favors the rotation of the magnetization (with an angle of 90°), while the interaction of ferromagnetic exchange favors the parallel alignment of the spins. As result of this competition and with the application of external magnetic fields, magnetic skyrmions were stabilized with a size between 3 and 100 nm.

In other materials with competition between magnetic dipole interaction and easy-axis anisotropy the formation of magnetic skyrmions was also observed [69, 70]. These skyrmions were stabilized in thin films, in which the ferromagnetic material is subject to perpendicular anisotropy with an easy axis, which favors magnetization perpendicular to the direction of the film, while the magnetic dipole interaction favors in-plane magnetization. Finally, by combining this frustration with an external magnetic field normal to the thin film plane, skyrmions were obtained. However, these skyrmions tend to be much larger with dimensions that can vary from 3 to 100 μm.

1.3.2 Skyrmions in ferroelectric materials

In the last few decades, the search for an electronic analogue of magnetic skyrmions has attracted the attention of the scientific community working with ferroelectric perovskites, since these materials are rich in competing interactions [15, 16]. However electric skyrmions in single-phase ferroelectrics have not yet been discovered.

To understand the absence of an electronic analogue of magnetic skyrmions, we must identify the main differences between the spins and electric dipoles that will form the electric skyrmion. When we look at its origin, in the case of electric dipoles, as we discussed earlier, they are the result of a polar distortion of the lattice. The amplitude of this distortion can vary continuously and consequently the electric dipoles can be reduced continuously until they are destroyed. In the case of spins, these are the consequence of unpaired electrons, such that the total spin is different from zero. In this way spins can change their direction by forming vortices or skyrmions as we mentioned earlier, but their amplitude cannot be continuously reduced until it is null.

In addition to these differences between the nature of spins and electronic dipoles, another factor may also have hindered the discovery of electric skyrmions. As mentioned earlier, in magnetic skyrmions of smaller dimensions, the Dzyaloshinskii-Moriya interaction has a fundamental role, however, there is no analogous electrical interaction in ferroelectric materials.

This way, Nahas and coworkers [2] opted for a different approach that allowed them to predict an electric skyrmion in complex artificial nanostructures. They studied the polarization behavior on a $BaTiO_3$ ferroelectric nanowire with a radius of 7 unit cells within a $SrTiO_3$ paraelectric matrix, as shown in Fig. 1.7 (a). In these nanostructures the two materials will exhibit two very different behaviors, on the one hand the energy of $BaTiO_3$ decreases when developing a polarization, while $SrTiO_3$ prefers to remain with a zero polarization. As a consequence of this frustration inside $BaTiO_3$ they identified a non-zero polarization component parallel to the infinite direction of the nanowire, combined with a vortex structure in the plane formed by four 90° domains (Fig. 1.7 (b)). These 90° domains in-plane ensure that the total polarization in-plane is zero or very close to zero and therefore the depolarization fields and

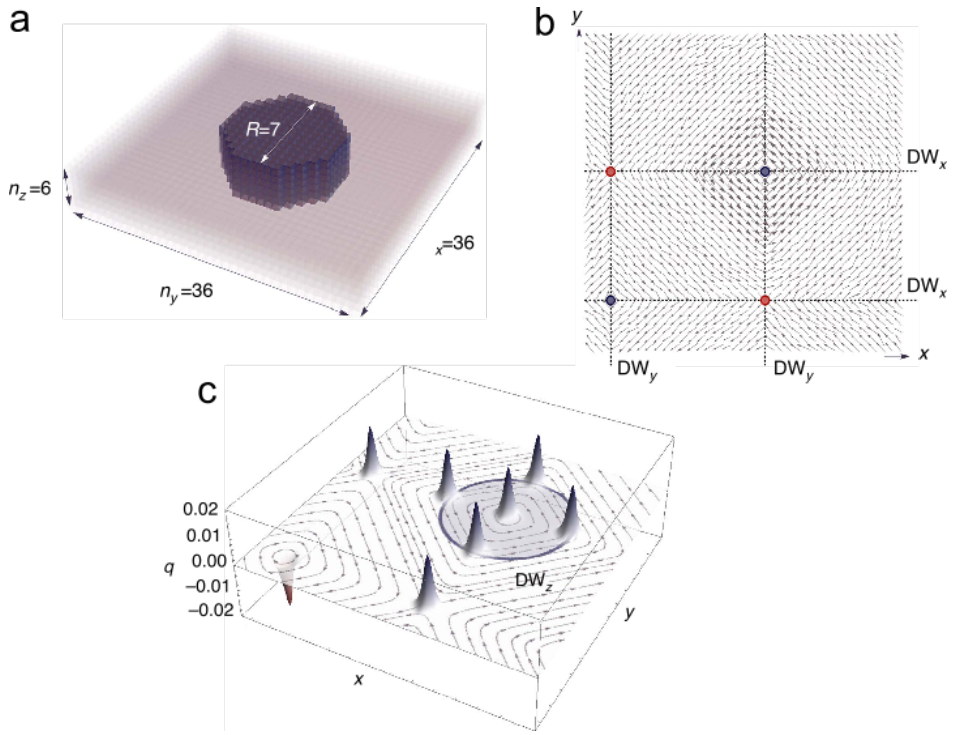

Figure 1.7: Sketches of $BaTiO_3$ nanowire in a $SrTiO_3$ (a) matrix; Electric dipoles (b) and Topological charge density (c) obtained in a xy plane. In the panel (b) the arrows show the polarization in the plane and the black lines show the different domain walls; In the panel (c) the arrows show the vector field obtained from the electric dipoles obtained. These figures were taken from the reference [2].

the electrostatic costs are minimized.

In Fig. 1.7 (c) we show the results that they obtained for the topological charge density along the nanowire configuration where a set of peaks were identified in the center of the different vortices of the in-plane polarization and four more peaks the interface between $BaTiO_3$ and $SrTiO_3$. They obtained a topological charge of $Q = +1$ and thus they predicted the first electric skyrmion in a nanowire configuration combining a ferroelectric material and a paraelectric material [2].

However, until now this prediction has not been proven experimentally, especially due to the difficulty in producing these nanowires with the necessary precision. Furthermore, although these results are encouraging in the search for electric skyrmions, in this case they are based on complex nanostructures, which limit the properties of skyrmions for future

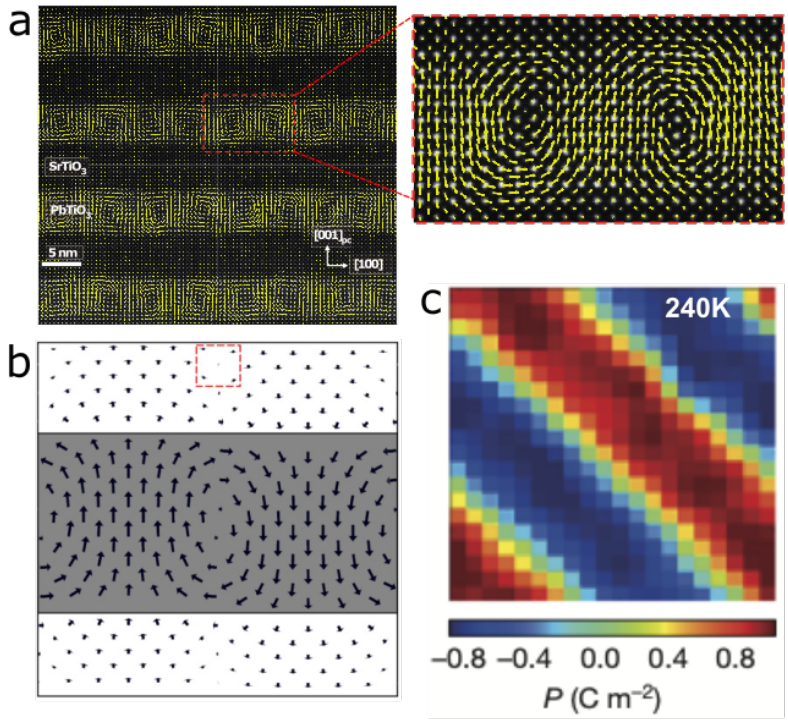

Figure 1.8: Panel (a) shows a cross-sectional HR-STEM image with an overlap of the atomic polar displacements (yellow arrows) for a superlattice of $PbTiO_3$/$SrTiO_3$, with the first experimental evidence of a multidomain structure formed by vortex-antivortex pairs inside the $PbTiO_3$ layers. Panel (b) presents the local polarization profile of the multidomain structures in $PbTiO_3$/$SrTiO_3$ superlattices obtained from first-principles calculations with vortices of polarization around the domain walls and with the rotation of the polarization at the interface. In panel (c) we present the local out of plane polarization in the middle of the $PbTiO_3$ layer in a $PbTiO_3$/$SrTiO_3$ superlattice, obtained using second-principles calculations for a snapshots at 240 K. The figure gathers several results in the literature presented in references [3, 4, 5]

applications.

Another approach can be followed in the search for electric skyrmions taking advantage of recent discoveries in the study of structure and polarization arrangement within domain walls [1] and the tendency of some ferroelectric materials to break down into small domains when subject to appropriate electrostatic conditions.

Recent studies suggest where to find these conditions, for example, mediating nucleation [71] or alternating [72] of ferroelectric domains. In addition, as mentioned above, fer-

roelectric vortex and other exotic behaviors were predicted and observed experimentally in superlattices formed by $PbTiO_3$ or $PbZr_{1-x}Ti_xO_3$ and $SrTiO_3$ [3, 4, 5, 55, 73] as we can see in Fig 1.8, suggesting that exotic structures such as skyrmions may be stabilized.

In this thesis we will follow this approach in an attempt to stabilize and study electrical skyrmions in ferroelectric materials.

1.4 Goals and structure of this thesis

Bearing in mind the general vision that we have presented throughout this chapter, we will now define the main objectives that we intend to achieve with this work and the way in which this thesis is organized.

Our main goal is to investigate if we can have topological structures in simple ferroelectrics using atomistic simulations.

In case we are able to predict such topological structures, our second objective is to understand their behavior and how we can tune them using external fields such as electric fields or strains. Finally, our last goal is to try to predict how they can be achieved in practice in realistic conditions.

This thesis is organized as follows. In Chapter 2, we briefly describe some of the main theoretical approaches that have been used in the study of materials and multidomain configurations, identifying their main advantages and disadvantages. Subsequently, we describe the second-principles methods (implemented in the SCALE-UP package [6, 74]) and the main results achieved using this method. Throughout this thesis we will use the second-principles methods to achieve the different objectives previously described.

In Chapter 3, we show the study of the low temperature nanodomain configuration in $PbTiO_3$, presenting in detail the polarization arrangement and demonstrating that this configuration corresponds to an electric skyrmion. In a second part, we show how to manipulate and optimize the properties of this configuration considering different epitaxial constraints and the effect of applying external electric fields.

In Chapter 4, we present the study of the stability of the nanodomain configuration when

we heat the system. In addition, we carry out the study of the dielectric responses identifying the different transitions in this system, in order to approximate our studies to the type of measurements that can be more easily performed experimentally.

Finally, in Chapter 5, we study the topological properties of the bubble domains in $PbTiO_3$/ $SrTiO_3$ superlattices. These results are further compared with the experimental results obtained in parallel to ours.

Chapter 2

Second-principles methods

In this chapter, we present second-principles methods with parameters obtained from first-principles, in which the energetics of a material is described by expanding in a Taylor series of the total energy around a reference structure taking into account all the atomic degrees of freedom. In this chapter, we start by reviewing several theoretical approaches with their advantages and disadvantages. After, we describe the second-principles methods, implemented in the SCALE-UP package [6, 74]. First, we describe the reference structure and the appropriate variables for the models. In the second part, we describe the different terms of the Taylor expansion of the energy and the main approximations applied to construct the models. Finally, we present the main results reported in literature using the second-principles methods in the study of $PbTiO_3$, $SrTiO_3$ and complex superlattices of $PbTiO_3$/$SrTiO_3$.

2.1 Theoretical approaches

Traditionally, theoretical methods have been used to predict and understand the different properties of material in order to complement the experimental techniques or overcome their limitations. Thus, we want a method that allows us to investigate the different properties of interest under realistic conditions, which can be used to study new materials, obtaining not only the global properties, but also the details on the atomic scale relevant to investigate in

detail multidomain configurations, domain walls or interfaces, which are very difficult to study experimentally.

2.1.1 First-principles methods

In this context, first-principles methods (like density functional theory DFT) are one of the most widely applied methods in the study of materials. This method describes the properties of a material, applying quantum mechanical theory to determine the total energy associated with its electrons and nuclei. The total energy is minimized with respect to the nuclei and electrons coordinates. This consists in a complex many-body problem of interacting particles. Then, in practice several approximations are used to simplify this problem. The first is the Born-Oppenheimer approximation, in which is performed the separation between the nucleus and the electron wave functions taking into account the difference in mass between them. The implementation of this simplification reduces the complexity of the many-body problem, to the study of interacting electrons moving in a configuration of frozen nuclei. So, we can write the Schrödinger equation as:

$$E\psi(\mathbf{r}_1, ..., \mathbf{r}_N) = \sum_i \Big(- \frac{\hbar^2 \boldsymbol{\nabla}_i^2}{2m} + v_{ext}(\mathbf{r}_i) + \sum_{i<j} v_{ee}(\mathbf{r}_i, \mathbf{r}_j) \Big) \psi(\mathbf{r}_1, ..., \mathbf{r}_N) \tag{2.1}$$

where $\psi(\mathbf{r}_1, ..., \mathbf{r}_N)$ is the electronic wavefunction, N is the number of electrons, m is the electron mass. The term $\frac{h\boldsymbol{\nabla}_i^2}{2m}$ is the kinetic energy operator, v_{ext} is the external potential created by the configuration of frozen nuclei and external electric fields and the term v_{ee} correspond to the electron-electron Coulombic interaction. However, even with this simplification, the interacting electron system remains a very complex problem. Thus, density functional theory was proposed by Hohenberg, Kohn [75] and Kohn, Sham [76] providing a simpler method of treating the interactions between the electrons. In DFT the energy of the electron gas is a unique functional of the electronic density. So the total energy can be written as

$$E[n] = T[n] + T_c[n] + U[n] + U_x[n] + V_{ext}[n] \tag{2.2}$$

where n is the electronic density, $T[n]$ is the sum of kinetic energy of the single particles, $T_c[n]$ is the correlation energy, $U[n]$ is the sum of the electron-electron Coulombic interactions, $U_x[n]$ is the exchange energy and $V_{ext}[n]$ is the external potential created by the configuration of nuclei and external electric fields. Finally, Kohn and Sham introduced another simplification by proving that the interacting electronic system can be solved as a system of non-interacting electrons moving in an external potential, obtaining the same ground-state electronic density. Then, the Schrödinger equation for a non-interacting electron is given by:

$$E\psi(\mathbf{r}) = \Big(-\frac{\hbar^2 \boldsymbol{\nabla}^2}{2m} + v_{ext} + v_{ee} + v_{xc} \Big) \psi(\mathbf{r}) \tag{2.3}$$

where v_{xc} is the exchange-correlation potential. This way, the complex problem of many-bodies can be solved as a set of one-particle equations describing the behavior of each electron in an effective external potential. However, none of these theorems give any information about the explicit form of the functional. In practice, to approach such functionalities, several strategies have been developed such as Local-density approximations (LDA) [76] and generalized gradient approximations (GGA) [77].

These methods have been very successfully applied in the study of different materials with high accuracy in the determination of the properties. In addition, being a method based on the fundamental equations of quantum mechanics, it can be applied in the study of new materials showing a high predictive power and provides an understanding of the system at the atomic scale.

However, even with all the simplifications in DFT, this method continues to present a prohibitive computational cost to compute the time and scale length relevant to study some properties of interest at realistic conditions. Moreover, as shown in the Chapter 1 the ferroelectric properties depend strongly on temperature presenting structural phase transitions. Then, to study these materials and compare with the experimental results it is important to study the different properties at finite temperature, which is not accessible using DFT, since random thermal fluctuations require large simulation boxes to obtain realistic results.

2.1.2 Effective Hamiltonian methods

During the 1990's another approach called effective Hamiltonian was applied in the study of $BaTiO_3$ [18, 78], a prototype ferroelectric perovskite.

The effective Hamiltonian method is based on a drastic simplification of the material retaining only the main degrees of freedom to describe the properties and the phase transitions. After identifying the relevant degrees of freedom, it is performed the expansion of the energy of the material. The coefficients of the expansion are computed from first-principles calculations and the precision can be improved in a well-defined way.

In the case of ferroelectric perovskites like $BaTiO_3$ [18, 78], $PbTiO_3$ [79] or $BiFeO_3$ [80, 81], a good approximation to describe the phase transition is to consider only the ionic degrees of freedom of the soft-mode responsible for the ferroelectric transition (with the displacement of the cations with respect to the oxygen sub-lattice) defined as a 3D vector associated to each perovskite unit cell, as shown in Fig. 2.1. The amplitude of this ferroelectric distortion is relatively small, therefore the energy can be expanded around the high-symmetry cubic perovskite structure in terms of local dipole ξ_i associated to the unit cell i and homogeneous strains $\boldsymbol{\eta}$, according to

$$\mathcal{H}(\{\xi_i\},\boldsymbol{\eta}) = \mathcal{H}^{ions}(\{\xi_i\}) + \mathcal{H}^{elast}(\boldsymbol{\eta}) + \mathcal{H}^{int}(\{\xi_i\},\boldsymbol{\eta}) \tag{2.4}$$

The first term $\mathcal{H}^{ions}(\{\xi_i\})$ describes the energy changes due to the variation of the local mode. The term includes the short-range interactions and the long-range dipole-dipole interactions. The short-range part also includes the fourth-order anharmonic terms required to properly describe the potential energy surface of the materials . The second term $\mathcal{H}^{elast}(\boldsymbol{\eta})$ is the elastic energy of the material and describes the energy changes as a function of the homogeneous strain. Finally, the last term $\mathcal{H}^{int}(\{\xi_i\},\boldsymbol{\eta})$ is the energy coupling between the ξ_i and $\boldsymbol{\eta}$.

This method was successfully applied in the study of ferroelectric perovskites. In the cases of $BaTiO_3$ [18, 78] or $PbTiO_3$ [79] or $BiFeO_3$ [80, 81] these models were able to reproduce the experimental sequence of phase transitions and the main properties of the

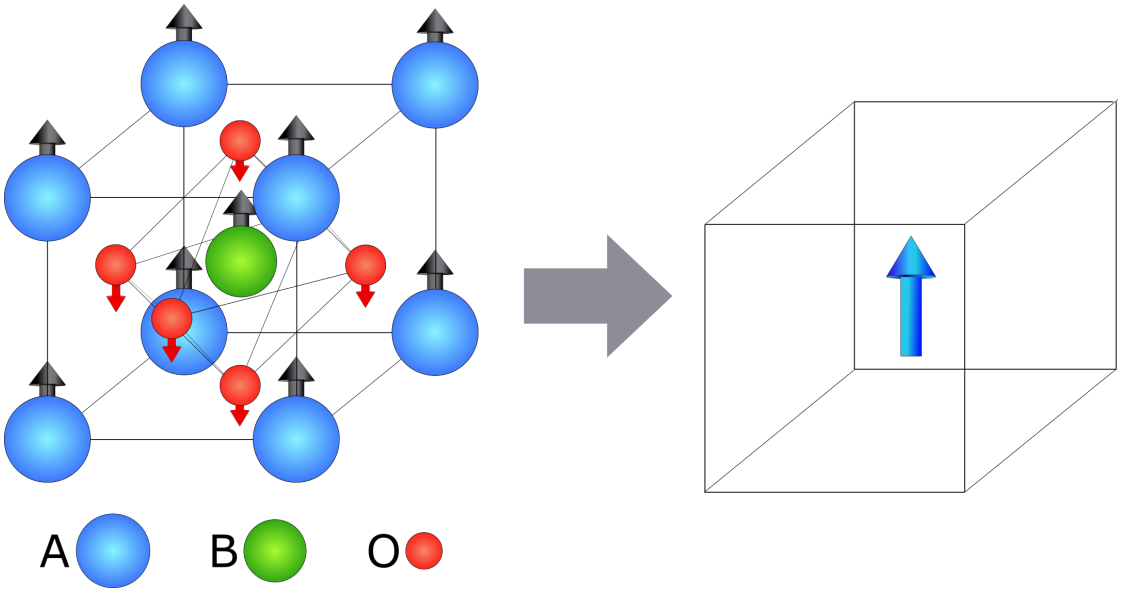

Figure 2.1: Sketch of the coarse-graining step. The FE distortion on the left with the displacement of the cations (A and B atoms) with respect to the oxygen sub-lattice. The arrows represent the atomic displacements. On the right we present the local mode representing the simplified system.

material.

2.2 Second-principles model potential

In this thesis we use another approach called second-principle methods, implemented in the SCALE-UP code [6, 74]. This strategy takes advantage of the work developed using effective-Hamiltonian methods in ferroelectric perovskites avoiding the limitations that these models present.

The drastic simplification of the system performed in the effective-Hamiltonian approach can bring problems with the accuracy of the results if not all instabilities and atomic degrees of freedom of the reference structure are included in the model, since even the high energy modes can be important in the final results of the properties at a quantitative level. Moreover, in some systems such as $PbTiO_3/SrTiO_3$ superlattices with a short periodicity or in domain walls it can be difficult to identify the relevant degrees of freedom. And given the complexity

of these cases would have to be included more degrees of freedom that would make the effective-Hamiltonian models very complex.

In the case of the second-principles methods, we follow the same approach used in effective hamiltonians but removing the coarse graining step. In other words, the energy of the material is expanded in a Taylor series around a reference structure, as well as, in the effective hamiltonians models, but we take into account all atomic degrees of freedom without any drastic simplification. This way, as we will see in the following sections, using this approach, the second-principles models can be built for any material in which all the parameters involved have an obvious physical meaning and they are obtained mostly from first-principles calculations using small simulation boxes.

2.2.1 Reference structure and model variables

The construction of our Second-principles potentials starts with the definition of the reference structure. For the sake of simplicity, the reference structure should be a minimum or a saddle point of the potential energy surface of the material. In the perovskite such as $PbTiO_3$ or $SrTiO_3$ the choice for reference structure is the ideal cubic perovskite structure, with space group $Pm\bar{3}m$. We assume a three-dimensional infinite crystal formed by periodically repeated supercell. Then, the positions of all atoms can be defined by the lattice vectors $\mathbf{R}_l$, where l labels the unit cell inside the supercell, and the $\boldsymbol{\tau}_k$ position of the atom k inside the unit cell. We can define all accessible configurations as distortions of the reference structure where the position of each atom is defined by the position vector, given by

$$r_{lk\alpha} = \sum_{\beta}(\delta_{\alpha\beta} + \eta_{\alpha\beta})(R_{l\beta} + \tau_{k\beta}) + u_{lk\alpha} \tag{2.5}$$

where α and β are the Cartesian directions and the distortions of the system are given by the homogeneous strain $\boldsymbol{\eta}$ and the atomic displacements $\mathbf{u}_{lk}$.

The individual atomic displacements $\mathbf{u}_{lk}$ describe the displacement of a specific atom k in the unit cell l with respect to the strained reference structure (shown in Fig. 2.2(a)). In order to simplify the notation, we can contract the pair of index $lk \leftrightarrow i$ where the index i

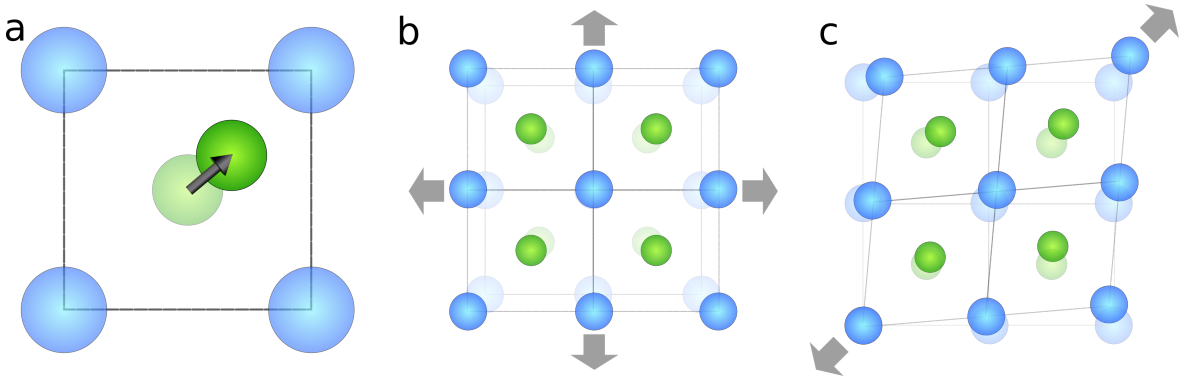

Figure 2.2: Sketch of the model variable with the associated distortions of the reference structure; Panel (a) shows the individual atomic displacements u_i of an atom in a unstrained reference structure; Panel (b) shows the effect of the homogeneous strain $\eta_{\alpha\alpha}$ in the absence of any individual atomic displacement; Panel (c) shows the effect of the off-diagonal strain $\eta_{\alpha\beta}$ (where $\alpha \neq \beta$) in the absence of individual atomic displacement

runs over both cells and atoms within each cell. The homogeneous strain $\boldsymbol{\eta}$ redefines the reference position of all atoms changing the $\mathbf{R}_l$ and $\boldsymbol{\tau}_k$ as we can see in the Eq. 2.5 and in Fig. 2.2 (b). The homogeneous strain $\boldsymbol{\eta}_{\alpha\beta}$ in our model is given by

$$\boldsymbol{\eta} = \begin{pmatrix} \eta_{11} & \eta_{12} & \eta_{13} \\ \eta_{21} & \eta_{22} & \eta_{23} \\ \eta_{31} & \eta_{32} & \eta_{33} \end{pmatrix} \tag{2.6}$$

We can rewrite the homogeneous strain using Voigt notation obtaining $\boldsymbol{\eta} = (\eta_1, \eta_2, \eta_3, \eta_4, \eta_5, \eta_6)$ in which the diagonal elements $\eta_\alpha = \eta_{\alpha\alpha}$ (for $\alpha = 1, 2$ and 3). In the case off-diagonal elements defined as $\eta_{\alpha'} = \eta_{\alpha\beta} + \eta_{\beta\alpha}$. The strain components introduce the homogeneous shear deformation as we show in Fig. 2.2(c).

2.2.2 Taylor expansion of the energy

The energy can be written as a Taylor expansion in terms of atomic displacements ($\{\mathbf{u}_i\}$) and homogenous strain ($\boldsymbol{\eta}$) around the cubic reference perovskite structure, as

$$E(\{\mathbf{u}_i\}, \boldsymbol{\eta}) = E_0 + E_{\rm p}(\{\mathbf{u}_i\}) + E_{\rm s}(\boldsymbol{\eta}) + E_{\rm sp}(\{\mathbf{u}_i\}, \boldsymbol{\eta}) \tag{2.7}$$

where E_0 is the energy of the reference structure, $E_{\rm p}$ is the (phonon) energy involving only atomic displacements, $E_{\rm s}$ is the bare elastic energy, and $E_{\rm sp}$ is the interaction between phonons and strains. Lets us describe in more detail the different terms in the Taylor expansion in the next sections.

The phonon contribution, E_p

The energy changes due to the atomic displacements ($\{\mathbf{u}_i\}$) can be expressed as a Taylor expansion around the reference structure as

$$E_{\rm p}(\{\mathbf{u}_i\}) = \frac{1}{2}\sum_{i\alpha j\beta} K^{(2)}_{i\alpha j\beta} u_{i\alpha} u_{j\beta} + \frac{1}{6}\sum_{i\alpha j\beta k\gamma} K^{(3)}_{i\alpha j\beta k\gamma} u_{i\alpha} u_{j\beta} u_{k\gamma} + ... \tag{2.8}$$

where the first term corresponds to the harmonic part and the higher orders contain the anharmonic part. The tensor $\mathbf{K}^{(n)}$ is formed by the derivatives of the energy given by

$$K^{(n)}_{i\alpha j\beta ...} = \left.\frac{\partial^n E}{\partial u_{i\alpha}\partial u_{j\beta}...}\right|_{RS} \tag{2.9}$$

where the first derivatives $\mathbf{K}^{(1)}$ are zero once the chosen reference structure is a minimum or a saddle point of the potential energy surface.

In order to guarantee that a rigid translation of the material does not change the energy and does not induce forces on the atoms, the coefficients $\mathbf{K}^{(n)}$ have to satisfy the acoustic sum rules (ASRs). In fact, we can rewrite the $E_{\rm p}$, and satisfy automatically the ASRs for all orders, if we expand the energy as a function of displacement differences as

$$\begin{aligned} E_{\rm p}(\{\mathbf{u}_i\}) \; = & \frac{1}{2}\sum_{ijkh\alpha\beta} \tilde{K}^{(2)}_{ij\alpha kh\beta}(u_{i\alpha}-u_{j\alpha})(u_{k\beta}-u_{h\beta}) + \\ & \frac{1}{6}\sum_{ijkhrt\alpha\beta\gamma} \tilde{K}^{(3)}_{ij\alpha kh\beta rt\gamma}(u_{i\alpha}-u_{j\alpha})(u_{k\beta}-u_{h\beta})(u_{r\gamma}-u_{t\gamma}) + ... \end{aligned} \tag{2.10}$$

and this way in the case of a rigid translation of the material the differences of the displacements will be zero and there are no induced forces on the atoms.

The strain contribution, E_s

The E_s gives us the energy variation when we homogeneously strain the reference structure. As well as in the previous case, the E_s can be expanded in a Taylor series as

$$E_{\mathrm{s}}(\boldsymbol{\eta}) = \frac{N}{2}\sum_{ab} C^{(2)}_{ab}\eta_a\eta_b + \frac{N}{6}\sum_{abc} C^{(3)}_{abc}\eta_a\eta_b\eta_c + ... \tag{2.11}$$

where N is the number of cells in the supercell and the coefficients of the expansion are given by

$$C^{(n)}_{ab...} = \frac{1}{N}\frac{\partial^n E}{\partial\eta_a\partial\eta_b...}\bigg|_{RS} \tag{2.12}$$

As well as in the previous section, there are no linear terms because we choose a reference structure that is a minimum or a saddle point of the potential energy surface. The harmonic terms in the expansion are known as the elastic constants that define the elastic response of the material in the reference structure.

The coupling between phonons and strain, E_{sp}

The last term in the Eq. 2.7 refers to the coupling between the atomic displacements ($\{\mathbf{u}_i\}$) and homogenous strain ($\boldsymbol{\eta}$). This term is given by

$$\begin{aligned} E_{\mathrm{sp}}(\{\mathbf{u}_i\},\boldsymbol{\eta}) \; &= \frac{1}{2}\sum_a\sum_{ij\alpha}\tilde{\Lambda}^{(1,1)}_{aij\alpha}\eta_a(u_{i\alpha}-u_{j\alpha}) + \\ &+ \frac{1}{6}\sum_a\sum_{ijhk\alpha\beta}\tilde{\Lambda}^{(1,2)}_{aij\alpha kh\beta}\eta_a(u_{i\alpha}-u_{j\alpha})(u_{k\beta}-u_{h\beta}) + \\ &+ \frac{1}{6}\sum_{ab}\sum_{ij\alpha}\tilde{\Lambda}^{(2,1)}_{abij\alpha}\eta_a\eta_b(u_{i\alpha}-u_{j\alpha}) + ... \end{aligned} \tag{2.13}$$

where coefficients of the expansion are $\tilde{\Lambda}^{(n,m)}$, where n and m define the order of the expansion for the strains and the atomic displacements, respectively. The coefficients $\tilde{\Lambda}^{(1,1)}$ are called force response internal strain tensor, that gives the forces on the atoms as a consequence of the homogeneous strain.

Symmetry adapted terms

Associated to the reference structure we have a set of lattice-translational and point symmetries. When we introduce the symmetries in second-principles models we can reduce the number of independent parameters.

Then, the symmetry related products can be gathered together and associated to the same coefficients of the Taylor expansion. Such groups of the symmetry related terms are called symmetry-adapted terms.

One example, in the case of the cubic system is associated with the three diagonal strain terms. The energy contributions associated with these terms are given by:

$$\frac{N}{2}\Big(C_{11}\eta_1^2 + C_{22}\eta_2^2 + C_{33}\eta_3^2\Big) = \frac{NC_{11}}{2}\Big(\eta_1^2 + \eta_2^2 + \eta_3^2\Big) \tag{2.14}$$

where the cubic symmetry implies $C_{11} = C_{22} = C_{33}$ and the symmetry-adapted terms formed by the η_1^2, η_2^2 and η_3^2.

External electric fields

Let us also note that local electric dipoles $d_{i\alpha}$ are computed, within a linear approximation, as

$$d_{i\alpha} = \sum_{\beta} Z^*_{i\beta\alpha} u_{i\beta} \ , \tag{2.15}$$

where $Z^*_{i\beta\alpha}$ is the Born effective-charge tensor of atom i; here, i runs over all atoms in the material and $\alpha, \beta = x, y, z$ label spatial directions.

Then, the effect of an external electric field $\boldsymbol{\mathcal{E}}^{\rm ext}$ is incorporated in our second-principles simulations by including in the the coupling term in Eq. 2.7 [6]

$$E(\{\mathbf{u}_i\}, \boldsymbol{\eta}; \boldsymbol{\mathcal{E}}^{\rm ext}) = E(\{\mathbf{u}_i\}, \boldsymbol{\eta}) - \sum_{i\alpha} d_{i\alpha}\mathcal{E}^{\rm ext}_{\alpha} \ , \tag{2.16}$$

This way we have the possibility to control different materials by applying external electric fields.

Long-range electrostatic interactions

Until now, we describe the interatomic interactions without making any considerations about the spatial range. Then, in theory our models should be able to include the interatomic interactions between all atoms. However, in practice due to computational limitations, we need to truncate the spatial extend of these interactions defining the terms that we will include in our model.

In the case of metals, such approach is supposed to work well, since the free charges will screen the long-range interactions. Nonetheless, in the case of insulators, the long-range Coulomb interactions cannot be neglected. These interactions are a consequence of the interaction between the local electric dipoles $\mathbf{d}_i$ (defined in Eq. A.1) that appear due to the ions distortions with respect to the reference structure.

Then, we can split the terms that involve the atomic displacements $\mathbf{u}_i$ into long- and short-range contributions:

$$\mathbf{K}^n = \mathbf{K}^{n,sr} + \mathbf{K}^{n,lr} \tag{2.17}$$

and

$$\boldsymbol{\Lambda}^{(m,n)} = \boldsymbol{\Lambda}^{(m,n),sr} + \boldsymbol{\Lambda}^{(m,n),lr} \tag{2.18}$$

where the separation between these two parts can be made for all orders n of the Taylor expansion.

The short-range interactions are treated according to the strategy described previously, however in the case of the long-range interactions there are an analytic expression in the limit of long separations. Therefore, in the second-principles models were used the strategy presented by Gonze and Lee [82], writing the long-range coefficients as

$$K^{(2),lr}_{i\alpha j\beta} = \sum_{\gamma\delta} Z^*_{i\alpha\gamma} Z^*_{j\beta\delta} \Big(\frac{(\epsilon^{-1}_\infty)_{\gamma\delta}}{D^3} - \frac{3\Delta_\gamma \Delta_\delta}{D^5} \Big) (\det \epsilon_\infty)^{-1/2} \tag{2.19}$$

where

$$\Delta_\alpha = \sum_\beta (\epsilon^{-1}_\infty)_{\alpha\beta} \Delta r_\beta \tag{2.20}$$

in which

$$D = \sqrt{\boldsymbol{\Delta} \cdot \Delta\mathbf{r}}$$
$$\Delta\mathbf{r} = \mathbf{R}_j + \boldsymbol{\tau}_j - \mathbf{R}_i - \boldsymbol{\tau}_i \tag{2.21}$$

The ϵ_∞ is the high-frequency dielectric permittivity tensor. In this work, we consider the long-range dipole-dipole interaction at the harmonic level. Besides that, in the second-principles calculations, we use a periodic repeated simulation box (supercell) and so the infinite range couplings are computed by performing the Ewald summation.

2.2.3 Calculating the parameters and precision

The models described previously are constructed with parameters computed directly from first-principles. In practice, to construct the model several approximations were done [6]. First, the spatially truncation to define the short-range limit and as a consequence defining the interactions included. Second, Wojdeł and coworkers [6] truncated the number of bodies included in the different terms presented in the previous sections. The models we will use in this thesis were constructed considering only two bodies terms. Third, they have to define the maximum order of Taylor expansion. In this case, they expand up to the fourth-order, the minimum order to obtain a model able to produce a defined energy minimum.

The lower-order terms (the harmonic part) are obtained from density-functional perturbation theory calculations and the models are constructed in order to include an exact description of the harmonic energy of the studied materials.

Regarding the anharmonic part, the different coefficients are fitted in order to create a model which are able to reproduce a first-principle results of a training set formed by the reference structure and the most relevant low-energy configurations (in Fig. 2.3). This fitting procedure is based in three goal functions. The first one implemented in order to guarantee that the model reproduces the set of energies obtained from the training set. The second goal function imposes a zero-gradient conditions for the different configuration included in the training set. Note that all the configurations in the training set are minima or saddle points in the potential energy surface obtained at very low temperature, hence the gradient of the energy should be zero. In addition, the third goal function associated with the

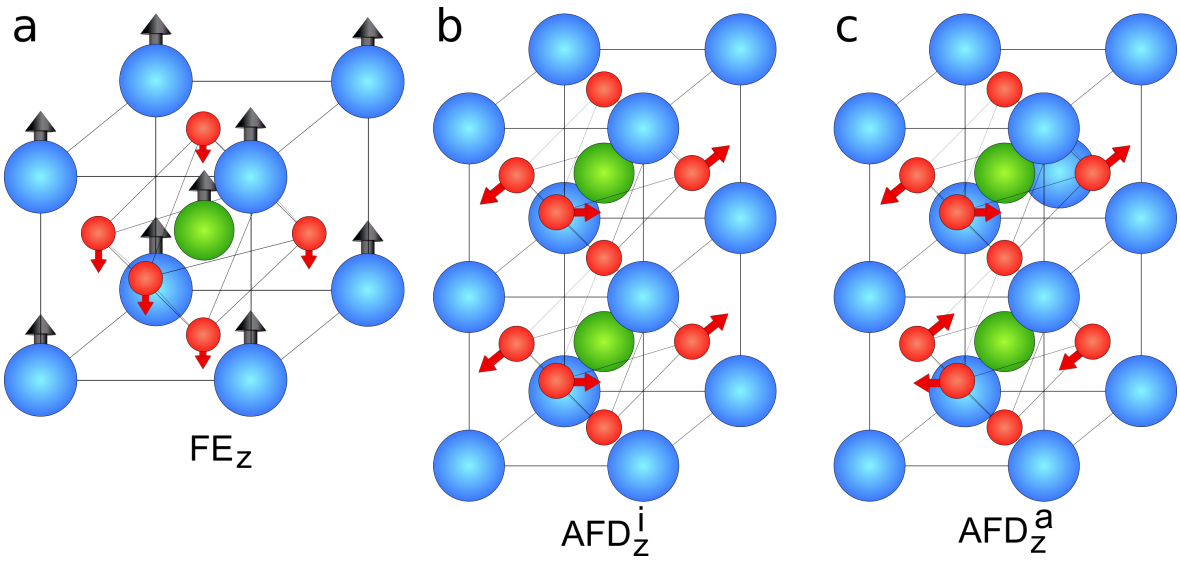

Figure 2.3: Sketch of the most low-energy configurations in ABO_3 perovskite oxides. Panel (a) shows the ferroelectric instability (FE_z); Panels (b) and(c) present the antiferrodistortive instabilities with the O_6 octahedra rotation along z in-phase AFD_z^i (b) and in antiphase AFD_z^a(c). The arrows represent the atomic displacements.

second derivative of the energy. The second-principles models obtained can be improved systematically depending on the precision required.

2.2.4 Models for superlattices

The $PbTiO_3$/$SrTiO_3$ superlattice models [5] were constructed from the models of the individual materials ($PbTiO_3$ and $SrTiO_3$) [6]. The different interactions within each layer are defined as in the bulk potentials. In the interface the different Ti-O interactions are obtained as an average of the same interactions in two materials, $PbTiO_3$ and $SrTiO_3$. Likewise the interactions involving Pb and Sr atoms are given by the average between the interactions of Sr–Sr and Pb–Pb pairs in the respective bulk materials.

The main effect in the stacking in the superlattice is the electrostatic interactions, in which the long-range dipole-dipole interactions are controlled by the Z^* of the bulk materials and the weighted average of the ϵ_∞ obtained from the first-principles results for each material($6.2\epsilon_0$ for $SrTiO_3$ and $8.5\epsilon_0$ for the $PbTiO_3$). Finally, the Z^* of the atoms inside the

layers of the two different materials are normalized according to $\sqrt{\epsilon_\infty}/\epsilon_\infty^{ATiO_3}$, where A is the Pb or Sr atom. In the case of the atoms at the interface the Z^* were kept as the original bulk values. Regarding the epitaxial constraints, it was assumed an in-plane lattice of $a = b = 3.901$ Å and was imposed an external expansive hydrostatic pressure of 11.2 GPa to correct the underestimation of the cubic-lattice constant obtained within the local density approximation.

Applying all approximations, Wojdeł and coworkers were able to construct different $PbTiO_3$/$SrTiO_3$ superlattice second-principles models with different thickness of $PbTiO_3$ and $SrTiO_3$.

2.3 Main results obtained with second-principles methods

The strategy described in the previous sections was implemented to construct second-principles models to tackle specific problems, which until now were inaccessible or computationally very expensive using first principles.

First of all, it was demonstrated that the models constructed for $PbTiO_3$ and $SrTiO_3$ reproduce the first-principles results at low temperature [6]. This test showed that second-principles models reproduce very well the structural parameters and the energetics of all low temperature equilibrium phases of $PbTiO_3$ and $SrTiO_3$.

Then, the models were used to study the temperature behavior of $PbTiO_3$ and $SrTiO_3$. In the first case, $PbTiO_3$ showed a phase transition from a high temperature cubic phase to a low temperature phase with a tetragonal structure in which one of the components of the polarization becomes nonzero [6]. The results as a function of temperature showed a qualitatively good description of $PbTiO_3$ (in Fig. 2.4), when compared with the polarization and strains obtained experimentally. However the transition was obtained at $T_c \approx 510$ K, while the experimental value is $T_c \approx 760$ K [83]. In the case of $SrTiO_3$ a similar structural transition was observed at $T_c = 160$ K, from a high temperature cubic phase to a low temperature tetragonal structure accompanied by rotation of the oxygen octahedra in antiphase (as showed in Fig. 2.3 (c)). Experimental results indicate that this transition occurs at $T_c = 105$ K [15]. The disagreement between the predicted and experimental values of T_c is a

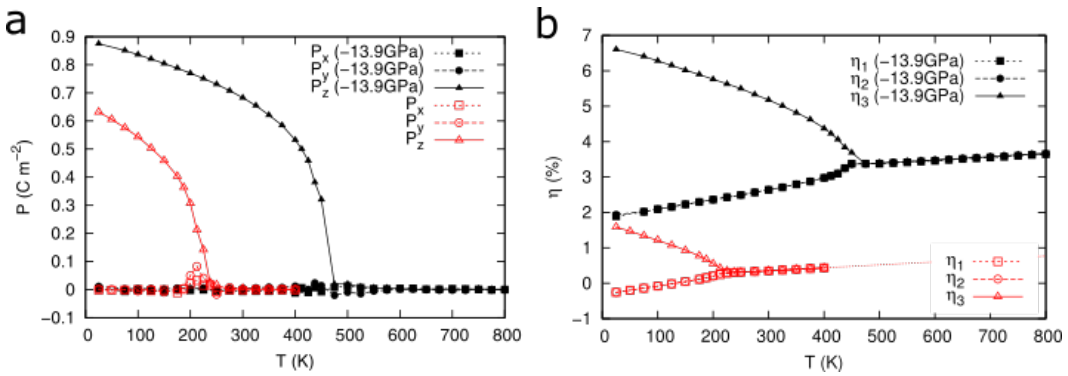

Figure 2.4: Polarization (a) and strains (b) of $PbTiO_3$ as a function of the temperature. Two different situations were considered: (i) under zero external pressure and (ii) under an external hydrostatic pressure of -13.9 GPa, that compensates the underestimation of the cubic lattice constant obtained using LDA. The figure was obtained from [6].

relevant evidence in both cases. To explain this discrepancy, one of the possible causes can be attributed to the approximations that are made in the models, for example the number of bodies involved or in the order of expansion considered. To compute several properties, the model is enough to obtain results according to the experimental ones, however it is possible that in the calculation of T_c, more detail in PES is necessary. In addition, another possibility may arise from the fact that DFT underestimating the energy difference between the ground state and the reference structure which may explain why the values of the transition temperature are lower than those observed experimentally.

Furthermore, to the study of the monodomain properties, the second-principles methods allowed the authors to study multidomain configurations, looking in detail at the domain walls. In the case of $PbTiO_3$, Wojdeł and Íñiguez [1] studied the 180° domain walls in $PbTiO_3$ detailing the structure and atomic distortions at the domain walls as a function of temperature. In the 180° domain walls configuration was observed an extra phase transition at $T_c^{DW} \approx 320$ K from a high temperature disordered domain walls with a null thermal average polarization to a low temperature polarized domain wall. This polarization is confined within very narrow domain walls (less than one unit cell of thickness) and is normal to the polarization in the domains with a Bloch-like character, as we show in Fig. 1.5.

The second-principles methods also allowed the study of $PbTiO_3$/$SrTiO_3$ superlattices,

in which the combination of ferroelectric and paraelectric layers forms the favorable system for the appearance of complex multidomain configurations. A. K. Yadav and coworkers [3] reported the observation of polar vortices in the ferroelectric layers of the superlattices, as we showed in Fig. 1.8 (a). Using second-principles calculations the chiral character of the vortices [8] was explained by a helical rotation of local polarization. Note that the second-principles results reported in the literature are in agreement with the results obtained in an independent way using first-principles calculations presented by Aguado-Puente and Junquera [4] (see Fig. 1.8 (b)). Beyond that, in similar superlattices and taking advantage of the ability of the second-principles to describe the different configurations at atomic scale was reported negative capacitance across a wide range of temperatures [5]. This negative capacitance was observed mainly in the interface between the paraelectric and ferroelectric layers and at the domain walls due to their motion.

Chapter 3

Low-temperature electric skyrmions

In this chapter we study the columnar nanodomain configuration in order to create and tune an electric skyrmion equivalent of a typical magnetic skyrmion. We study a columnar nanodomain in a single-phase prototype ferroelectric material $PbTiO_3$ at low-temperature using second-principles simulations described in Chapter 2. We discuss the different instabilities of the nanodomain wall, taking into account the size and shape of the ferroelectric nanodomains. The topological properties of the different states of the ferroelectric nanodomain were characterized. Finally, we consider the effect of the epitaxial strain and the response of our system to different external electric fields in order to tune and enhance the properties of the ferroelectric nanodomain.

3.1 Ferroelectric columnar nanodomain

We consider a ferroelectric columnar nanodomain (ND) with positive polarization embedded in a matrix with opposite polarization and between these two domains the nanodomain wall (NDW) forming a close surface around the ND as shown as in Fig. 3.1(a).

Wojdeł and Íñiguez [1] showed that the planar 180° domain walls (DWs) of $PbTiO_3$ (PTO) at low-temperature have a Bloch-like character with a spontaneous polarization confined within the DW plane with a thickness of less than one unit cell (Fig. 3.1(b)). As in the previous case, in the ND configuration (shown in Fig. 3.1(a)) the NDW is also a 180° domain wall that

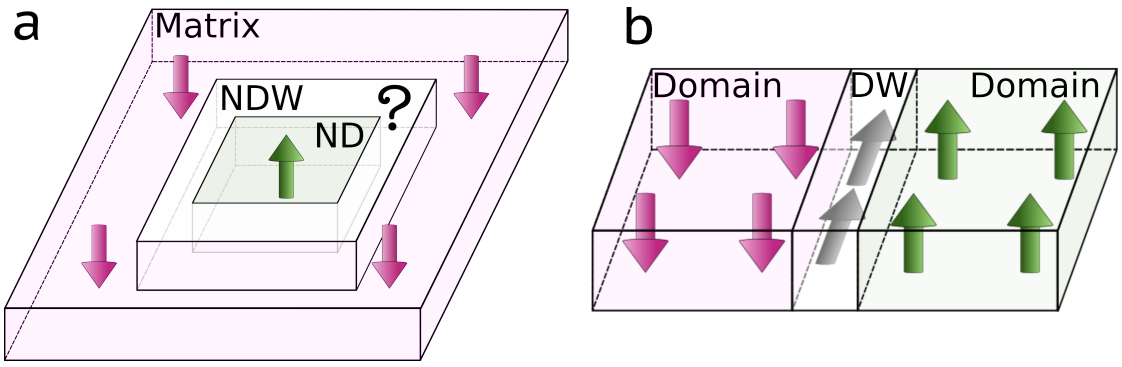

Figure 3.1: Sketches of (a) ND within a matrix of opposite polarization investigated in this chapter; (b) structure of the 180° FE planar DW of PTO at low temperature as predicted in Ref. [1].

forms a closed surface around the ND. Here, we will show how we can take advantage of the Bloch character of the polarization in the NDW to create and tune a variety of complex arrangements with unique properties.

It is important to stress that the ND is a robust and stable configuration at 0 K and survives up to 260 K (as we will show in the next Chapter) even if we consider a small domain with 6×6 unit cells, and even if we take into account that the boundary conditions assumed in the simulations (short circuit) favor the monodomain state (since there is no depolarization field) and not a multidomain configuration.

3.1.1 Nanodomain wall instabilities

In order to study the possible polarization arrangements within the NDW, we consider a ND configuration in which we constrained all the atoms to move only along z (parallel to the ND direction) during the relaxation. The resulting constrained equilibrium configuration is presented in Fig. 3.2(a). We identify the two different domains, with nonzero out-of-plane polarization – positive in the ND and negative in the matrix. Between these two domains we have the NDW with zero polarization. In order to identify the possible arrangements of the polarization within the NDW, we study the main instabilities of the system computing the Hessian matrix implemented in SCALEUP code.

The potential energy of the constrained equilibrium configuration can be expanded in a

Taylor series in terms of small atomic displacements $\mathbf{u}$, according to

$$E(\mathbf{r}_1, ..., \mathbf{r}_N) = E_0 + \sum_{i\alpha} \frac{\partial E}{\partial u_{i\alpha}} u_{i\alpha} + \frac{1}{2} \sum_{i\alpha j\beta} \frac{\partial^2 E}{\partial u_{i\alpha} \partial u_{j\beta}} u_{i\alpha} u_{j\beta} + ... \tag{3.1}$$

where N is the number of atoms in the supercell, α and β denote the Cartesian directions. The $\mathbf{r}_i$ is the position vector of the atom i in the equilibrium configuration.

The first term E_0 corresponds to the equilibrium configuration energy. The second term gives us the first derivatives of the energy. Since our constrained configuration is a minimum or saddle point of the potential energy surface, all the linear terms will be zero.

In the third term, the second derivatives of the energy are the elements of the Hessian matrix (or the force constants) and they give us information regarding the energy curvatures. Then, for a supercell with N atoms we compute the energy variation caused by the $3N$ atomic displacements along the three Cartesian components. The Hessian matrix obtained is a $3N \times 3N$ matrix. From the diagonalization of this matrix we compute the different eigenvalues λ_a and the associated eigenvectors $\{\mathbf{v}_j^a\}$ where j runs over all the N atoms in the supercell give us the pattern of the atomic displacements associated to the eigenvalue λ_a. From all eigenvalues of the system, the ones that are negative show the instabilities of the equilibrium configuration considered.

In Figs. 3.2 [(b)–(e)], we present the eigenvectors arrangement for the four instabilities of the constrained ND configuration with the most negative eigenvalues. In the regions with polarization only out-of-plane, i.e. the ND and the matrix, the eigenvectors are almost zero.

In the NDW, we have the eigenvectors associated with the different instabilities, forming different arrangements in the xy plane. The most negative eigenvalue λ_1, we identify a closed loop of distortions forming a vortex-like arrangement as we can see in Fig. 3.2 (b). In the second eigenvalue λ_2, the average of the distortions in-plane is different from zero and points in the direction $[\bar{1}\bar{1}0]$, presented in Fig. 3.2 (c). The eigenvector associated to the λ_3 form an antivortex-like arrangement in the NDW (Fig. 3.2 (d)). The fourth eigenvector λ_4 presents a more complex arrangement with vortices-like structures in the corners of the ND, as shown in the Fig. 3.2 (e).

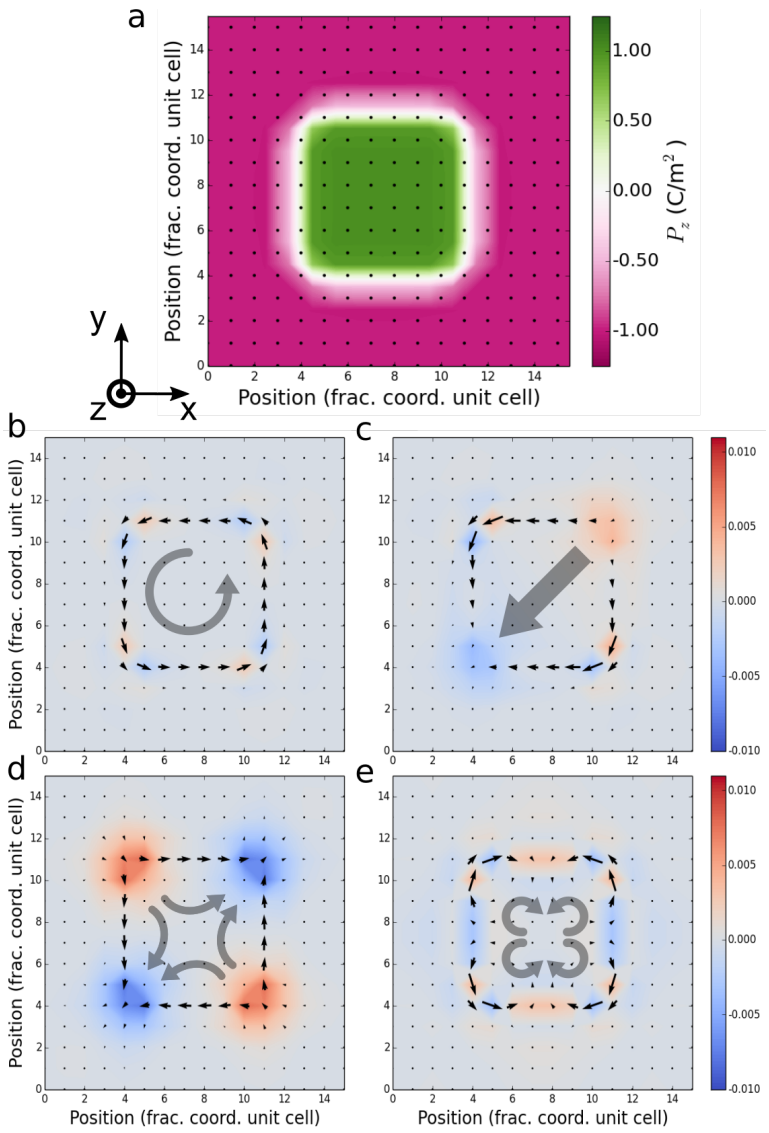

Figure 3.2: Calculated polarization map (a) of the ND constrained configuration where the color scale gives the out-of-plane P_z component, while the arrows correspond to the in-plane P_x and P_y; Panels [(b)–(e)] show the eigenvectors associated to each Pb atom in the supercell. The color scale gives the out-of-plane component v^a_{jz}, while the arrows are the in-plane v^a_{jx} and v^a_{jy} of the eigenvalue λ_a. The panels [(b)–(e)] correspond to the main instabilities with eigenvalues of $\lambda_1 = -1.14$ eVÅ^{-2}, $\lambda_2 = -0.92$ eVÅ^{-2}, $\lambda_3 = -0.67$ eVÅ^{-2} and $\lambda_4 = -0.48$ eVÅ^{-2}.

In order to study the atomic configurations corresponding to the different instabilities, we condense the respective atomic displacement patterns. Then, we construct the initial

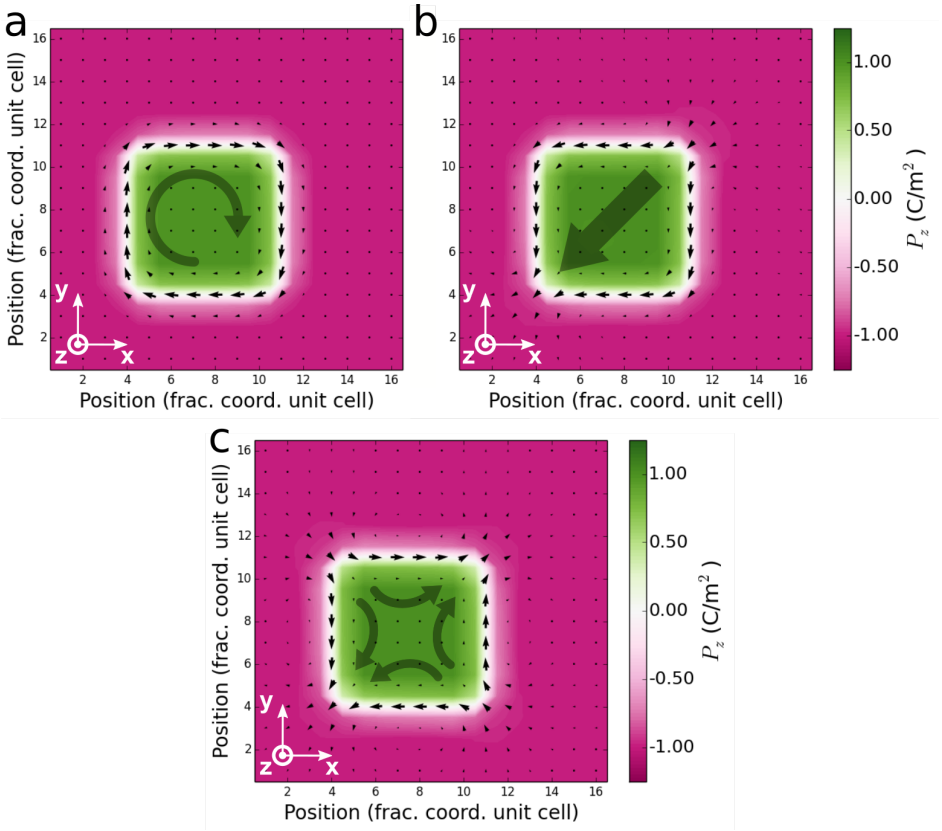

Figure 3.3: Calculated polarization maps of the different NDW configuration regarding the main instabilities λ_a. The color scale gives the out-of-plane P_z component, while the arrows are the in-plane component P_x and P_y.

configurations, where we include the set of atomic displacements of the constrained ND configuration $\{\mathbf{u}_j^{res}\}$ and the eigenvectors associated to each eigenvalue λ_a. Therefore, the initial displacement $\mathbf{u}_j^a$ of each atom j for each eigenvalue λ_a is constructed according to

$$\mathbf{u}_j^a = \mathbf{u}_j^{res} + \xi \mathbf{v}_j^a, \tag{3.2}$$

where ξ is a factor to resize the eigenvectors according to the usual values of the atomic displacements in $PbTiO_3$.

Using standard Monte Carlo method we perform the annealing and structural relaxation of the different initial configurations associated to the different λ_a. The different polarization

maps obtained are presented in Fig. 3.3. The first state of the NDW obtained for the instability λ_1 is presented in Fig. 3.3 (a). The result obtained shows a closed loop of polarization in the xy plane confined in the NDW forming a vortex-like structure. In the second instability in Fig. 3.3 (b), the NDW obtained is polarized in-plane with a dipole moment of about 1.4×10^{28} Cm pointing in the $[\bar{1}\bar{1}0]$. The third mode presented in Fig. 3.3 (c) shows an anti-vortex like structure within the NDW with a null dipole moment in the xy plane. In the case of the instability λ_4 the displacement pattern (Fig. 3.2 (e)) leads us to a saddle point or a very shallow minimum of the energy. Then, during the relaxation and annealing the four vortices in the corners of the ND are destroyed and the energy is reduced by forming a closed loop of polarization within the NDW, which coincides with the result obtained for the instability λ_1.

In Table 3.1, we present the energy of the NDW E_{NDW} obtained from the difference between the energy of different ND states E_{ND} and the energy of ferroelectric monodomain E_{MD} defined as

$$E_{NDW} = \frac{E_{ND} - E_{MD}}{\#NDW u.c.}, \tag{3.3}$$

where the # NDW u.c. is the number of unit cells of the domain wall (for a ND with 6×6 u.c. we have 6×4 u.c. of NDW). Besides that, we also present the energy difference ΔE given by the difference between the E_{ND} and the energy of the restricted configuration E_{Res} in which we constrained all the atoms to move only along z (in Fig. 3.2(a)). This energy difference is given by

$$\Delta E = \frac{E_{ND} - E_{Res}}{\#NDW u.c.}, \tag{3.4}$$

where the energies are normalized by the number of unit cells of the domain wall.

The Table 3.1 shows the results obtained for the different NDW states. When we inspect the results obtained for the ΔE we verify that the unconstrained configurations with in-plane polarization along the NDW present $\Delta E < 0$. Therefore, the system prefers to develop a polarization confined in the NDW, in agreement with the result reported for the planar 180° domain walls (DWs) of $PbTiO_3$ where was observed at low-temperature a spontaneous polarization confined within the DW and normal to the polarization at the domains [1].

Comparing the E_{NDW} of the unconstrained configurations, we verify that the conden-

Table 3.1: Energies and polarizations in xy plane of the different states of the ferroelectric nanodomain. The E_{NDW} is given in eV and is computed using the Equation 3.3; ΔE in eV and obtained according to Equation 3.4; The average polarization in the xy plane is given in Cm^{-2}. The results presented were obtained for a supercell of 16×16×1 unit cells with a ND of 6×6×1 unit cells.

	E_{NDW}	ΔE	P_{xy}^{NDW}
Restricted	0.144	–	–
λ_1	0.116	-0.029	0.00
λ_2	0.121	-0.023	0.08
λ_3	0.132	-0.013	0.00

sation of the state λ_1 results in the NDW with lower energy. Thus, the ground-state of the ND configuration presents a closed loop of polarization in the xy plane along the NDW. The E_{NDW} is always positive, as the monodomain is the ground-state of an infinite crystal of $PbTiO_3$. However, the different NDW configurations presented are metastable solutions and robust even for small ND of 6×6×1 unit cells.

3.1.2 Shape and size of the nanodomain

In order to understand how robust the ND configuration is we studied several shapes and sizes. In the previous section we showed the results obtained for a square ND with 180° DWs perpendicular to [100] and [010] directions (Fig. 3.3). Other possible shapes of the ND are presented in Fig. 3.4 in which we present the polarization maps obtained for a circular ND and for a rotated square ND in with the NDW is perpendicular to $[110]$, $[1\bar{1}0]$, $[\bar{1}\bar{1}0]$ and $[\bar{1}10]$ directions.

In Figs. 3.4, the panels (a), (c) and (e) show polarization maps of the circular ND with the different polarization arrangements in the NDW, which are obtained following the strategy used in the previous section. Likewise, for the rotated square ND it was possible to condense the instabilities of the NDW associated with the three most negative eigenvalues, as we can see in Figs. 3.4 (b) (d) and (f). These results show that both the ND and the different arrangements in the NDW are stable solutions, regardless of the different shapes of the ND.

In addition, we also consider NDs with a rectangular shape, in which we increase the length of the ND only along y and we keep fixed along x. Fig. 3.5 shows the different

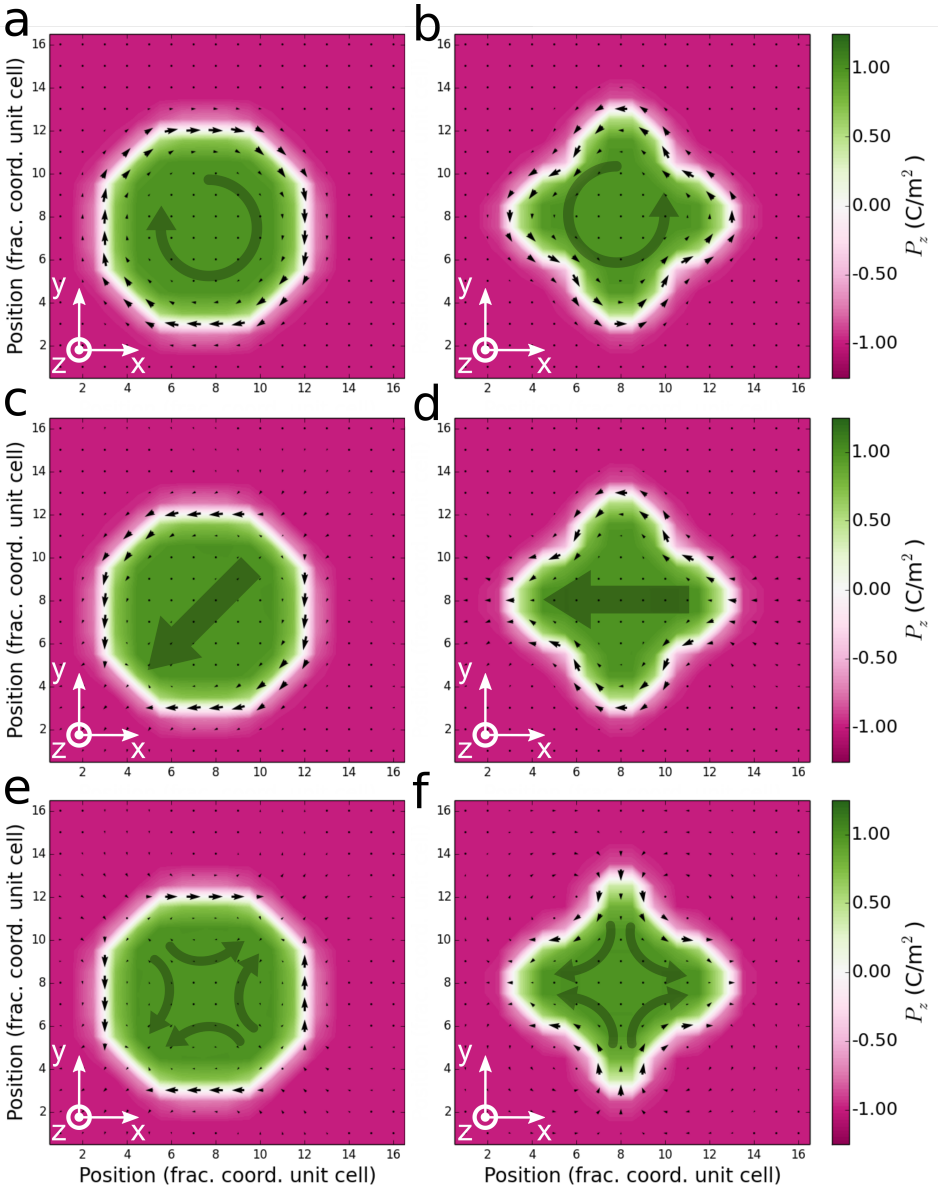

Figure 3.4: Polarization maps of the different instabilities λ_1 [(a) and (b)], λ_2 [(c) and (d)] and λ_3 [(e) and (f)]; Panels [(a), (c) and (e)] show the results obtained for a circular ND and the panels [(b), (d) and (f)] for a rotated square ND; The color scale gives the out-of-plane P_z component, while the arrows correspond to the in-plane P_x and P_y.

rectangular NDs with 6×8, 6×12 and 6×14 unit cells. In the first two cases, the rectangular NDs allow us to stabilize different polarization arrangements in the NDW, as we can see in Fig. 3.5 [(a)–(c)] where we present the results obtained for a NDs of 6×8 unit cells and in

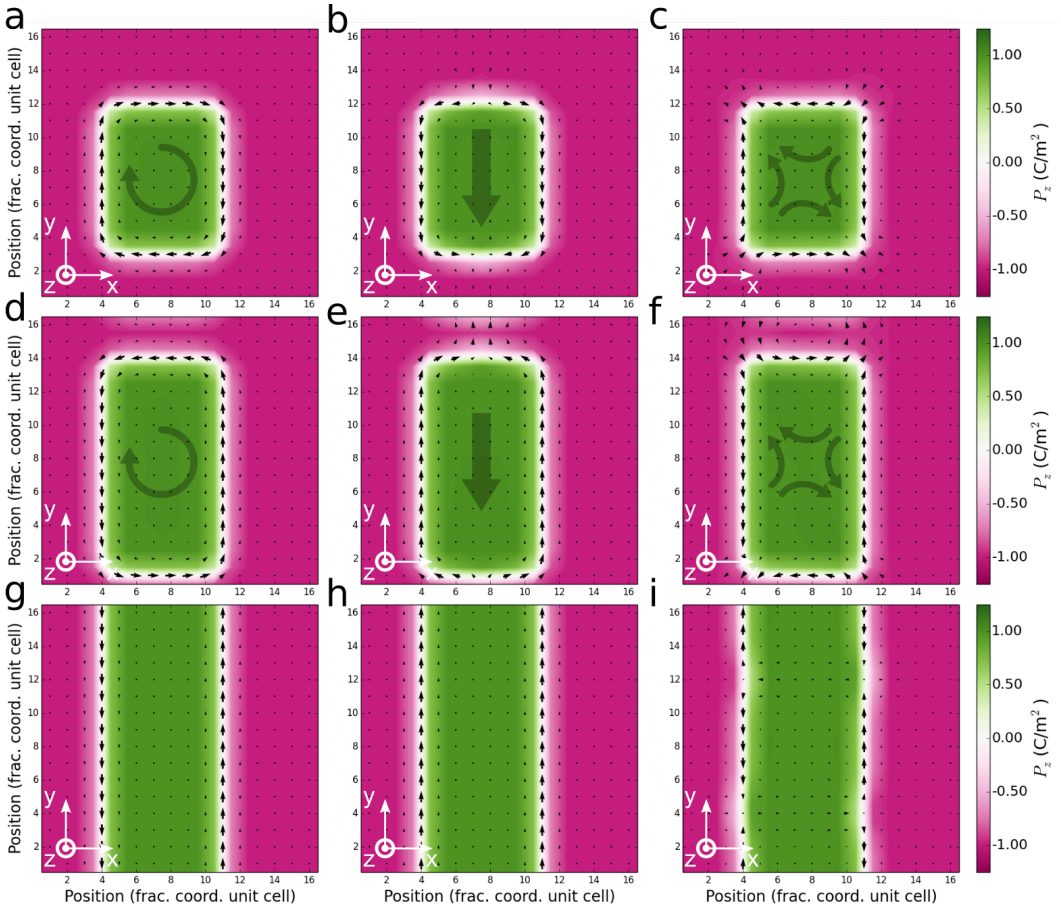

Figure 3.5: Polarization maps of rectangular ND with the different NDW instabilities λ_1 [(a), (d) and (g)], λ_2 [(b), (e) and (h)] and λ_3 [(c), (f) and (i)]; Panels [(a)–(c)] show the rectangular ND with 6×8 u.c.; Panels [(d)–(f)] show the rectangular ND with 6×12 u.c.; Panels [(g)–(i)] show the rectangular ND with 6×14 u.c.; The color scale gives the out-of-plane P_z component, while the arrows correspond to the in-plane P_x and P_y.

the panels [(d)–(f)] for the nanodomain with 6×12 unit cells.

In the case of 6×14 unit cells, the initial configurations constructed using the Eq. 3.2 present only two unit cells of separation between the two sides of the NDW (up and down sides along y). As a consequence, during the relaxation and annealing of these configurations the two sides merge and we obtain a stripe configuration as shown in Figs. 3.5[(g)–(i)] with two planar 180° DWs.

This way the different arrangements of the in-plane polarization confined in the NDW

are robust enough to remain unchanged, in the limit of very low temperatures, even for big changes of the shape or dimensions of the ND. Therefore, the result obtained for the NDW configuration is a consequence of the presence of the domain, regardless of its shape or size. A relevant result for future experimental demonstrations taking into account the difficulties to write experimentally a perfect square domain or to control the exact size of the domain at nanoscale.

3.2 Topological properties

The NDW instabilities obtained in the previous section are similar to skyrmion and anti-skyrmion configurations introduced in Chapter 1. To demonstrate, we need to compute the topological charge $Q = \int q(x,y)dxdy$, where $q(x,y)$ is the topological charge density given by:

$$q(x,y) = \frac{1}{4\pi}\mathbf{u} \cdot (\partial_x \mathbf{u} \times \partial_y \mathbf{u}) \ . \tag{3.5}$$

where $\mathbf{u}$ is the normalized polarization field. The topological charge density $q(x,y)$ is computed following the strategy presented in Appendix D. Fig. 3.6 shows the topological charge density $q(x,y)$ for each NDW configuration.

The first instability in Fig. 3.3 (a) shows a closed loop of polarization around the ND. Such polarization texture is very similar to a skyrmion as described in the Chapter 1. Fig. 3.6(a) shows the $q(x,y)$ which presents local maxima at the NDW corners and a total topological charge of $Q = +1$. Therefore, the ground state of the ND configuration – in which we obtained a closed loop of polarization within the NDW – correspond to an electrical skyrmion in a single phase material, the NDW-skyrmion.

The second instability in Fig. 3.3 (b) presents a polarized NDW. Fig. 3.6 (b) shows the $q(x,y)$ which presents two local maxima and two local minima at the NDW corners. As a consequence, the total topological charge obtained is $Q = 0$. This ND configuration corresponds to a trivial topological texture, the NDW-polar.

The instability λ_3 presented in Fig. 3.3 (c) shows a texture like an antivortex in the NDW. Fig. 3.6 (c) shows the $q(x,y)$ which presents local minima at the NDW corners, like the

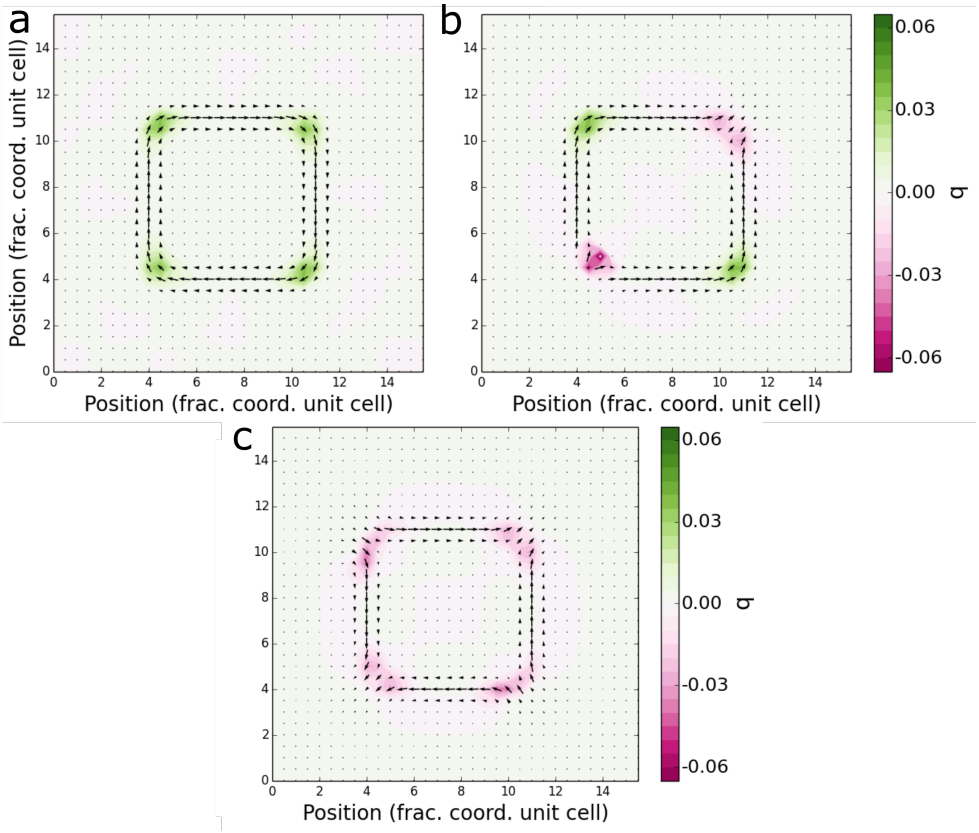

Figure 3.6: Calculated Pontryagin density of the polarization arrangements associated to the different NDW instabilities λ_1 (a), λ_2 (b) and λ_3(c); The color scale gives the Pontryagin density $q(x, y)$, while the arrows correspond to the in-plane normalized polarization P_x and P_y.

peaks obtained in the NDW-skyrmion but with opposite sign. The total topological charge obtained is $Q = -1$. Then, the third state obtained is an electrical antiskyrmion, the NDW-antiskyrmion.

Likewise, the strategy for computing the topological charge was implemented in the different NDs with different shapes, sizes and separations presented in Section 3.1.2. The results obtained show that the topological charge is independent of the shapes, sizes or separations of the NDs.

3.3 Epitaxial strain effect

The epitaxial strain is a key factor to tune and enhance ferroelectric properties of perovskites (as described in the Chapter 1). Let us consider the effect of the epitaxial strain in the ferroelectric ND, which can be imposed by growing $PbTiO_3$ on different substrates. The epitaxial strain forces the in-plane lattice parameters of our $PbTiO_3$ to be equal to the lattice parameters of the substrate a_{sub}, imposing a square substrate with lattice constants $a = b = a_{\mathrm{sub}}$ and $\gamma = \gamma_{\mathrm{sub}} = 90^{\circ}$. The free parameters were annealed and relaxed using Monte Carlo simulations.

In the case of $PbTiO_3$ monodomain (in Fig. 3.7(a)) we identify two different regions. In the first region for $a_{\mathrm{sub}} < 3.945$ Å the polarization points only along z. For tensile strains when $a_{\mathrm{sub}} > 3.945$ Å the polarization rotates, developing an in-plane polarization $P_x = P_y$ (comparison with the results of previous works in literature is discussed in Chapter 4).

The results obtained in Fig. 3.7(b) show the behavior of the polarization in-plane of the NDW-polar state that follows the monodomain behavior with an increment due to the polarized character of its NDW. In the case of the NDW-skyrmion state, the results of the in-plane polarization presented in Fig. 3.7(b) reveal a continuous transition similar to the transition obtained in the case of the $PbTiO_3$ monodomain.

Besides that, the NDW-skyrmion state undergoes a continuous transition with the breaking of the material in 90° domains in-plane, as shown in the Fig. 3.7(d), which explains how we obtain a smaller average $P_{x,y}$.

The new NDW-skyrmion arrangement with the 90° DWs presents a topological charge of $Q = +1$ obtained from the topological charge density presented in Fig. 3.8(c). Therefore, the NDW-skyrmion undergoes a transition from a high-symmetric skyrmion to a polarized skyrmion, keeping constant the topological charge (always equal to $+1$).

The tensile epitaxial strain forces the NDW-skyrmion to adapt, breaking the symmetry in-plane due to the Skyrmion center S_{skyr} (defined in Appendix D) that moves away from the midpoint of the ND. Fig. 3.8 (a) shows the movement of the S_{skyr} as a function of the a_{sub}. In order to understand this transition, we introduce a new quantity, the skyrmion center

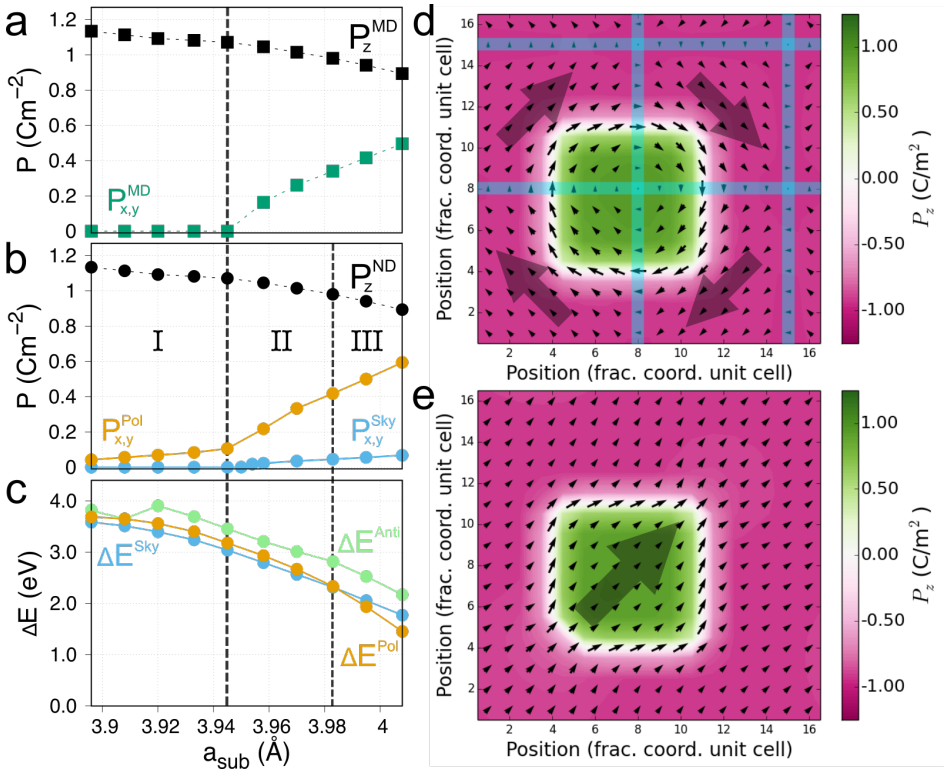

Figure 3.7: Polarization [(a), (b)] and energy difference between the NDW-states and the monodomain (c) as a function of the epitaxial constraint a_{sub}; Polarization maps [(d) and (e)] of the NDW-skyrmion and NDW-polar configurations obtained for $a_{\rm sub} > 3.95$ Å. In panel (a) we show the results of the polarization for the monodomain state in which black-filled squares give $|P_z|$ and the green squares are the $P_x = P_y$; In panel (b) black-filled circles give $|P_z|$ as obtained at the middle of either matrix or ND, blue and orange circles give the $P_x = P_y$ components of the NDW-skyrmion and NDW-polar configurations, obtained from a supercell average and normalized to the supercell volume; In panel (c) the blue, orange and green-filled circles give the ΔE of the NDW-skyrmion, dipolar and antiskyrmion taking the result for the ferroelectric monodomain of as the zero of energy. Black vertical dashed lines show the $a_{\rm sub}$ values of the two different transitions.

susceptibility defined as

$$\chi_{\alpha\beta} = \frac{\partial S_\alpha}{\partial E_\beta} \,, \tag{3.6}$$

where E_β is the β component of an applied electric field. Fig. 3.8(b) shows the skyrmion center susceptibility along the directions xx and xy. Around the $a_{\rm sub} = 3.950$ Å, where we observed the skyrmion-skyrmion transition, the component of our susceptibility χ_{xy} nearly diverges, which seems to indicate that we are facing a transition with a second-order char-

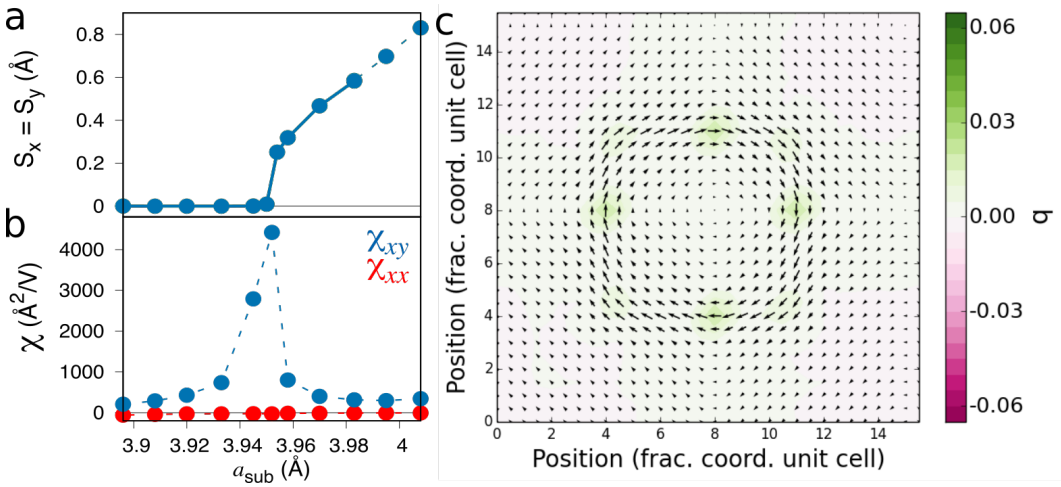

Figure 3.8: The displacement (a) and the susceptibility components (b) of the skyrmion center as a function of a_{sub}. Calculated Pontryagin density map (c) where the color scale gives the $q(x, y)$, while the arrows correspond to the in-plane normalized P_x and P_y. In the panel (a), the dashed line marks the regime where the NDW-polar becomes the ground state and the NDW-skyrmion is a metastable solution.

acter. The component of the skyrmion center susceptibility that diverges is the χ_{xy}, which implies that applying an external electric field along y the center moves along x, the direction normal to the field applied. In this region where χ_{xy} diverges the center of the skyrmion is very mobile, which opens up the possibility of controlling the NDW-skyrmion, moving its center between the four symmetry-equivalent states, applying small electric fields as we will show in the section 3.4.1.

The $90°$ DWs in the matrix bring with them an extra cost on the energy, however such DWs are not present in the NDW-polar, as we can see in Fig. 3.7(e), where we observe a monodomain in the $P_{x,y}$. Such intrinsic difference between the two NDW-states can be seen in their energies (in Fig. 3.7(c)). For $a_{\text{sub}} = 3.983$ Å the energies cross and the NDW-polar becomes the most stable configuration of the ferroelectric ND, which implies a discontinuous transition to a trivial topological texture with $Q = 0$. In Fig. 3.7(c) we also present the ΔE of the NDW-antiskyrmion and we verify that this is the highest-energy NDW state.

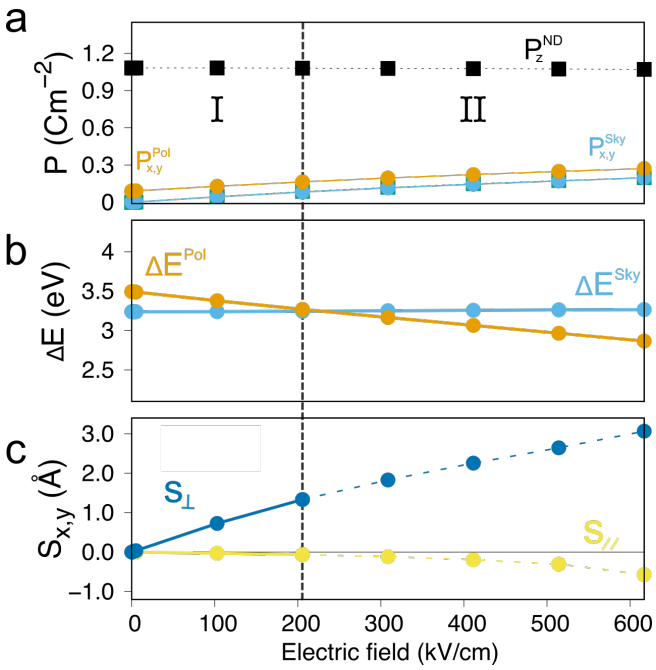

Figure 3.9: Polarization (a) and energy difference between the NDW-states and monodomain (b) and the skyrmion center displacement (c) as a function of the external electric field applied along $[110]$ direction. In panel (a) we show the results of the polarization in which black and green squares give $|P_z|$ and $P_x = P_y$ of the monodomain, respectively. The blue and orange circles are the $P_x = P_y$ of the NDW-skyrmion and NDW-dipolar states, obtained from a supercell average and normalized to the supercell volume. In this panel (a) the green squares that represent the $P_x = P_y$ of the monodomain are not visible since they coincide with the $P_x = P_y$ of the NDW-skyrmion (blue squares); In panel (b) the blue and orange circles give the ΔE of the NDW-skyrmion and dipolar configurations, taking the result for the ferroelectric monodomain as the zero of energy; Panel (c) shows the movement of the skyrmion center in the direction parallel (yellow-filled circles) and the normal (blue-filled circles) to the applied electric field; Black vertical dashed line shows the a_{sub} value of the transitions.

3.4 Response to external electric fields

The electrical skyrmion is a non-trivial topological arrangement of electrical dipoles, thus the application of an external electric field is an obvious choice to control it. By applying an external electric field along $[110]$ direction, $PbTiO_3$ monodomain polarized along z develops a polarization in the xy plane, $P_x = P_y$.

As discussed in previous sections, when $E = 0$ kV/cm and $a_{\mathrm{sub}} = a_{bulk}$ of $PbTiO_3$ the

average in-plane polarization of NDW-skyrmion is zero, which indicates a high symmetry skyrmion and in this case the S_{skyr} coincide with the geometrical center of the ND.

In this section, we will study how the skyrmion reacts to different external electric fields, keeping $a = b = a_{\mathrm{sub}}$ and $\gamma = \gamma_{\mathrm{sub}} = 90^{\circ}$ fixed. This allows us to separate the effect of the external electric field from the effect of strain, studied in the previous section.

Increasing the external electric field the average polarization of our NDW-states in-plane increases as shown in Fig. 3.9(a) following the behavior of the $PbTiO_3$ monodomain. Moreover, the NDW-skyrmion deforms to adapt to the external electric field. The consequence of this field-induced deformation is the displacement of the skyrmion center. Fig. 3.9(c) shows the position of the skyrmion center S_{skyr} moving mainly along the direction perpendicular to the applied field.

Fig. 3.10 shows the rearrangement of the NDW-skyrmion polarization and Pontryagin density when subjected to an external electric field < 200 kV/cm applied along the $[110]$ direction. The figure shows how the closed loop of the NDW-skyrmion reacts to the external electric field. The local electric dipoles tend to align with the direction of the electric field to minimize the energy. This way, the electric field tries to rotate the polarization on two sides of the NDW, the sides with a component of the polarization against the applied field. As a consequence, for an external electric field around 200 kV/cm the energies of the NDW-skyrmion and NDW-polar configurations cross (as we can see in Fig. 3.9(b)) and the NDW-polar becomes the configuration most stable ND configuration.

Moreover, when we increase more the electric field the metastable NDW-skyrmion reaches a critical electric field of about 650 kV/cm where the NDW-skyrmion becomes unstable. So, for these high external electric fields, only the NDW-dipolar is stable.

3.4.1 Control electric skyrmion using electric fields

As discussed in Section 3.3 the epitaxial strain induces a symmetry breaking with the movement of the skyrmion center along one of the four equivalent directions and as a consequence we have four equivalent states.

Besides that, for in-plane lattices around $a_{\mathrm{sub}} = 3.950$ Å the skyrmion center is very mo-

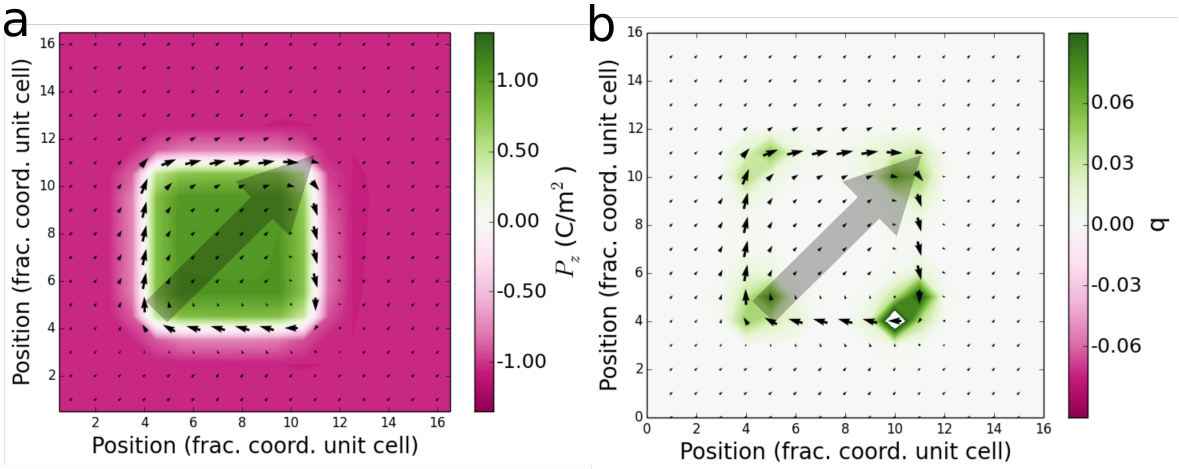

Figure 3.10: Calculated polarization (a) Pontryagin density (b) maps for our ND within a matrix in its NDW-skyrmion ground state subject to an in-plane electric field along $[110]$ direction (the field is indicated by a shadowed arrow). In panel (a) the color scale gives the out-of-plane P_z component, while the arrows correspond to the in-plane P_x and P_y; In panel (b) the color scale gives the $q(x, y)$, while the arrows correspond to the in-plane normalized P_x and P_y.

bile, which opens the possibility of control the NDW-skyrmion using smaller external electric fields.

Then combining the effect of the epitaxial strain with the control of the center using an external electric field, we are able to favor one of the four equivalent states. Using the strategy applied before to study the effect of the electric field, we apply a sequence of electric fields presented in Fig. 3.11(a). The response of the polarization in-plane (Fig. 3.11(b)) and movement of the skyrmion center (Fig. 3.11(c)).

As discussed previously, the movement of the skyrmion implies a change in the average polarization in-plane, given us a way to observe the response of the NDW-skyrmion when switching between the four equivalent states.

3.5 Electric field Vs Epitaxial strain

Previously we studied the effect of the epitaxial stain, keeping the external electric field off and the ferroelectric columnar ND response to the external electric field for a $a_{\text{sub}} = a_{bulk}$.

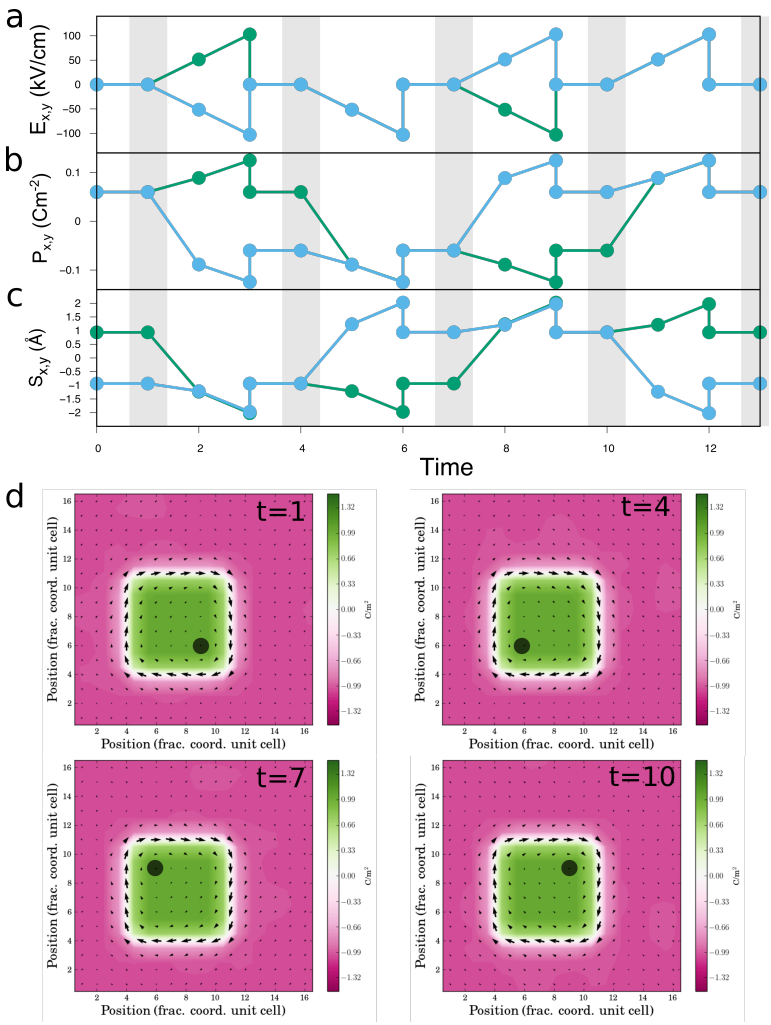

Figure 3.11: Sketch of our concept to control skyrmion center. The external electric field applied (a) the polarization in-plane P_x and P_y (b) and the position of the skyrmion center (c) as a function of MC time. The polarization maps (d) under different electric fields and the black dots represent the corner where the center of the skyrmion goes; Panels [(a)–(c)] the green-filled circle correspond to the x components and the blue-filled circles are the y components.

In the case of the epitaxial stain using different substrates we impose a compressive or tensile strain. As we showed in Section 3.3, depending on the strain constraints imposed, we can stabilize the NDW-skyrmion or NDW-polar states. Applying an external electric field in xy plane, we showed in Section 3.4 a transition from a NDW-skyrmion to NDW-polar configuration.

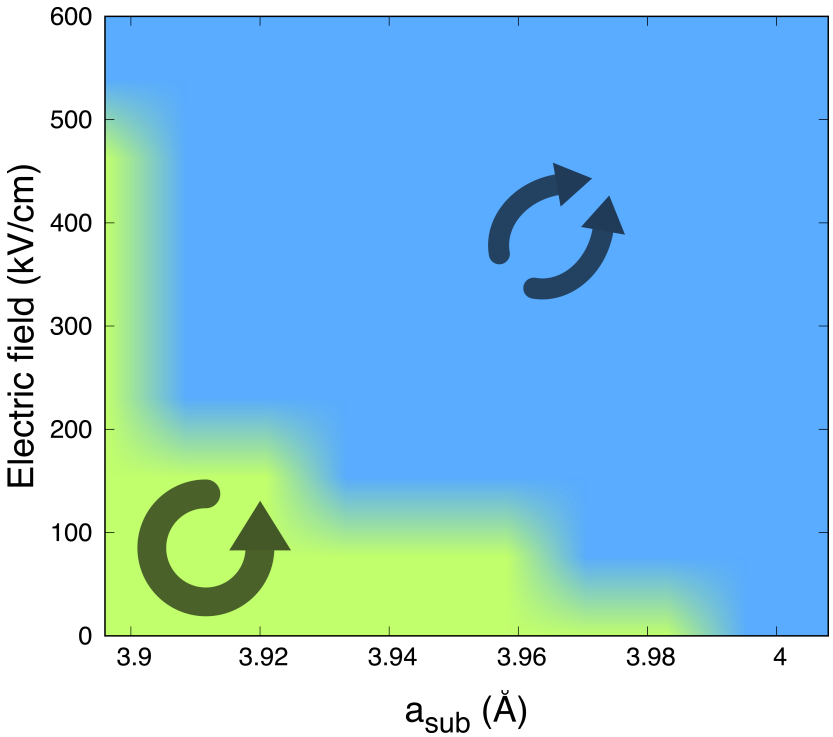

Figure 3.12: Phase diagram of our ferroelectric columnar ND considering the NDW-skyrmion and NDW-polar configurations as a function of the electric field in the xy plane ($\mathbf{E}_{xy} = E\hat{\mathbf{i}} + E\hat{\mathbf{j}}$) and $a_{\rm sub}$; The green and blue regions show the electric fields and $a_{\rm sub}$ where the configurations NDW-skyrmion and NDW-polar are more stable, respectively.

Thus, in this section, the phase diagram of the ferroelectric columnar ND, considering the NDW-skyrmion and NDW-polar configurations as a function of the $\mathbf{E}_{xy}$ (applied along $[110]$ direction) and $a_{\rm sub}$.

Fig. 3.12 shows the phase diagram obtained, where we observe the regions where the NDW-skyrmion (green region) or NDW-polar (blue region) are more stable. These different regions are obtained monitoring the energy difference between NDW-skyrmion and NDW-polar configurations.

As expected taking into account previous results presented in section 3.3 when the $a_{\rm sub}$ value is bigger than $a_{\rm sub} = 3.983$ Å, the NDW-polar is the most stable state, even without the application of any external electric field.

For in-plane lattices $a_{\rm sub} < 3.983$ Å we stabilize the NDW-skyrmion at zero electric field.

In this region, we define the critical electrical field from which the NDW-polar configuration becomes the most stable state. Decreasing the in-plane lattice constants the critical field of the NDW-skyrmion increases, until $\mathbf{E}_{xy} \approx 500$ kV/cm for the biggest value of a_{sub} considered in this phase diagram.

3.6 Summary

In this chapter, we have presented guidelines for stabilizing an electric skyrmion in a nanodomain configuration in $PbTiO_3$ at low temperatures. Thus, we demonstrate that it is possible to stabilize topological structures in simple ferroelectrics using atomistic simulations.

The electric skyrmion proved to be a polarization arrangement robust enough to be stabilized on nanodomains with different shapes or sizes. This fact is important for future experimental studies since the writing of the nanodomain does not require a specific shape to obtain an electric skyrmion.

The application of external electric fields allows us to induce a series of transitions in the configuration of the nanodomain. For small electric fields the electric skyrmion is the most stable configuration. However, by increasing the electric field, Skyrmion develops a polarization in the plane. This polarization is a consequence of the displacement of the center of the skyrmion, which moves in a direction perpendicular to the direction of the applied external field. Thus, we conclude that the movement of the skyrmion can be controlled by the direction of the applied field. By increasing the electric field, the electric skyrmion is destroyed and we obtain a new trivial state with $Q = 0$.

When applying different epitaxial constraints, we observe a spontaneous transition from a high symmetry skyrmion to a polarized skyrmion with the formation of 90° domains in-plane. For higher values of in-plane lattice constant, this polarized skyrmion undergoes a second transition to a trivial state destroying the in-plane 90° domains in-plane. A peak in the susceptibility was identified near the transition of the skyrmion center, showing that the application of small electric fields in this region induces large displacements of the skyrmion center, which may be interesting for future applications that rely on the movement of the

skyrmion center.

Chapter 4

Electric skyrmion phase diagram of temperature and strain

In this chapter, we will study the stability of the skyrmion considering the effect of temperature and epitaxial strain. For that, we will have to pay attention not only to the different transitions associated with the polarization and its direction, but also to the different topological transitions destroying or transforming our electric skyrmion. Firstly, we will study the effect of temperature when the electric skyrmion is in bulk conditions, and thereby minimizing the effect of epitaxial strain. Finally, we will build the phase diagram of the electric skyrmion considering the effect of temperature and the constraints imposed by different substrates. Before that, it was necessary to study the behavior of the $PbTiO_3$ monodomain, thus identify the different phases of polarization in this material and, its impact on the electric skyrmion multidomain configuration.

4.1 Skyrmion stability and transitions in bulk $PbTiO_3$

Temperature is a key factor in the study of the different properties of materials. Besides that, the introduction of temperature in our simulations allows us to have a more accurate understanding of our system in conditions closer to the experimental conditions.

In the previous Chapter 3, we studied a ferroelectric nanodomain in pure $PbTiO_3$ and we found that the ground state of this multi-domain configuration corresponds to an electric skyrmion. However, all the results previously presented were obtained at very low temperatures. Then, in this section, we will study the effect of temperature trying to answer two fundamental questions: (i) is the electric skyrmion stable at finite temperatures? and (ii) what kind of transition will we have in case we destroy the electric skyrmion?

Therefore, using the second-principles model constructed for $PbTiO_3$ (presented in Chapter 2) we study the effect of temperature in the electric skyrmion. We solve this model using Metropolis Monte Carlo methods with a periodically repeated supercell made up of 16×16×10 unit cells (12800 atoms) in which we write a nanodomain with 6×6×10 unit cells. For each temperature we ran 20,000 sweeps for thermalization and extra 20,000 sweeps (or 100,000 sweeps close to transitions) to compute thermal averages. To identify any topological transition associated with changes in the polarization arrangement on the domain wall, we start by computing the topological charge Q (following the strategy presented in Appendix D) for a thermalized configuration, computing the polarization maps $u(x, y)$ and topological densities $q(x, y)$ of a 16×16×1 slice of 16×16×10 supercell. For each temperature, we calculate the topological charge every 100 steps, thus we obtained a collection of Q values for each temperature. Note that, the different simulations of the nanodomain configuration were performed by imposing the $PbTiO_3$ bulk lattice parameters, considering their variation with temperature.

The results obtained are summarized in Fig. 4.1 where we show the evolution of the topological charge as a function of the temperature in the form of a histogram, in which we identify three different regions with different topological properties. In a first region between 0 and 150 K the topological charge is constant and always equal to $+1$. In this region, we obtain the answer to our first question, and then we can say that the electric skyrmion is stable below a critical temperature $T_{skyr} = 150$ K, in which the NDW presents an in-plane polarization that forms a closed loop around the nanodomain.

In the second region we have a distribution of different Q values coexisting. This region is observed between T_{skyr} and T_{ND}, in which T_{ND} defines the temperature at which

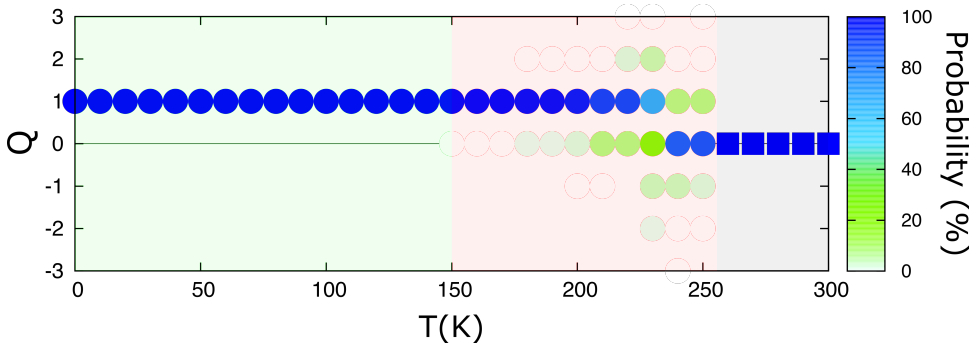

Figure 4.1: Calculated probability distribution of the topological charge as a function of temperature. The color scale represents the probability to obtain a given topological charge Q. The background colors show the different phases identified; white for the skyrmion phase; red for the coexistence phase; grey background the monodomain phase. The circles appear in the temperature range in which the configuration of the nanodomain exists and the squares indicate that the nanodomain has already been destroyed.

the nanodomain is destroyed and is equal to 260 K. So, we called this phase the coexistence phase where the most probable values of Q are $-1, 0$ and $+1$ that correspond to NDW-antiskyrmion, NDW-polar and NDW-skyrmion respectively (arrangements described in Chapter 3). So we answer the second question previously posed, since this second region shows how the NDW-skyrmion state is destroyed in an intermediate phase in which the topological charge goes from $Q = +1$ to a Q that fluctuates between different values.

Finally, in the third region for temperatures above T_{ND} the topological charge is always zero once the nanodomain has been destroyed. To analyze this transition, we must consider the polarization arrangement and how it evolves as a function of temperature. In Fig. 4.2 we show some snapshots and we verify that between 220 K and 260 K the nanodomain reduces its size until $T = 260$ K where the thermal fluctuations are sufficient to destroy completely the nanodomain (it is important to note that, at temperatures below 220 K, we observe some fluctuations in the form of the nanodomain in its corners, but the appreciable reduction in the size of the nanodomain starts at 220 K).

Thus, for a nanodomain with 6×6 unit cells in-plane, the transition from the coexistent phase to a trivial phase is a consequence of the complete destruction of the nanodomain. The T_{ND} depends on the size of the ND. In our case we consider a nanodomain with 6×6

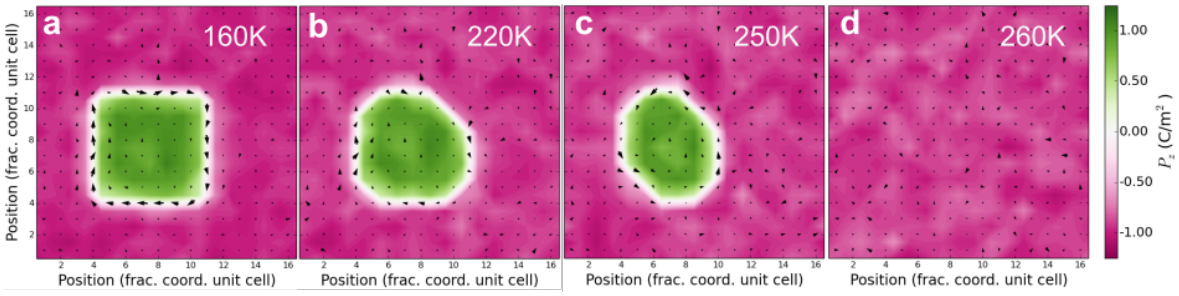

Figure 4.2: The polarization maps for snapshots obtained at different temperatures ($T = 160$ K, $T = 220$ K, $T = 250$ K and $T = 260$ K); the color scale gives the out-of-plane P_z component, while the arrows correspond to the in-plane P_x and P_y.

unit cells in the plane, however if we increase the size of the nanodomain it will disappear at higher temperatures. In addition, our simulations are carried out under short-circuit boundary conditions that do not favor our nanodomain. So if we consider the appropriate electrical boundary conditions such as the condition in some ferroelectric/dielectric superlattices (as we will see in next Chapter) we favor the formation of domains and we will increase the T_{ND}.

This way we show the behavior of the nanodomain configuration when we increase the temperature, and how it affects the polarization arrangement and therefore the topology giving rise to three distinct phases.

4.2 Structural and topological phase diagram in thin films

We will now introduce the effect of epitaxial strain together with temperature. Let us start by studying the behavior of $PbTiO_3$ monodomain grown on different substrates. Then, we study the structural and topological behavior of the electric skyrmion as a function of temperature and for different epitaxial constraints.

4.2.1 Monodomain

In this section, we present the phase diagram of the $PbTiO_3$ monodomain as a function of temperature and epitaxial strain obtained using the second-principles methods. This way we

can understand the behavior of $PbTiO_3$ monodomain without the effects of the ferroelectric nanodomain.

Previous literature

In a previous work, the behavior of $PbTiO_3$ in bulk was studied as a function of the temperature using second-principles [6]. Such study showed a phase transition from a ferroelectric phase with polarization parallel to the z direction at low temperature to a paraelectric phase with an average null polarization.

In addition, Diéguez et al. [84] studied the behavior of $PbTiO_3$ and other perovskite oxides when varying the in-plane epitaxial constraints using Effective Hamiltonian methods. The results obtained indicate that $PbTiO_3$ at low-temperature presents a polarization parallel to the z direction for compressive strains, called c-phase. For the tensile stress, they obtained an aa-phase in which the polarization points only in the plane xy, according to $P_x = P_y \neq 0$ and $P_z = 0$. Between these two phases they predict a multidomain structure, mixing domains from both phases.

Another study of the effect of the epitaxial strain on $PbTiO_3$ at 0 K was carried out using first-principles methods [85], in which the existence of only two phases was predicted. The phase with polarization parallel to the z direction for compressive epitaxial strains and a polarization only in-plane with $P_x = P_y$ for bigger values of the in-plane lattice and between these phases was observed and abrupt transition. It is important to note that, in this study the angles $\alpha = \beta = 90°$ (α and β are the angles of the c axis with the a and b axis respectively) are held fixed.

Present work

We used second-principles methods to carry out several Monte Carlo simulations for different in-plane lattice parameters at very low temperatures. Subsequently, for each of these in-plane lattice parameters, several Monte Carlo simulations are made at different finite temperatures with a periodically repeated supercell made up of $16\times16\times16$ unit cells (in which

we consider 10,000 sweeps for thermalization and 40,000 sweeps to compute thermal averages). Regarding the application of the epitaxial restrictions, we impose a substrate with square symmetry defined by an in-plane lattice constants $a_{\mathrm{sub}} = b_{\mathrm{sub}}$ and with $\gamma_{\mathrm{sub}} = 90°$. All these parameters define the epitaxial constraints and they are held fixed during the Monte Carlo simulation.

At low-temperature $T = 12.5$ K, we obtain two different phases as shown in Fig. 4.3 (a). The first phase called c-phase, with a_{sub} values around the $a_{\mathrm{bulk}} = 3.933$ Å of $PbTiO_3$ and for compressive strains, in which the polarization point in the [001] direction. When applied tensile strain we obtain another phase called r-phase, in which the polarization rotates, developing a polarization in-plane with $P_x = P_y \neq 0$. For $a_{\mathrm{sub}} > 4.014$ Å we observe a change of the polarization components, in which the $P_{x,y}$ increases while the out of plane component decreases. Such change seems to correspond to the beginning of a transition from the r- to aa-phase.

At higher temperature $T = 250$ K (in Fig. 4.3 (b)) two phases are observed. First a c-phase, which we also observe at low temperatures, and when we increase the in-plane lattice parameter we have a transition in which the polarization rotates fully in-plane, pointing in the $[110]$ direction, so called aa-phase.

In the Fig. 4.3 (c)–(e) we present the behavior of the polarization for three different in-plane lattice parameters a_{sub}. In the panel (c) the polarization always remains parallel to z and almost constant over the temperature range considered. In the case of panels (d) and (e) at low temperatures was obtained a r-phase. When the temperature increases the r-phase is destabilized and undergoes two different phase transitions to c-phase ($a_{\mathrm{sub}} = 3.983$ Å) and aa-phase ($a_{\mathrm{sub}} = 4.014$ Å).

All this information is gathered together in the phase diagram of $PbTiO_3$ presented in the Fig. 4.4 (a) in which we can identify the three different phases previously described. When the in-plane lattice constant is increased, the temperature range in which r-phase is the most stable increases. For $a_{\mathrm{sub}} > 4.01$ Å the aa-phase is favored at higher temperatures.

It is important to note that our results showed the formation of a r-phase. Such results are partially in disagreement with the results obtained by Diéguez et al. [84] in which was

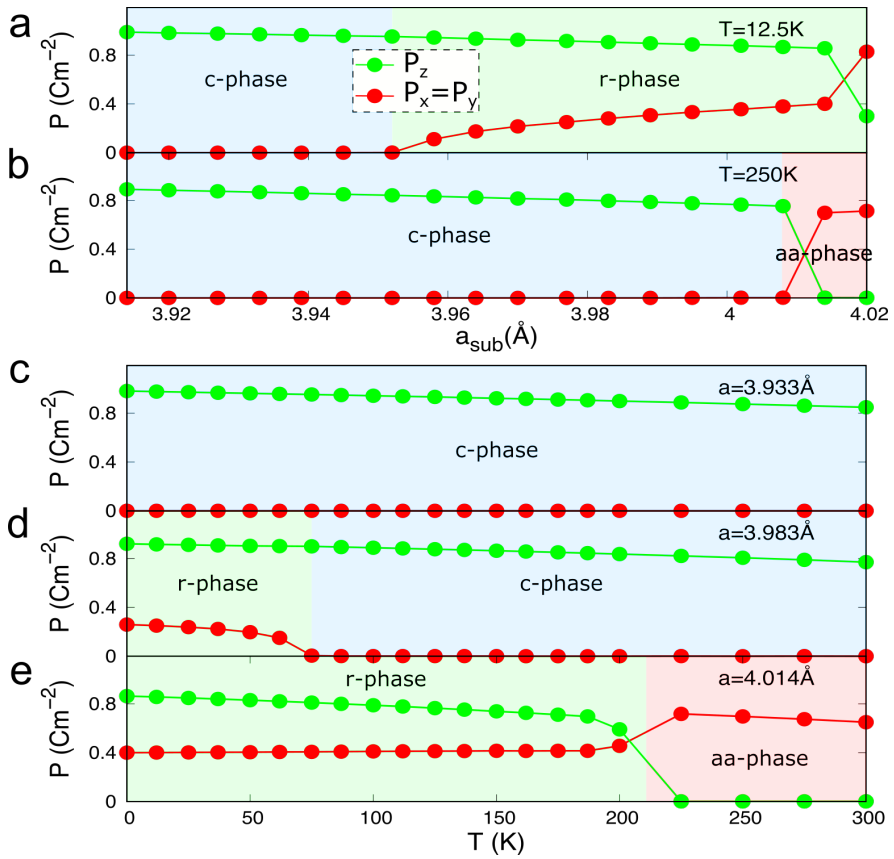

Figure 4.3: Calculated components of the average polarization (green circles represent the out-of-plane component $|P_z|$ and the red circles show the in-plane component of the polarization $|P_x| = |P_y|$). In panels [(a) and (b)] is presented the polarization at constant temperature, respectively $T = 12.5$ K and $T = 250$ K. The panels [(c)–(e)] we show the evolution of the polarization components for different in-plane lattices, respectively $a_{\mathrm{sub}} = 3.933$ Å, $a_{\mathrm{sub}} = 3.983$ Å and $a_{\mathrm{sub}} = 4.014$ Å.

predicted an intermediate phase at low temperature the formation of mixed domains of c and aa-phase without explicitly taking into account the additional cost of creating domain walls. So, we performed additional calculations of multidomain configurations at low-temperature and our results predict that these multidomain phases present a higher energy than the obtained for the r-phase.

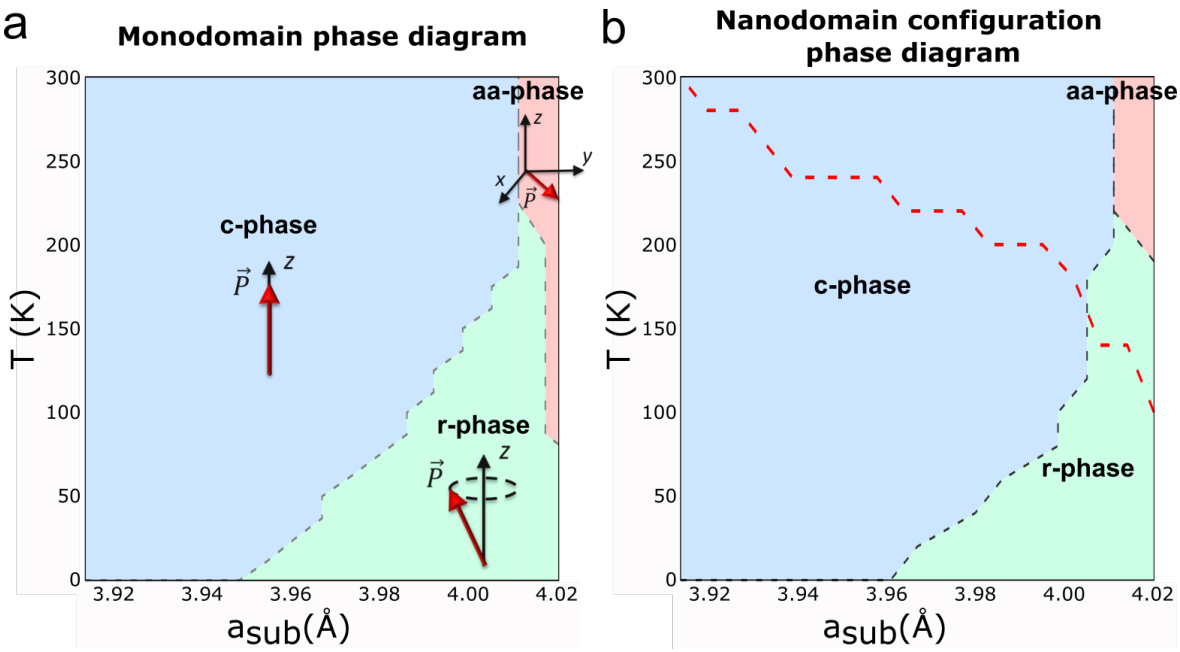

Figure 4.4: Structural phase diagram of $PbTiO_3$ monodomain (a) and ferroelectric nanodomain (b), where the colors green, blue and red represent the three different phases, respectively r-phase, c-phase and aa-phase. The red arrows are a sketch of the polarization direction in each phase observed. The red dashed line shows the critical temperature in which the nanodomain is destroyed.

4.2.2 Nanodomain and Electric skyrmion

In this section we present the structural phase diagram of the ferroelectric nanodomain configuration, applying a strategy similar to that presented in Section 4.2.1. In this case, the initial configurations considered are the results obtained at very low temperatures for the different epitaxial constraints presented previously in Chapter 3. Using second-principles methods we performed Metropolis Monte Carlo running 20,000 sweeps for thermalization and additional 80,000 sweeps to compute thermal averages. We used a periodically repeated supercell formed by 16×16×16 unit cells in which we have a nanodomain of 6×6×16.

Structural phase diagram

As we observed in the previous Section 4.2.1, the temperature and epitaxial strain play a main role in the direction and amplitude of the polar distortions. So to build the phase dia-

gram of the electric skyrmion configuration we calculate the thermal average of the polarization for each temperature and a_{sub}. From the second-principles simulations, we obtain a set of thermalized configurations that allow us to calculate the average configuration. From this configuration, we calculate the thermal average of the local polarization centered at several Pb atoms in the middle of the matrix.

The results obtained using this strategy are shown in Fig. 4.4 (b) where we present the structural phase diagram of the skyrmion configuration with the same three phases discussed in the phase diagram of $PbTiO_3$ monodomain (in Fig. 4.4 (a)). The presence of the nanodomain gives rise to minor changes in the boundaries between the different phases.

In addition to information about the stability of the different phases, we also include T_{ND}, which indicates the temperature at which the nanodomain disappears completely, as defined previously in Section 4.1. Note that this temperature is a characteristic of the nanodomain considered in this case. Thus, increasing or decreasing the size of this nanodomain, its destruction temperature should vary accordingly.

In the phase diagram, we do not have information about the polarization arrangement at the atomic level. In Fig. 4.5 (a) and (b) we show the average configuration obtained for two different points in the phase diagram. In Fig. 4.5 the panel (a) shows the nanodomain configuration in the r-phase where the polarization in-plane points along the four equivalent $\langle 110 \rangle$ directions breaking in 90° domains in-plane. In the c-phase (shown in Fig. 4.5 (b)) the polarization in the matrix and in the nanodomain points only along z and the only polarization in-plane appears in the NDW.

In short, the result obtained in the structural phase diagram is like that obtained in the case of the monodomain, showing that the presence of the nanodomain does not affect the obtained direction of the polarization inside the matrix.

Topological phase diagram

Temperature plays an important role in the topological character as shown in previous Section 4.1 with the results obtained for $a_{\mathrm{sub}} = a_{\mathrm{bulk}}$. When upon heating the electric skyrmion configuration, with a topological charge $Q = +1$, it undergoes several transitions involving

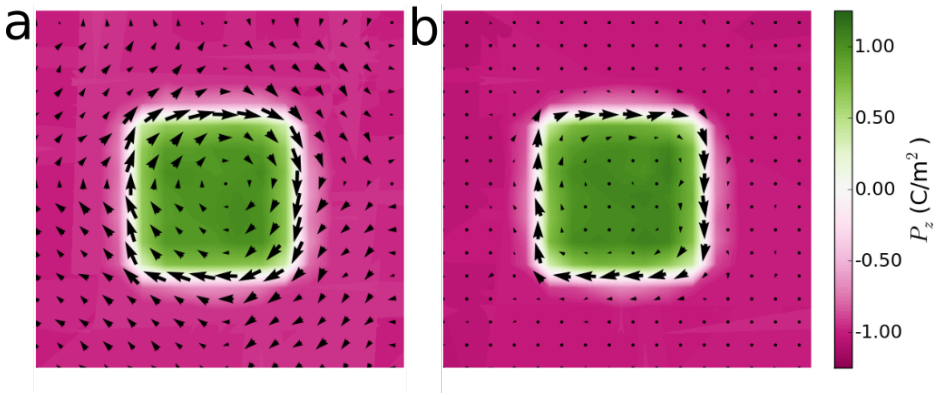

Figure 4.5: The polarization maps for two different in-plane lattices of $a_{\mathrm{sub}} = 3.983$ Å (a) and $a_{\mathrm{sub}} = 3.933$ Å (b) both at $T = 40$ K; the color scale gives the out-of-plane P_z component, while the arrows correspond to the in-plane P_x and P_y.

configurations with an unusual topology and trivial structures with a $Q = 0$. Such transitions allow us to define a critical temperature of skyrmion, T_{skyr} as defined in Section 4.1. Fig. 4.6 shows the topological charge evolution upon heating for several different in-plane lattice constants. In the Fig. 4.6 (a), we observe an abrupt transition from a skyrmionic state ($Q = +1$) to a trivial arrangement ($Q = 0$) at $T_{skyr} \sim 200$ K, obtaining a very narrow coexistence phase.

Decreasing the in-plane lattice for $a_{\mathrm{sub}} = 3.958$ Å, presented in Fig. 4.6 (b), the transition between skyrmionic state ($Q = +1$) and normal ($Q = 0$) nanodomain states is intermediate by a broader coexistence phase. In the coexistence phase, red region, we observe a distribution of different Qs obtained from our simulations, in which the most probable Q states are $+1$ and 0. However, we were able to identify in this phase Qs in the interval $Q \in [-1, 3]$. Then, the evolution of Q as a function of temperature let us identify two different transitions. The first transition from a skyrmionic phase to a coexistence phase at $T_{skyr} \sim 180$ K and a second transition from the coexistence to a monodomain configuration at $T_{ND} \sim 220$ K.

Fig. 4.6 (c) presents the distribution of Qs for $a_{\mathrm{sub}} = 3.920$ Å, where the nanodomain undergoes in the same sequence of transitions from skyrmionic state to a coexistence phase and finally to a monodomain configuration with the respective temperatures $T_{skyr} \sim 140$ K and $T_{ND} \sim 280$ K. On the coexistence phase, we obtained a broader distribution of Qs in an interval of $Q \in [-3, 4]$ where the $Q = -1, 0, +1$ are the most probable states of the ND.

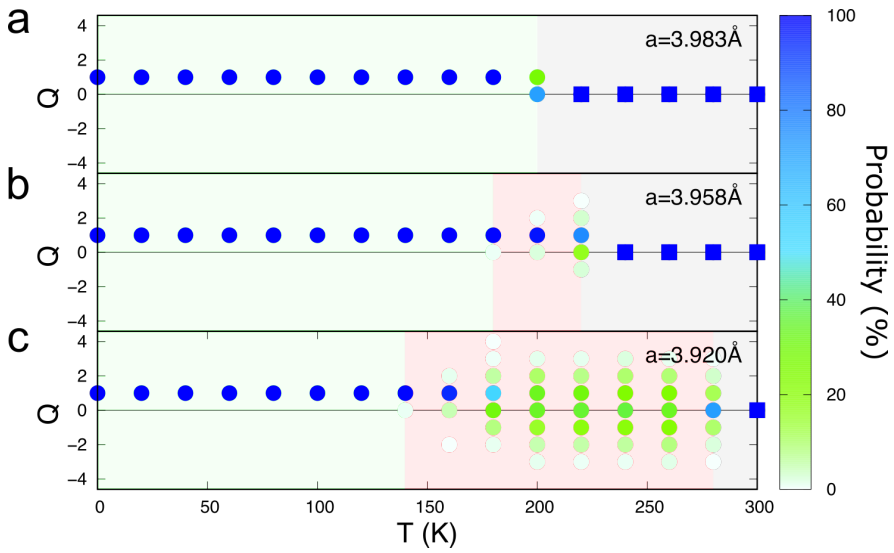

Figure 4.6: Probability distribution for Q as a function of T for three different in-plane lattices of $a_{\mathrm{sub}} = 3.983$ Å, $a_{\mathrm{sub}} = 3.958$ Å and $a_{\mathrm{sub}} = 3.920$ Å, respectively shown in the different panels [(a)–(c)]. The background colors show the different phases identified; white for the skyrmion phase; red for the coexistence phase; grey background the monodomain phase. The circles appear in the temperature range in which the configuration of the nanodomain exists and the squares indicate that the nanodomain has already been destroyed.

Therefore, we found that by decreasing the in-plane lattice parameter, we increased the temperature range of the coexistence phase. This result shows that using different substrates we have a tunable sequence of topological transitions - with or without a coexistence phase. This behavior can be understood when we think about the effect of the restrictions imposed by the substrate in the polarization. In the case of tensile strain, a big component of the polarization in the xy plane is not only confined to the NDW, but also along the matrix and nanodomain forming the 90° domains. So, the thermal fluctuations must disorder this whole arrangement in-plane to destroy the $Q = +1$ skyrmion. On the other hand, the polarization out-of-plane decreases for tensile strains and therefore it is easier to destroy the nanodomain than to destroy the pattern of domains in-plane. So, for tensile strain the coexistence phase is very narrow.

When applying a compressive stress, we verify that the polarization in the nanodomain and in the matrix is parallel to z in c-phase. When we decrease the in-plane lattice param-

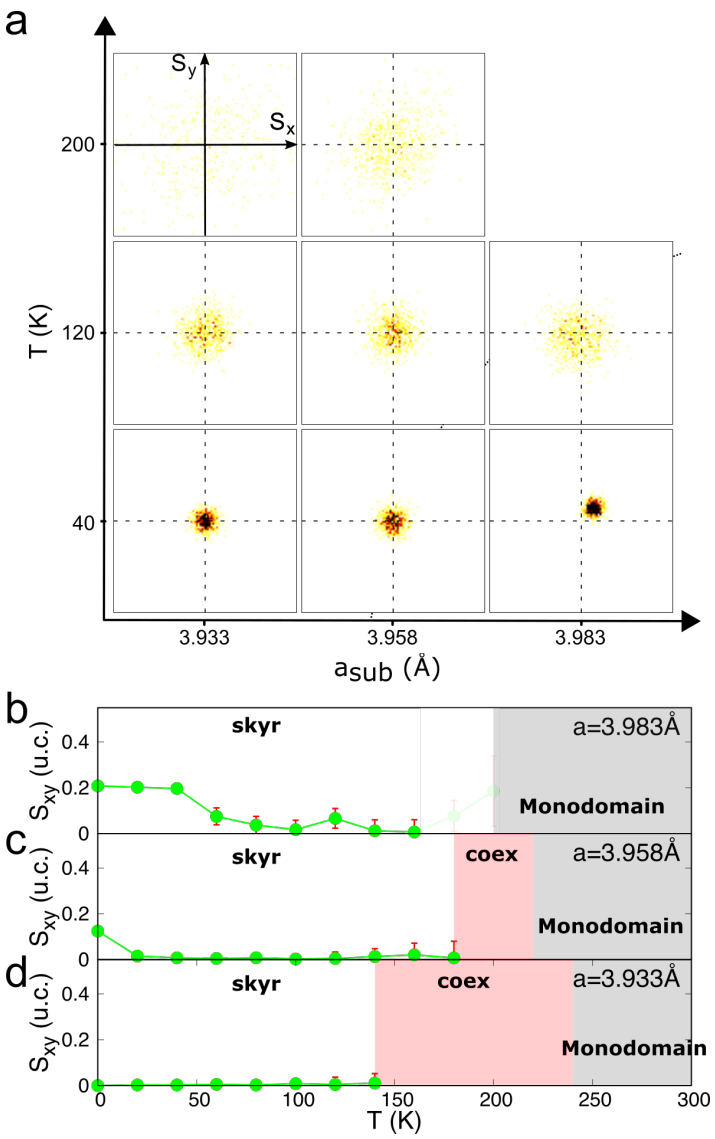

Figure 4.7: Sketches of (a) the histograms of the skyrmion center as a function of temperature and epitaxial strain in-plane, where the horizontal dash line represents $S_x = 0$ and the vertical the $S_y = 0$; Panels (b)–(d) the average of the position of the skyrmion center, $|\langle S_{xy} \rangle|$, for three different in-plane lattices of $a_{\text{sub}} = 3.983$ Å, $a_{\text{sub}} = 3.958$ Å and $a_{\text{sub}} = 3.933$ Å, respectively.

eter, P_z increases and this explains why the temperature of destruction of the nanodomain increases. However, for these epitaxial restrictions, only in the NDW the polarization is in-plane. By decreasing the in-plane lattice parameter this polarization in the NDW decreases

in magnitude. This way, thermal fluctuations can disorder the confined polarization confined in the NDW, giving rise to the coexistence phase at lower temperatures. Therefore, by decreasing the in-plane lattice parameter, simultaneously, we increase the stability of the nanodomain and at the same time we decrease the stability of the ordered closed loop of polarization in the NDW giving rise to a broader coexistence phase in temperature.

In addition, another important property of the electric skyrmion configuration is the position of the skyrmion center. The previous study regarding the center of the skyrmion at low-temperature in Chapter 3 showed a symmetry-breaking skyrmion-skyrmion transition driven by epitaxial strain, due to the off-centering of the skyrmion.

Fig. 4.7(a) shows the histograms of the center of the skyrmion. Applying compressive strain in-plane xy the center moves around the zero which implies a high-symmetric skyrmion. When applied a tensile epitaxial strain the distribution of the center moves off-center.

The effect of the temperature on the movement of the skyrmion center is more evident in Fig. 4.7 (b) in which we show the average of the position of the skyrmion center, $|\langle S_{xy}\rangle|$, for $a_{\mathrm{sub}} = 3.983$ Å. We can identify a first region with non-zero $|\langle S_{xy}\rangle|$ below $T_S = 80$ K, where T_S is the temperature associated with this transition. When heated up, the thermal fluctuations induce a topological transition to a high-symmetric skyrmion ($|\langle S_{xy}\rangle| \approx 0$). Fig. 4.7 (c) shows the S_{xy} for $a_{\mathrm{sub}} = 3.958$ Å. We observe a similar behavior, but the critical temperature associated with the transition regarding the movement of the center is reduced to $T_S = 20$ K. As expected for a compressive epitaxial strain the movement of the skyrmion is more costly, such can be seen in Fig. 4.7 (d) where the $S_{xy} = 0$ all over the skyrmion phase. It is important to emphasize that for all in-plane lattice constants studied; the increase of the temperature leads to wider distributions of the skyrmion center.

Considering all the information regarding the different topological phases presented in Fig. 4.6 together with the transition of the skyrmion center, Fig. 4.7, we can construct the topological phase diagram of the skyrmion, taking into account the structural phase diagram described in Section 4.2.2. Fig. 4.8 assembles all the details about the topological transitions. At low temperatures, we identified two different phases. A first region for $a_{\mathrm{sub}} < 3,983$

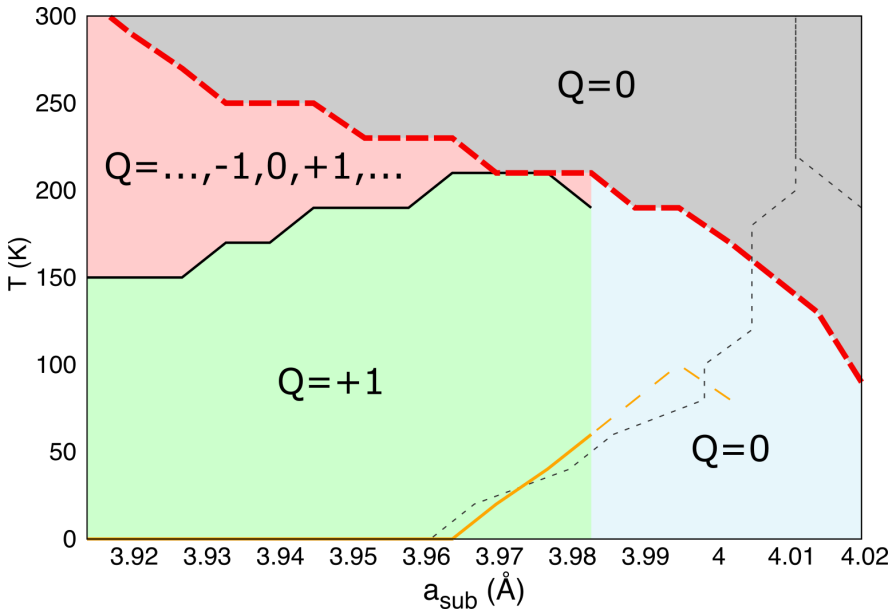

Figure 4.8: Topological phase diagram of ferroelectric ND; colors green, light blue, red and grey representing the different topological phases, respectively skyrmion phase, dipole phase, coexistence phase and trivial phase. The grey dashed lines show the structural transitions, red dashed line represents the critical temperature of the ND, the orange solid line shows the transition of the position of the skyrmion center and the orange dashed line represents the same transition in the region where skyrmion is a stable solution but it is not the most stable state of the ND state. To define the different phases, we had introduced a tolerance factor of 2% defining the minimum $\%$ where we consider such state. Regarding the transition of the position of the skyrmion center we consider the movement only when it is $> 0.05 u.c.$

Å where the skyrmion is the stable solution and a second region when $a_{\mathrm{sub}} > 3,983$ Å, where the polar state NDW is the most stable solution of the ND configuration. Nevertheless, in our simulations, we did not observe any spontaneous transition from a NDW-skyrmion state to NDW-polar state, which indicates that between these states we have a large energy barrier.

4.3 Macroscopic signatures of structural and topological transitions

In the phase diagrams previously discussed we reported several transitions regarding rotations of the polarization and topology that should have associated signatures in the dielectric response. These signatures assigned to the different transitions should be possible to observe experimentally.

4.3.1 Monodomain

The results obtained for $PbTiO_3$ are presented in Fig. 4.9 (a) and (b). In the panel (a) we show the dielectric response in-plane, $\chi_{xx} = \chi_{yy}$, where we observed a maximum for tensile epitaxial strain in-plane that coincide with the transition between the c-phase and r-phase. Combining the almost divergence of the dielectric response with the polarization profile previously shown in the Fig. 4.3 (a), we have the indication that this transition presents a second-order character.

Besides that, the χ_{xx} also presents smaller peaks in the c- to aa-phase transition and in the r- to aa-phase (more difficult to identify in the logarithmic scale). Such transitions are most easily observed in Fig. 4.9 (b) in which we present χ_{zz}. Taking into account the polarization profile in these transitions – shown in Fig. 4.3 (e) with the c- to aa-phase transition – it seems to be an abrupt transition, which indicates that this transition is more similar to a first-order transition.

4.3.2 Nanodomain and Electric skyrmion

In the phase diagrams discussed before, we report several transitions related to the structural changes and the associated signatures in the dielectric response. In this section, we will focus on the different topological transitions and identify their macroscopic dielectric signatures.

Let us first compute the macroscopic dielectric response of the nanodomain configura-

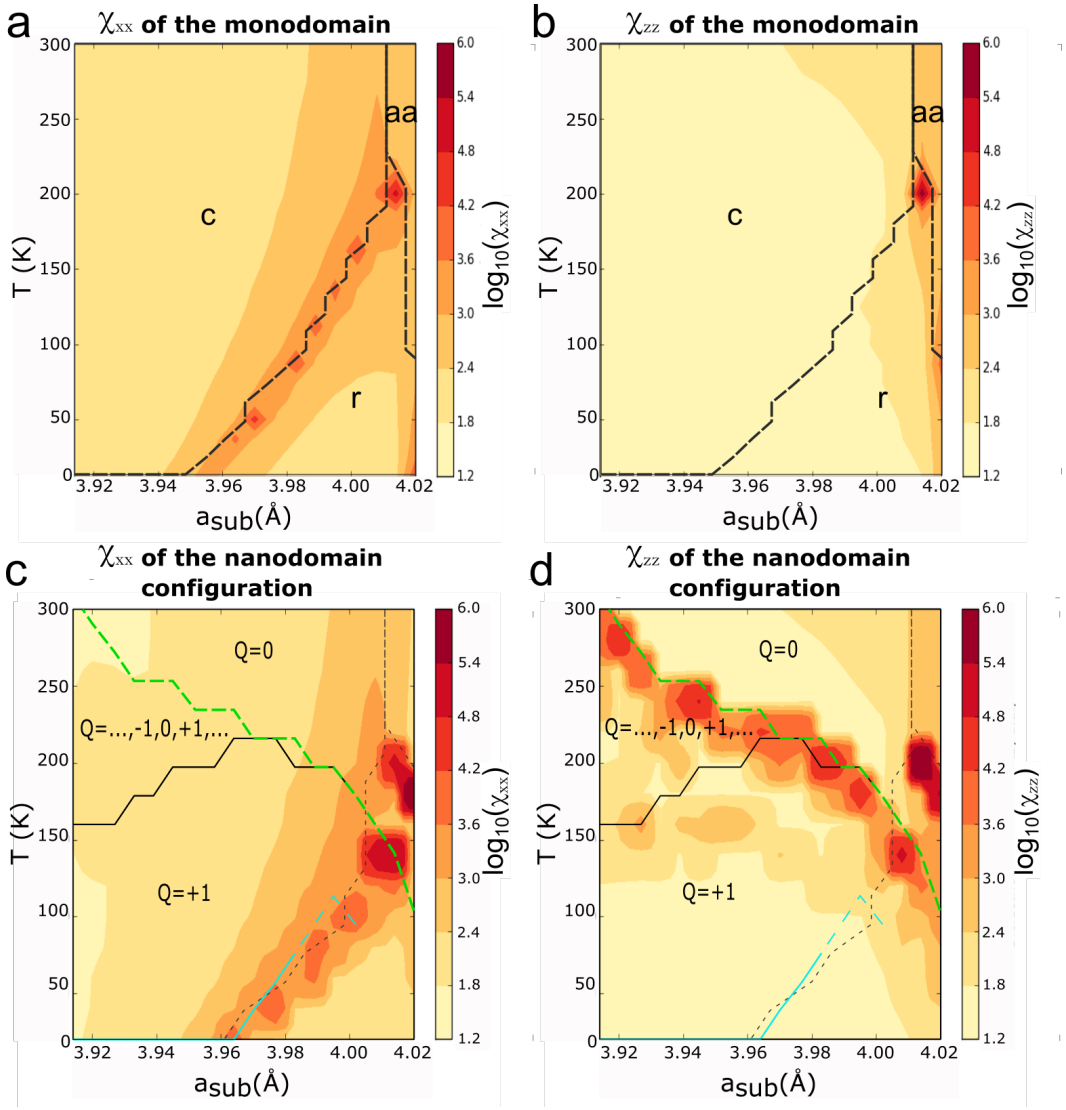

Figure 4.9: Calculated dielectric response diagram of the $PbTiO_3$ monodomain [(a)–(b)] and nanodomain [(c)–(d)] as a function of temperature and a_{sub} (obtained using the strategy presented in Appendix B); The panels (a) and (c) correspond to the dielectric response in-plane, $\chi_{xx} = \chi_{yy}$; (b) and (d) are the dielectric responses out-plane, χ_{zz}. The color scale represents the log_{10} of the respective dielectric responses. The dashed lines represent the limits of the different structural phases. In the panels (c) and (d) the black lines represent the limits of topological phases; the green dashed line represents the destruction of the ND and the blue dashed line corresponds to the transition of the skyrmion center.

tion in bulk $PbTiO_3$, simplifying the problem by eliminating the effect of the epitaxial strain. In Section 4.1 we showed how temperature induces several transitions.

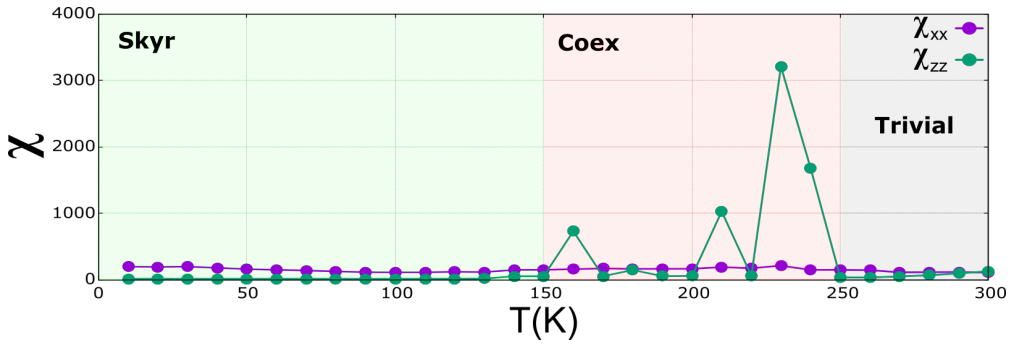

Figure 4.10: Calculated diagonal dielectric response of the electric skyrmion in bulk $PbTiO_3$ as a function of temperature. The magenta circles represent the χ_{xx} and the green circles are χ_{zz}.

In Fig. 4.10 we show the macroscopic dielectric response of the nanodomain configuration. The component in plane χ_{xx} remains almost constant and does not allow us to identify any dielectric anomaly as well as we obtained for the monodomain case (in Fig. 4.9 (a)). However, when we consider the other component χ_{zz}, we identified three different anomalies. The first at $T \sim 160$ K where we observe a peak in the dielectric response in the proximity of T_{skyr}. Two other peaks were obtained, first in the middle of the coexistence phase ($T = 210$ K) and the second closest to T_{ND}. This last peak is associated with the transition from the coexistence phase to a monodomain phase. Finally, the peak obtained at $T = 210$ K appears in the coexistence region. This peak is located close to the temperature at which the shape of the nanodomain begins to be distorted ($T = 220$ K). This seems to be the explanation for this peak obtained in the middle of the coexistence phase.

The situation is more complex when we consider the effect of the epitaxial strain. As we discussed in Section 4.2.2, there are three regions where we identified topological transitions associated to: i) coexistence to skyrmionic phase (T_{skyr}), (ii) the skyrmion center (T_S), and iii) destruction of the nanodomain (T_{ND}). Therefore, let us analyze each of these regions and their respective dielectric responses and compare with the results of the $PbTiO_3$ monodomain.

Coexistence to skyrmionic phase (T_{skyr})

In this topological transition, the different components of the dielectric response exhibit different behaviors. With regard to the χxx (in Fig. 4.9 (c)) we verify that the transformation in the topology does not have any anomaly in the dielectric response. On the other hand, the χ_{zz} (presented in Fig. 4.9 (d)) presents a maximum, that does not appear in the monodomain dielectric response. In this region, the peak in the response follows the T_{skyr} line, although it is shifted to lower temperatures. Interestingly, the local dielectric response χ_{zz} (obtained using the strategy presented in Appendix C), in Fig. 4.11 (c), presents a maximum in the NDW. This result is consistent with an order-disorder transition in the NDW. Note that huge peaks of χ_{zz} are observed in three corners of the nanodomain. Such a response appears due the fact that in this region of the phase diagram the external electric field is strong enough to flip the polarization of the nanodomain corners, turning the polarization along z from positive to negative (now part of the matrix).

Thus, we identified a signature in the dielectric response seems to be related to the topological transition within the NDW. The relationship is not fully established, as the peak in χ_{zz} occurs at temperatures lower than the observed T_{skyr}. Nevertheless, while we still lack a more detailed understanding, it seems that the connection between these two features is clear. Hence, we believe that this dielectric anomaly may allow the experimental identification of the presence of skyrmions.

The skyrmion center (T_S):

Fig. 4.9 (c) and (d) show the different components of the dielectric response of the electric skyrmion. When we investigate the results obtained in the region – where we observe the skyrmion-skyrmion transition due to the off-centering of the skyrmion center – we verify that these are like those obtained in the monodomain case. This is because, as we discussed earlier in Chapter 3, the off-centering of the skyrmion center is driven by the rotation of the polarization in the transition from c- to r-phase. Thus, the dielectric signature of the nanodomain in this region is mainly defined by the structural transition.

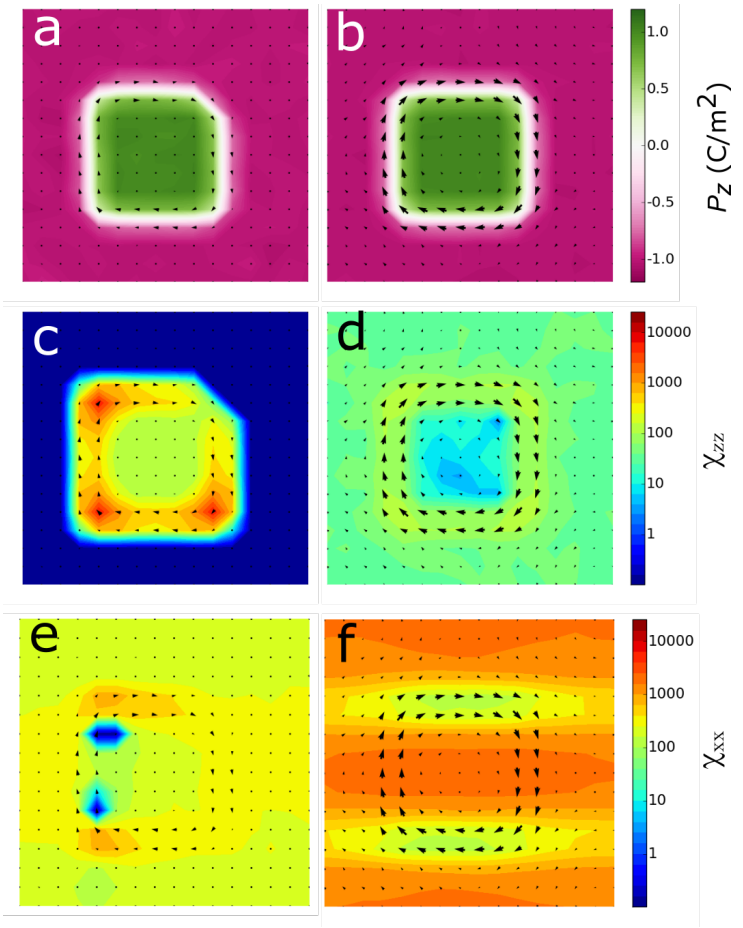

Figure 4.11: Calculated polarization [(a) and (b)] and local electric susceptibility maps χ_{zz} [(c) and (d)] and χ_{xx} [(e) and (f)] for two different points in the phase diagram; transition of the center of the skyrmion ($a_{\text{sub}} = 3.970$ Å, $T = 40$ K) (a),(c) and (e); transition from skyrmion phase to coexistence phase ($a_{\text{sub}} = 3.933$ Å, $T = 160$ K) (b),(d) and (f). In panels [(a) and (b)] the color scale gives the out-of-plane P_z component, while the arrows correspond to the in-plane P_x and P_y. In panels [(c)–(f)] the color scale gives the $\chi_{zz}(x, y)$ or $\chi_{xx}(x, y)$ while the arrows correspond to the in-plane P_x and P_y.

Even knowing that in this region the dielectric response is dominated by structural transformation, the study of the local response of the nanodomain configuration can reveal unique characteristics of the nanodomain configuration. Fig. 4.11 (b), (d) and (f) show the polarization arrangement and the components of the local dielectric response. Focusing on χ_{zz} results we can identify two regions with different responses. The first region is at the matrix and nanodomain, where the biggest component of the polarization is P_z, and this component

is hard to change and therefore we obtain a small χ_{zz}. The second is in the NDW formed by polarization in-plane, in which we observe the maximum of the χ_{zz}, showing that NDW is the most reactive part of the nanodomain configuration.

The panel (f) show the response of the same region of the phase diagram when applied an external field along x. In these conditions the center of the skyrmion moves perpendicular to the direction of the electric fields as we showed previously in Chapter 3. Fig. 4.11 (f) presents the local electric susceptibility in which we observe the maximum in the part of the NDW with local polarization along y, in the vortices of polarization in the matrix and in the center of the ND.

Destruction of the nanodomain (T_{ND})

When comparing the dielectric response of the monodomain and the nanodomain configuration in this region, it is easy to identify a clear difference in the χ_{zz} (Fig. 4.9 (b) and (d)). In this region we observe the destruction of the nanodomain and the transition from a monodomain phase to the coexistence phase. This anomaly in the dielectric response is a consequence of the variation of the average polarization over z due to the destruction of the nano domain.

4.4 Summary

In this chapter, we studied the stability of the electric skyrmion obtained in the nanodomain configuration, considering the temperature effect. We predicted that at high temperatures the nanodomain is destroyed and, consequently, we obtain a trivial arrangement. At lower temperatures, the nanodomain is stable and we observe that thermal fluctuations give rise to a phase in which several values of Q coexist. Finally, we observed the transition from a coexistence phase to the skyrmionic phase. We show evidence that this topological transition is associated to an anomaly in the macroscopic dielectric response. Considering different substrates, the results showed that the phase sequence is tunable, with or without the coexistence phase, which disappears for tensile epitaxial strains.

Chapter 5

Electric skyrmions in superlattices of $PbTiO_3$/$SrTiO_3$

In this chapter, we report the discovery of electric skyrmion bubbles in lead titanate layer confined by strontium-titanate layers. We start by introducing the concept of superlattices and the different factors that define their properties, illustrated with several examples from the literature specifically for $PbTiO_3$/$SrTiO_3$ superlattices. Focusing on our objective, then we briefly describe the different experimental results that allowed to prove the existence of electric skyrmions at room temperature in $PbTiO_3$/$SrTiO_3$ superlattices. Finally, we describe the theoretical study carried out using the second-principles and how they allowed us to describe and understand more better the electronic skyrmions at the structural and topological level.

5.1 Ferroelectric-Paraelectric superlattices

In recent years, experimental developments in the growth of complex heterostructures with high quality have created the possibility of studying these new complex materials. Throughout this chapter, we will focus on a specific type of heterostructures, the superlattices that are formed by a periodic structure with two materials, which are alternately layered, as shown in

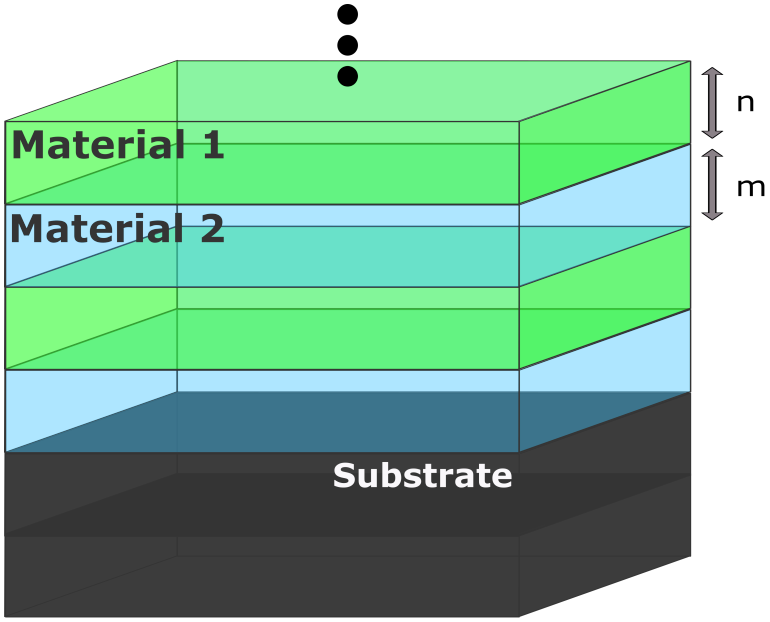

Figure 5.1: Sketch of a superlattice formed by two different materials represented by the green and blue layers where n and m are the thickness of layers in unit cells. The black material is the substrate of the superlattice

Fig. 5.1. Usually, these layers are very thin with few unit cells.

These heterostructures can not only allow the possibilities to improve or control the properties of one of the materials present in the superlattices, but also give rise to new properties that we do not observe in the materials individually. For example, in the case of superlattices formed by $BaCuO_2$ and $SrCuO_2$, superconductivity was observed, even though none of the materials present superconductivity in itself [52], or in superlattices $SrZrO_3$ and $SrTiO_3$ that exhibit ferroelectricity when none of these materials is ferroelectric [53].

In this work, we will focus on superlattices where we combine a ferroelectric and a dielectric material. In these superlattices the main factors defining the ground state are: (i) the epitaxial stress imposed by the substrate, (ii) the interface and how the atoms relax in this region, and (iii) the electrostatic interactions between the different materials.

Neaton and Rabe [86] showed the importance of epitaxial strain in the study of $BaTiO_3$/$SrTiO_3$ superlattices grown epitaxially on a $SrTiO_3$ substrate. They found that for very thin layers of $BaTiO_3$ and $SrTiO_3$, the entire superlattice is homogeneously polarized – including $SrTiO_3$

an incipient ferroelectric – as a result of electrostatic interactions between different materials. In addition, due to the compressive stress applied in-plane – in the $BaTiO_3$ layers - the superlattices $(BaTiO_3)_2/(SrTiO_3)_3$ (the indexes define the thickness of the different layers in unit cells) show an increase of more than 50% in the polarization magnitude when comparing with the value obtained for the bulk of $BaTiO_3$. These results have been demonstrated experimentally with an enhancement in polarization in $BaTiO_3$ [87, 88].

In the case of the $PbTiO_3/SrTiO_3$ superlattices – in which we will focus on throughout this chapter – the electrostatic interactions between the different layers is one of the most important factors to define the final polarization state. $PbTiO_3$ presents a ferroelectric phase with a tetragonal structure. In the case of $SrTiO_3$, it has a non-polar phase at low temperatures with a tetragonal structure. In addition, the in-plane lattices of these materials in their tetragonal phases are very similar, which facilitates the experimental construction of these superlattices and allows us to minimize the effect of epitaxial strain choosing $SrTiO_3$ as a substrate. With these epitaxial constraints $PbTiO_3$ layers are compressed in-plane and as a consequence they develop a polarization only out of plane, parallel to the stacking direction.

The effect of electrostatic interaction can be understood using a simple model introduced by Junquera and Ghosez [89]. This model was used to study the critical thickness of ferroelectricity in ultra thin films, however, it can be easily generalized to study superlattices. Thus, considering a superlattice formed by ferroelectric layers with n unit cells, and a layer of a paraelectric material with m unit cells. The total thickness of the bilayers formed by these two materials is given by $t_{FE} + t_{PE} = nc_{FE} + mc_{PE}$ in which c_{FE} and c_{PE} are the lattice parameters of the materials. In the absence of an external electric field the total energy of the superlattice is given by:

$$E(P_{FE}, P_{PE}) = U(P_{FE}, P_{PE}) + E_{elec} \tag{5.1}$$

The first term corresponds to the internal energy of the superlattice in the absence of any electric field and the second term is the electrostatic energy due to the interaction between the different layers. So we can write the first term as a sum of the energies of each of

the materials when calculated under the same conditions of epitaxial strain. In addition, it is important to bear in mind that in this model we will neglect the impact of the interface on the problem, assuming that it is much smaller than the electrostatic interaction. Thus $U(P_{FE}, P_{PE})$ can be rewritten as:

$$U(P_{FE}, P_{PE}) \approx nU(P_{FE}) + mU(P_{PE}) \tag{5.2}$$

In the superlattice in the absence of free charges, the development of a polarization P_{FE} in the ferroelectric material gives rise to an electric field $\mathcal{E}_{FE}$ – a depolarization field. Taking into account that in our problem the superlattice is in a short circuit condition, then the paraelectric layer will have to develop a depolarization field $\mathcal{E}_{PE}$ in order to keep the total variation of the electric potential null, and therefore we can write:

$$t_{FE}\mathcal{E}_{FE} = -t_{PE}\mathcal{E}_{PE} \tag{5.3}$$

In addition, in the absence of free charges the condition $\nabla \cdot D = 0$ is imposed and from this we obtain that:

$$P_{FE} + \varepsilon_0\mathcal{E}_{FE} = P_{PE} + \varepsilon_0\mathcal{E}_{PE} \tag{5.4}$$

Combining these two equations we obtain the depolarization field given by:

$$\begin{aligned} \mathcal{E}_{FE} &= -\frac{t_{PE}}{\varepsilon_0(t_{FE} + t_{PE})}(P_{FE} - P_{PE}), \\ \mathcal{E}_{PE} &= +\frac{t_{FE}}{\varepsilon_0(t_{FE} + t_{PE})}(P_{FE} - P_{PE}) \end{aligned} \tag{5.5}$$

As shown in the previous equations if the polarizations in the two materials are different, two electric fields with opposite signs appear in each material and their magnitude will depend on the relative thickness of each of the materials and the difference of the polarizations $P_{FE} - P_{PE}$.

Taking this result into account, we can calculate the electrostatic energy due to the interaction between the different layers which is given by $E_{elec} = -\sum_i t_i\mathcal{E}_i \cdot P_i$ where i runs over

all the layers in the superlattice. So we obtain

$$E_{elec} = \frac{t_{FE}t_{PE}}{\varepsilon_0(t_{FE}+t_{PE})}(P_{FE}-P_{PE})^2 \tag{5.6}$$

Finally, replacing the results obtained for each of the terms in Eq. 5.1 the total energy of the superlattice is given by:

$$E(P_{FE},P_{PE}) = nU(P_{FE}) + mU(P_{PE}) + \frac{t_{FE}t_{PE}}{\varepsilon_0(t_{FE}+t_{PE})}(P_{FE}-P_{PE})^2 \tag{5.7}$$

Therefore, according to this simple model, we have three key factors to define the final polarization state of the superlattice. First, the ferroelectric material minimizes its energy by developing a spontaneous polarization. Second, the energy cost of polarizing the paraelectric material. And finally, the electrostatic cost of having different polarization in each of the materials. The balance of the different factors is defined by the relative thickness of the different materials in the superlattice.

From the literature on $PbTiO_3$/$SrTiO_3$ superlattice, we verify that its behavior can be understood taking into account the previous model with reasonable agreement. When the paraelectric layer is very thin the superlattice develops a uniform polarization in both materials. As we can see from Eq. 5.7, this way the depolarization fields are eliminated with the additional cost of polarizing the layers of $SrTiO_3$ [86, 90, 91].

When we increase the thickness of the paraelectric layer, the cost of polarizing this material increases. So in these superlattices, when the $SrTiO_3$ layer is sufficiently thick, the P_{STO} will be null. If we consider the cases where the layers of $PbTiO_3$ has a uniform polarization inside – as we show in Fig. 5.2 (a) – we will obtain large depolarization fields as shown by Eq. 5.5.

In order to minimize the depolarization fields, the polarization inside each $PbTiO_3$ layer would prefer to break into different domains with polarization pointing up and down, as shown in Fig. 5.2. This solution allows to obtain a total P_{PTO} that is zero. This way, the difference $P_{PTO} - P_{STO} = 0$ and therefore the total depolarization fields given by Eq. 5.5 are null in both materials. However, when the material breaks in domains, other factors must be taken

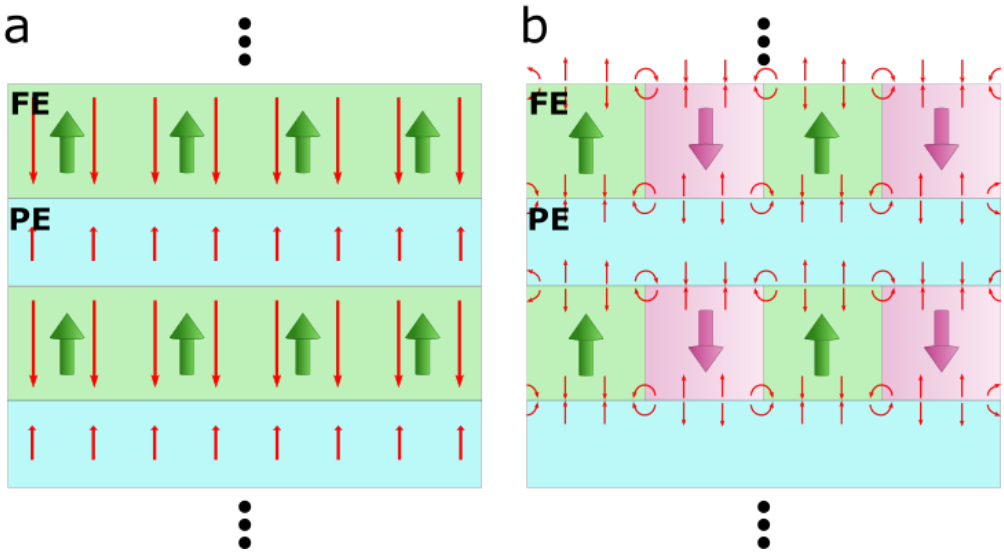

Figure 5.2: Sketch of the $PbTiO_3/SrTiO_3$ superlattices with a (a) monodomain polarization inside the $PbTiO_3$ layer and (b) with the multidomain configuration inside the $PbTiO_3$ layer. The green and magenta arrows represent the polarization and the red arrows represent the depolarization fields created for each polarization state.

into account, first is the energy of the domain walls and second the width of the domains. The balance between these factors depends on the thickness of the layers and leads to a configuration that follows Kittel's law initially applied to ferromagnetic domains [92] and later applied to ferroelectric domains [93, 94].

Aguado-Puente and Junquera [4] studied the properties of the 180° stripe domains in superlattices of $PbTiO_3/SrTiO_3$ using first-principles calculations (shown in Fig. 1.8 (b)). Under these epitaxial constraints, $PbTiO_3$ would present a tetragonal structure with polarization only along z. So as discussed previously in this section, to avoid depolarization fields, the polarization in $PbTiO_3$ breaks in domains up and down. The result obtained presents a complex structure with different domains. Between them polarization vortices are formed around the domain walls as shown in Fig. 1.8 (b). In addition, to avoid creating depolarization fields at the interface, the polarization rotates continuously in-plane. In order to accommodate such rotation around domain walls and interface the material develops large strain gradients.

5.2 Experimental studies of the structure of $PbTiO_3$/$SrTiO_3$ superlattices

Previous works

Experimentally, the existence of ordered ferroelectric nanodomains in the superlattices of $PbTiO_3$/$SrTiO_3$ grown on a $SrTiO_3$ substrate was verified, using X-ray diffraction and transmission electron microscopy [55, 56, 57] in Fig. 1.8 (a). The analysis of tetragonality along the superlattice and the comparison with the theoretical results predicted the complex structure of the nanodomains with the continuous rotation of the polarization at the interface and around the domain walls [4].

In the sequence of these studies, it was verified experimentally that in these superlattices of $(PbTiO_3)_5$/$(SrTiO_3)_n$ different domain structures like ferroelectric stripes formed in the layer of $PbTiO_3$ [5]. Along with the experimental studies, second-principle methods were also used to study these domain structures that we present in the Fig. 1.8 (c). This figure shows the planar-view of the stripe configuration from above. The different local properties presented in this study, such as polarization, susceptibility and dielectric response, were obtained using second-principles methods applied for the first time in the study of superlattices. In the next sections the theoretical results presented were obtained using the same model, described in more detail in Chapter 2.

In a similar structure with superlattices $PbTiO_3$/$SrTiO_3$ grown on a substrate of $DyScO_3$ the existence of polar vortices confined in the layers of $PbTiO_3$ was discovered [3]. Using cross-sectional high-resolution scanning transmission electron microscopy (HR-STEM), a structure composed of pairs of left and right handed vortices was observed as we show in Fig. 1.8 (a). Besides that, using resonant soft X-ray diffraction and second-principle simulations, a strong circular dichroism was observed, due to the interaction of the polar vortices with the circularly polarized light, showing that these structures are chiral [8].

Later studies, the coexistence at room temperature of the polar vortices phase and the ferroelectric phase with domains a_1/a_2 was observed [95]. Applying electric fields in the mixed phase it is possible to favor one of the phases, abruptly changing the properties of the

superlattices.

In the following sections we will study the possibility of stabilizing electric skyrmions in superlattices of $PbTiO_3$/$SrTiO_3$ that present themselves as strong candidates.

Observation of electric skyrmion in $PbTiO_3$/$SrTiO_3$ superlattices

As we showed in the previous section, the $PbTiO_3$/$SrTiO_3$ superlattices are structures able to stabilize complex multidomains arrangements. Therefore, they are a strong candidate for stabilizing structures such as electrical skyrmions. Then by combining the new experimental resources with theoretical predictions, electrical skyrmions were observed experimentally at room temperature in $PbTiO_3$/$SrTiO_3$ superlattices grown on a substrate of $SrTiO_3$ [7]. In this section, we will show the different experimental results that indicate the existence of electric skyrmions.

The first evidence comes from the dark-field transmission electron microscopy (DF-TEM) images, showing the cross-sectional and planar view of the circular nanodomains confined in the $PbTiO_3$ layers (in Fig. 5.3). Using three-dimensional reciprocal space mapping was identified a peak associated to the superlattice periodicity demonstrating the high quality of the superlattices used. The observed satellite peaks were assigned to the in-plane periodicity of about 8 nm, consequence of the ordered arrangement of ferroelectric nanodomains confined in the $PbTiO_3$ layers.

Fig 5.4 shows the displacement vectors of the Ti atoms. These results show the converging and diverging polarization arrangements observed at top and bottom interfaces. Such arrangements of the polarization prove the existence of electric Néel skyrmion (described in Chapter 1) in the superlattice interfaces between the $PbTiO_3$ and $SrTiO_3$ layers.

However, in the middle layers of $PbTiO_3$ there was no evidence of the Bloch component of the polarization in the domain wall. Without this component of the polarization forming a closed surface of polarization around the nanodomains, the middle planes of $PbTiO_3$ layers are trivial topological textures with a topological charge of $Q = 0$. On the other hand, using second-principles simulations we were able to describe in detail the structure of the domain walls – as we showed in Chapter 3 – identifying the closed surface of polarization around

the nanodomains (these results will be discussed in the next section). Based on our theoretical predictions that describe the displacements of different atoms in the superlattice, the group of D.A. Muller in Cornell determined that it should be possible to observe such polarization pattern by combining high-angle annular dark-field scanning transmission electron microscopy (HAADF-STEM) images and four-dimensional scanning transmission electron microscopy (4D-STEM). Fig 5.4(c)–(f) show the 4D-STEM images demonstrating the existence of such component of the polarization. Another indication of the Bloch polarization confined in the domain walls was obtained using resonant soft X-ray diffraction experiments showing circular dichroism confirming chirality. Such result only appears in the nanodomain configuration if the domain wall polarization forms a closed loop of polarization around the nanodomain.

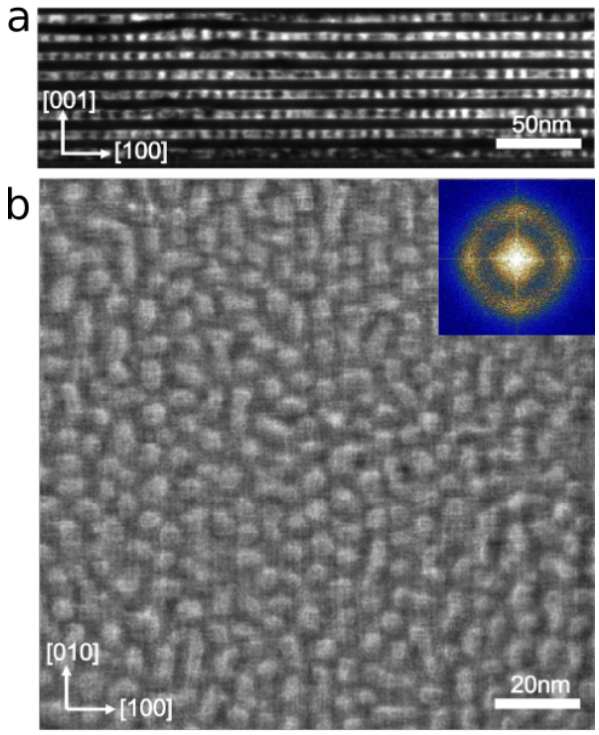

Figure 5.3: Ordered nanodomains arrangements observed using Cross-sectional DF-TEM images in $(SrTiO_3)_{16}$/(PbTiO3)$_{16}$ superlattices, showing an in-plane modulation of about 8 nm. Planar-view DF-STEM imaging shows the circular nanodomains. Figure adapted from reference [7].

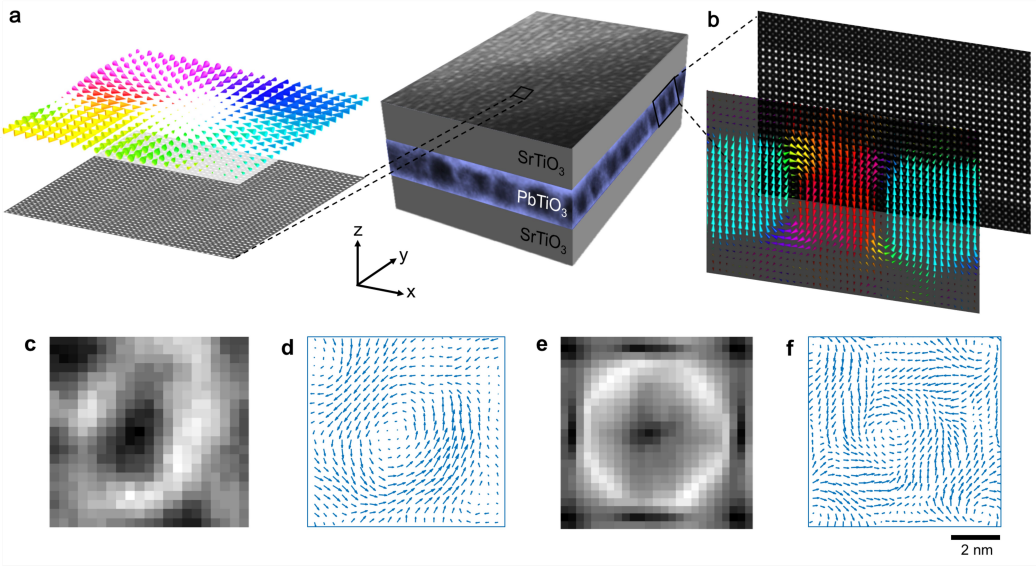

Figure 5.4: Reversed Ti displacement vector maps (top) based on atomic resolved plan-view HAADF-STEM image (bottom) of a circular nanodomain in $(SrTiO_3)_{16}/(PbTiO_3)_{16}/(SrTiO_3)_{16}$ trilayer, form a structure like a Néel skyrmion structure. Panel (b) presents the Ti-displacement vector map (front) obtained from the atomically resolved cross-sectional HAADF-STEM image (back), showing the circular nanodomain and the matrix with the up and down polarization. The 4D-STEM image of a $(SrTiO_3)_{16}/(PbTiO3)_{16}$ superlattice gives the ADF image (c) and maps of polar order using the probability current flow (d), which were reconstructed from the same 4D dataset. Panels (e) and (f) are Multi slice simulations of the beam propagation through the structure. The ADF image (e) and the probability current flow (f). The signals are not simple projections, but weighted by electron beam channelling towards the middle of the skyrmion bubble, where the polarization exhibits a Bloch-like character. Figure adapted from reference [7].

This experimental result proves the existence of a stable electric skyrmion in $(PbTiO_3)/(SrTiO_3)$ superlattices obtained at room temperature.

5.3 Theoretical study of electric skyrmion in $PbTiO_3/SrTiO_3$ superlattices

In parallel with the experimental investigation presented in the previous section, we began the study of these superlattices of $PbTiO_3/SrTiO_3$ in order to understand and complement the experimental results with the detailed description of the structure at the atomic level. We

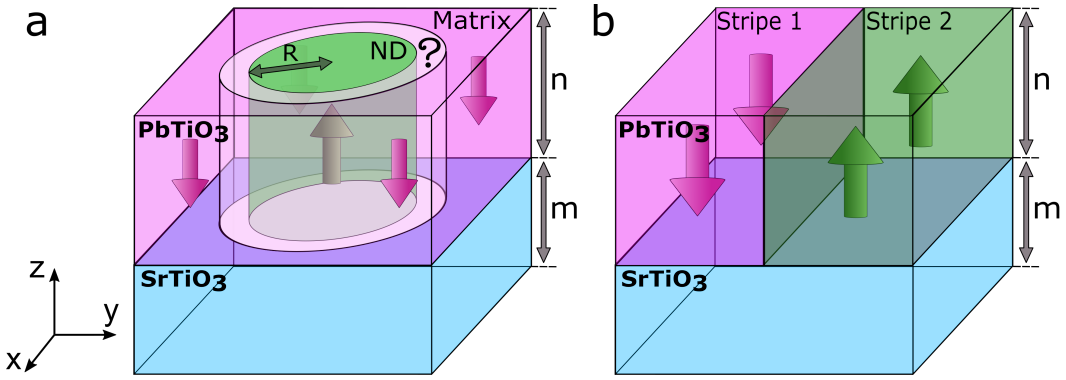

Figure 5.5: Sketch of $(PbTiO_3)_n/(SrTiO_3)_m$ superlattice in which we write the (a) nanodomain(green region) confined in the $PbTiO_3$ layer with positive polarization within a matrix (magenta region) of opposite polarization and the (b) 180° stripe domains. The $SrTiO_3$ layer is the blue region.

focus especially on the topological properties of the bubble arrangement and the polarization behavior in the domain walls and in the interface that proved to be the most challenging regions to study at an experimental level.

5.3.1 Stripes domains Vs bubble domains

As we described in the previous section, on $PbTiO_3/SrTiO_3$ superlattices grown on a substrate of $SrTiO_3$, ferroelectric bubbles can be stabilized inside the $PbTiO_3$ layers, with a positive polarization along z surrounded by a matrix with opposite polarization [7], represented in a simplified version in the Fig. 5.5 (a). On the other side, in these superlattices other polarization arrangements can be obtained, such as 180° stripe domains as shown in Fig. 5.5 (b). Yadav et al. [3] reported the experimental observation of 180° stripe domains in $PbTiO_3/SrTiO_3$ superlattices grown on a substrate of $DyScO_3$. The polar vortices were formed around the domain walls, as shown in Fig. 5.6 with the polarization maps reproducing the results presented in the literature [3, 8].

So the question that arises is, which of these configurations are more stable when we vary the epitaxial constraints. In order to investigate the two different configurations we used the second-principles methods to perform the annealing and relaxation of the initial configurations presented in Fig. 5.5 (a) and (b), changing the epitaxial constraints in the plane

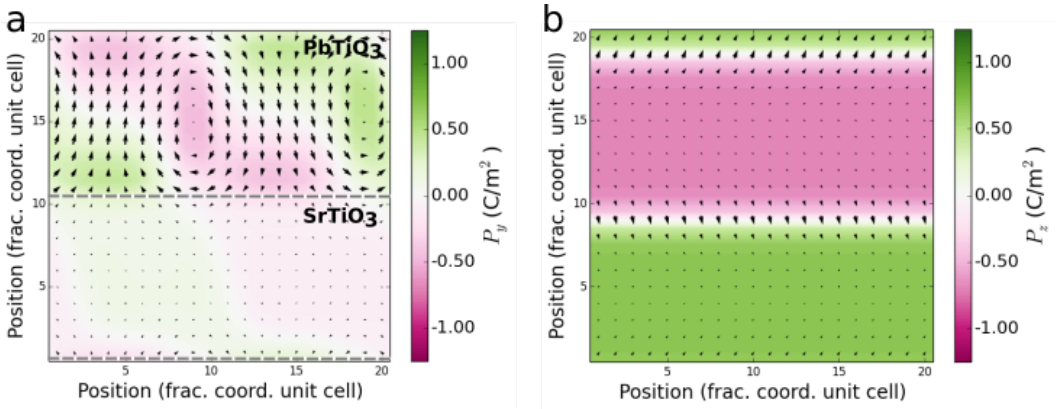

Figure 5.6: Calculated polarization maps in which we observe the vortex-antivortex pairs in the ($PbTiO_3$)/($SrTiO_3$) superlattices. Panel (a) show the plane normal to the superlattice layers (zy plane) in order to identify the vortex-antivortex configuration. Panel (b) is the plane in the middle of the $PbTiO_3$ layer parallel to the superlattice layers. The color scale gives the out-of-plane component, while the arrows correspond to the in-plane. The figure reproduce the results published by Yadav et al. [3] and Shafer et al. [8].

xy. In Fig. 5.7 we present the energy difference between these configurations computed for $PbTiO_3$/$SrTiO_3$ superlattice with a thickness of 10 unit cells of $PbTiO_3$ and 4 unit cells of $SrTiO_3$ as a function of the epitaxial constraints. This energy difference ΔE is defined as

$$\Delta E = \frac{E_{Bub} - E_{Str}}{\#PbTiO_3 f.u} \tag{5.8}$$

where E_{Bub} and E_{Str} are the energies of the bubbles and stripes configurations and $\#$ $PbTiO_3$ f.u is the number of the formula units of $PbTiO_3$ in the superlattice.

This choice for the thickness of the layers allows us to realistically capture the behavior of the $PbTiO_3$/$SrTiO_3$ superlattices, using the same thickness for the $PbTiO_3$ layer that was used experimentally and the minimum thickness of $SrTiO_3$ to break the system into up and down domains. Regarding the in-plane dimensions of the supercells used, in the case of the ferroelectric bubbles the experimental results obtained using three-dimensional reciprocal space mapping showed satellite peaks revealing an in-plane periodicity of about 8 nm (≈ 20 unit cells). Thus, we use a supercell with 20×20 unit cells in-plane, consistent with the experimental results. On the other hand, in the case of the 180° stripe domains configuration

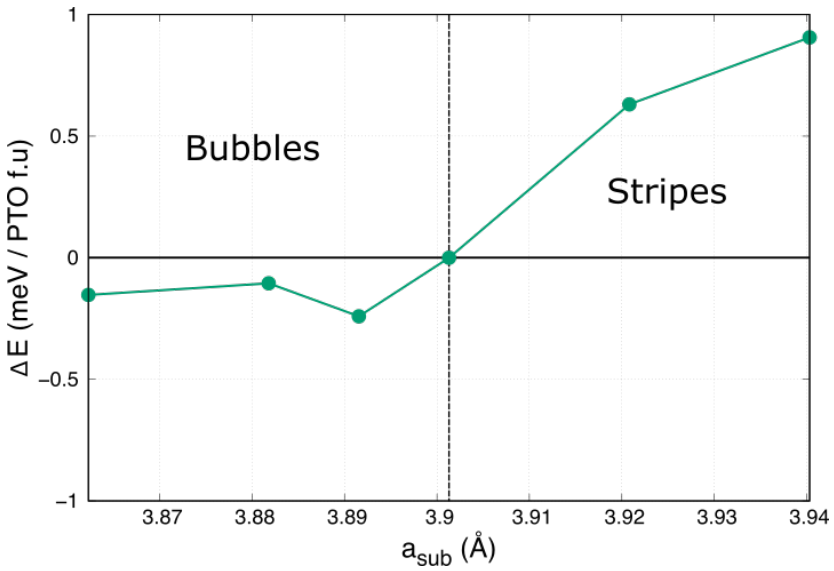

Figure 5.7: The energy difference between the ferroelectric bubble configuration and the 180° stripe domains as a function of the substrate lattice parameter, a_{sub}. This results were obtained using a superlattice of $(PbTiO_3)_{10}/(SrTiO_3)_{10}$. The energy difference is computed using the Eq. 5.8.

the experimental results revealed a modulation of 20 unit cells along x and infinity along y [3]. Then we used a supercell of 20×1 unit cells in-plane.

These results show two different regions. In the first region for $a_{sub} < 3.901$ Å the electric skyrmion bubble is the most stable configuration. For the second region when $a_{sub} > 3.901$ Å the 180° stripes configuration reduces its energy and becomes the most stable configuration. The crossing point of the energies for the two configurations that we take into account occurs for an $a_{sub} = 3.901$ Å, which corresponds to the value used for the calculations in which we consider a substrate of $SrTiO_3$. The results show that the energy difference between the two configurations is very small, regardless of the epitaxial restrictions considered in this section. However, despite the small difference in energy, we identified a clear trend (expansive tension favors stripes and compressive favors bubbles) and both metastable minima are robust – or in other words, it is not easy to go from one state to the other).

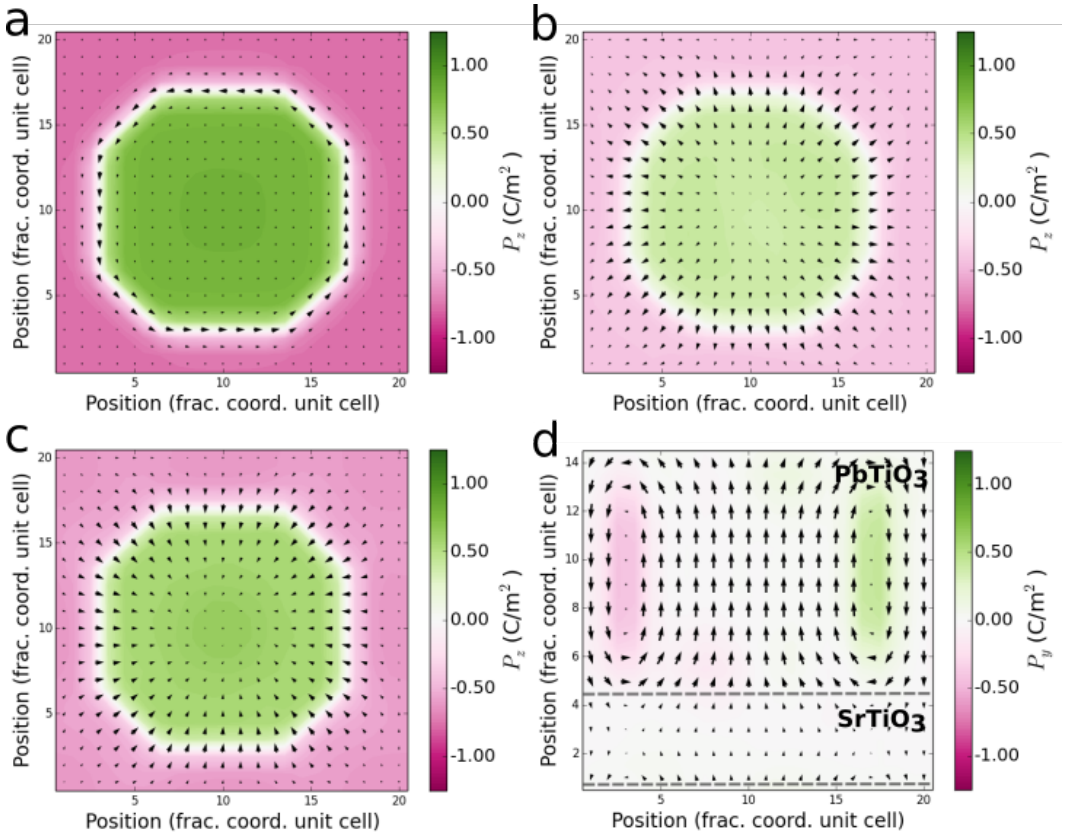

Figure 5.8: Calculated polarization maps of the nanodomain in $PbTiO_3/SrTiO_3$ superlattices where the color scale gives the out-of-plane component, while the arrows correspond to the in-plane; Panels [(a)–(c)] are the xy planes along the superlattice. The panel (a) is a plane in the middle of the $PbTiO_3$ layer and the panels (b) and (c) are respectively the planes at the top and bottom interface between the $PbTiO_3$ and the $SrTiO_3$ layers. In the panel (d) shows the polarization of the xz plane that passes in the middle of the nanodomain.

5.3.2 Structure and stability of ferroelectric bubbles

In order to investigate the polarization arrangement of the ferroelectric bubble in the $PbTiO_3/SrTiO_3$ superlattice grown on a substrate of $SrTiO_3$ we used the same strategy (as before in Chapter 3), starting with an initial configuration presented in Fig. 5.5 (a). The results obtained are presented in the Fig. 5.8 where we show the polarization maps in the different planes of the ferroelectric bubble configuration. The polarization map of the middle layer of $PbTiO_3$ is presented in panel (a) where we observe the two different domains, the bubble with positive polarization surrounded by the matrix with opposite polarization. Between these two do-

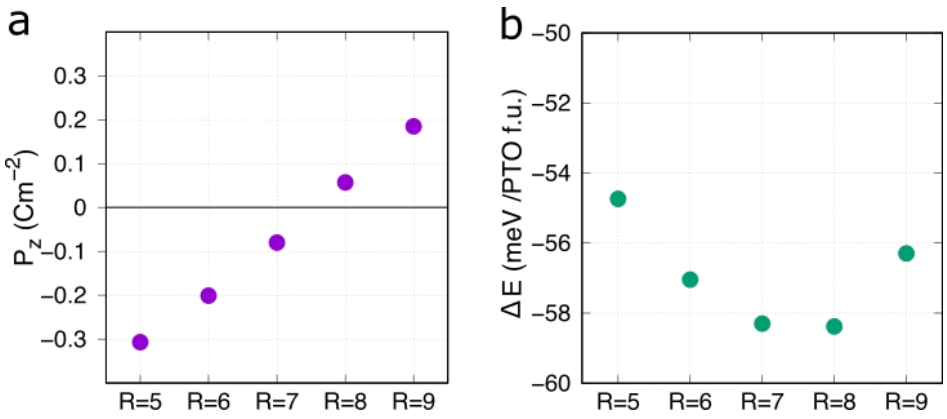

Figure 5.9: Average polarization along z (a) and energy difference (b) for nanodomain with a different radius (presented in unit cells); The energy difference is given by $\Delta E = (E - E_{Ref})/(\#PbTiO_3 f.u)$ where the E is the energy of the relaxed nanodomain configuration and E_{Ref} is the energy of the reference structure of the superlattice. The reference structure is the ideal perovskite structure of $PbTiO_3$ and $SrTiO_3$. We imposed an epitaxial constraint corresponding to having a SrTiO3 (001)-oriented square substrate; we assume in-plane lattice constants $a = b = 3.901$ Å.

mains the nanodomain wall presents a closed loop of polarization in-plane with a Bloch-like character. This result obtained is similar to the result obtained for the nanodomain in pure $PbTiO_3$ presented in Chapter 3. At the top and bottom interfaces between the layers, the polarization maps shown in Fig. 5.8(b) and (c) reveal a different arrangement of the in-plane polarization. At the top interface the polarization in-plane is normal to the domain wall plane and points to the center of the nanodomain. At the bottom interface the same behavior is observed, however, in this case the polarization in-plane points outwards of the nanodomain. Then in both interfaces we have Néel-like domain wall (described in Chapter 1) with polarization pointing normal to the domain wall plane. The cross-sectional view presented in Fig. 5.8 (d) (xz plane) shows the two vortices of polarization around the domain walls in the $PbTiO_3$ layer. The arrangement of polarization that we obtained is in agreement with the experimental results discussed in the Section 5.2.

Varying the radius of the ferroelectric bubble we change the volume of $PbTiO_3$ with polarization up (nanodomain) and down (matrix). As a consequence, we change the average polarization and energy of our configuration. In Fig. 5.9(a) shows the average polarization

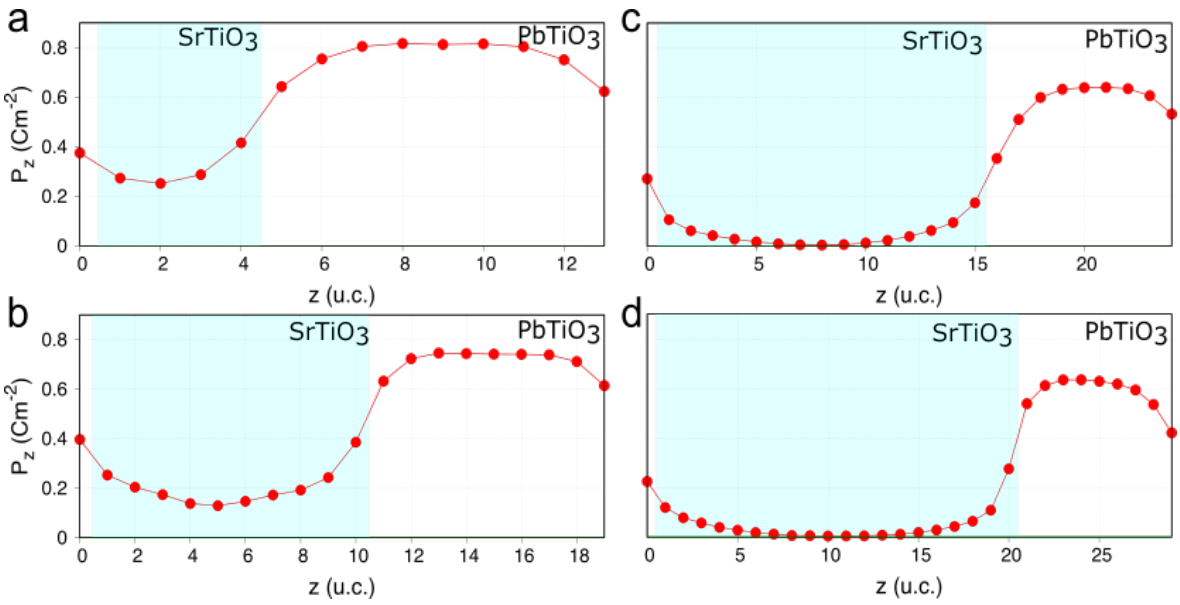

Figure 5.10: Polarization profile along the direction normal to the layers computed in the center of the nanodomain for different superlattices $(PbTiO_3)_n/(SrTiO_3)_m$ varying the $SrTiO_3$ layer thickness $m = 4, 10, 15$ and 20 unit cells; The blue region corresponds to the $SrTiO_3$ layer; The P_z was computed from the atomic displacements in a unit cell centered in the A cation (Sr and Pb atoms).

along z inside the $PbTiO_3$ layer as a function of the bubble radius. For a $R = 7$ and 8 unit cells the volume of $PbTiO_3$ polarized up and down are similar, minimizing the global polarization along z. As a consequence, in Fig. 5.9(b) we verify that for these radius of the nanodomain ($R = 7$ and 8 unit cells) we obtained the ferroelectric bubbles with lower energy.

Finally, we study the effect of the $SrTiO_3$ layer thickness that we define as m (as well as defined in Fig. 5.5 (a)) and how it affects the ferroelectric bubble polarization along the $PbTiO_3$ and $SrTiO_3$ layers and at the interface between them. Fig. 5.10 shows the results of P_z obtained in the center of the ferroelectric bubble for different superlattices in which the thickness of the $PbTiO_3$ layers is kept fixed (with 10 unit cells) and the thickness of the $SrTiO_3$ layers $m = 4, 10, 15$ and 20 unit cells. The main difference in the results obtained for different superlattices is observed in the $SrTiO_3$ layers. Fig. 5.10(a) and (b) shows a $SrTiO_3$ layer clearly polarized, even in the central planes. On the other hand, for superlattices with $SrTiO_3$ thickness of 15 to 20 unit cells Fig. 5.10(c) and (d) show an unpolarized region in

the center of the $SrTiO_3$ layers. In the $PbTiO_3$ layers we observe that the magnitude of the polarization decrease when thickness of $SrTiO_3$ layer is increased. These results seem to indicate that by increasing the thickness of the $SrTiO_3$ layers, we build superlattices in which the ferroelectric bubbles will be electrostatically decoupled along the z direction.

5.4 Topological properties of ferroelectric bubbles

The Pontryagin density associated to the different arrangements of the polarization obtained along the $PbTiO_3$ layers was computed following the strategy presented in the Appendix D. However, in this case the polarization arrangement is not periodic along z, as we verified when we analyzed the structure of the ferroelectric bubble, with different arrangements in the interfaces and in the planes in the middle of the $PbTiO_3$ layers. Therefore, to study the topological properties of ferroelectric bubbles we break it down into a collection of xy planes and for each we compute the Pontryagin density. Fig. 5.11 shows the peaks of the Pontryagin density along the domain walls in the three different regions of the superlattice (in the middle of the $PbTiO_3$ layer and the top and bottom interfaces but the materials). Computing the total topological charge from these distributions we obtained a $Q = +1$ for all the planes in the $PbTiO_3$ layer.

Then, in the middle $PbTiO_3$ layer (Fig. 5.8 (a)) we have a Bloch-like domain wall similar to the results presented in Chapter 3, whereas in the polarization texture at the top and bottom interfaces between $PbTiO_3$ and $SrTiO_3$ (Fig. 5.8 (b) and (c)) we have Néel-like domain wall (as shown in Chapter 1).

This way, the polarization texture in the $PbTiO_3$ layer can be seen as an evolution of two-dimensional skyrmions with different characters along z. Such complex arrangement of the polarization are formed by different skyrmions arises from the presence of $SrTiO_3$ layers and as a consequence the polarization at the interfaces rotates in the xy plane.

Then the ferroelectric bubbles in the $PbTiO_3$/$SrTiO_3$ superlattices grown on a substrate of $SrTiO_3$ are formed by a column of electric skyrmion – confined inside the $PbTiO_3$ layers – with different characters. These results obtained from second-principles calculations are in

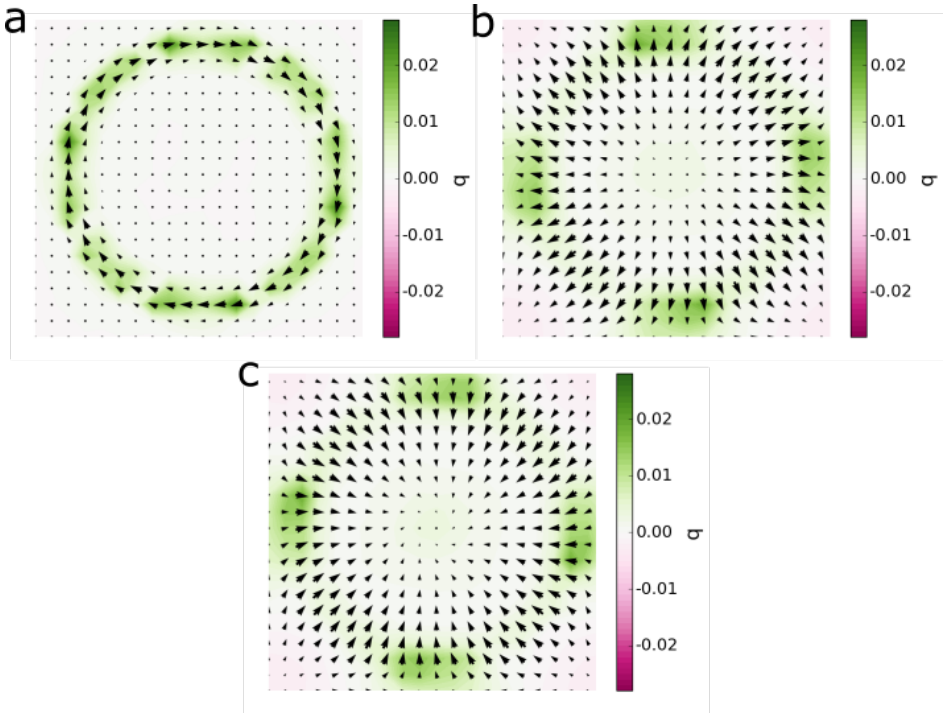

Figure 5.11: Calculated Pontryagin density of the different regions $PbTiO_3$ layer; The panel (a) is a plane in the middle of the $PbTiO_3$ layer and the panels (b) and (c) are respectively the planes at the top and bottom interface between the $PbTiO_3$ and the $SrTiO_3$ layers.

agreement with the experimental results.

5.5 Summary

The investigation of ferroelectric bubbles in $PbTiO_3/SrTiO_3$ superlattices led us to conclude that electric skyrmions could be stabilized in realistic materials. These ferroelectric bubbles confined in the $PbTiO_3$ layers are formed by a column of electric skyrmions with different characters. Bloch skyrmions in the central layers and Néel Skyrmions in the interfaces between $PbTiO_3$ and $SrTiO_3$. These results were demonstrated experimentally with the observation of electric skyrmions at room temperature.

Chapter 6

Summary and conclusions

The study of ferroelectric materials in the last decades has led to the observation of various exotic polarization behaviors in complex multidomain structures in which polarization vortices have been observed. These discoveries raised the possibility of stabilizing topological structures such as skyrmions in simple ferroelectric materials, analogous to the widely studied magnetic skyrmions.

In this context, in the thesis I present, a strategy for stabilizing electric skyrmions in a single-phase ferroelectric material was predicted for the first time, taking advantage of the Bloch character of polarization in the domain walls. Applying external electric fields or simulating the effect of different substrates, it has been shown that electric skyrmions can be controlled or even destroyed. The studies of the electric skyrmions in conditions closer to the realistic ones allowed to demonstrate that these topological arrangements are stable at finite temperatures and that they can be observed experimentally in $PbTiO_3$/ $SrTiO_3$ superlattices at room temperature.

We present a basic characterization of electric skyrmions in ferroelectric materials, however, some questions remain open for a deeper understanding of the behavior and properties of these topological objects, such as:

- As we discussed earlier in superlattices, similar to those that were studied in this work, the polarization inside the $PbTiO_3$ layer has an anomalous dielectric response (effec-

tively mimicking a ”negative capacitance” [5, 96, 97]) . Thus, with regard this negative capacitance, the electrical skyrmions observed in the $PbTiO_3$/$SrTiO_3$ superlattices were studied and it was demonstrated that these also have local negative capacitance especially in the domain walls and at the interfaces between $PbTiO_3$ and $SrTiO_3$. This work, to which I have contribute second-principles simulations and analysis, is currently under review in Nature Materials [98].

- Another question that I would like to raise is related to the interaction of electric skyrmions with polarized light due to their chirality. Resonant soft-X-ray diffraction experiments show circular dichroism, confirming chirality [7]. However, a strategy to control the chirality of the electric skyrmions by changing the direction of rotation of the polarization in the NDW remains unclear.

- In the first part of this study, it was always considered a nanodomain periodically repeated and thus the different interactions between nanodomains with the same or different topologies (such as skyrmions and anti-skyrmions) or the formation of different lattices of these objects were not evaluated.

- Under certain conditions the domain walls can move almost freely as predicted in $PbTiO_3$/$SrTiO_3$ superlattices [5] .The free movement of the domain walls, the possibility of moving the electric skyrmions and controlling their dynamics by moving the nanodomain in a controlled manner without destroying the skyrmion remains an open question.

In this work, we start by looking for the electric analog to a magnetic skyrmion. When comparing them, we find that electric skyrmions can be smaller than magnetic ones, and electric skyrmions can be controlled or manipulated using electric fields instead of magnetic fields. For future applications this is a fundamental point since electric fields are cheaper and do not involve the application of electric currents that can be a problem in nanoscale devices. However, since electric skyrmions have only just been discovered, the investigation of magnetic skyrmions is much more advanced and already in a phase of application in

devices [69, 99]. This was achieved with the very intense study not only of how to create magnetic skyrmions but also with the investigation of how to destroy, detect or move them. This led to the development of Skyrmion-Based Racetrack Memory and Skyrmion-Based Logic Gates in which skyrmions are moved along a nanowire and the presence of a skyrmion or its absence is associated with values 1 or 0 [99]. Inspired by the evolution we saw in magnetic skyrmions the study of electric skyrmions must follow a similar evolution attempting (as we mentioned earlier) to find practical strategies to move and quickly detach electric skyrmions so that they can be considered as a strong possibility in memory devices or nanoscale devices taking into account their small size.

Chapter 7

List of publications

The list of publications produced during this Thesis:

- M. A. P. Gonçalves, C. Escorihuela-Sayalero, P. García-Fernández, J. Junquera and J. Íñiguez.
  Theoretical guidelines to create and tune electric skyrmion bubbles
  Science Advances, **5**, no. 2 (2019)

- S. Das, Y. L. Tang, Z. Hong, M. A. P. Gonçalves, M. R. McCarter, C. Klewe, K. X. Nguyen, F. Gómez-Ortiz, P. Shafer, E. Arenholz, V. A. Stoica, S. -L. Hsu, B. Wang, C. Ophus, J. F. Liu, C. T. Nelson, S. Saremi, B. Prasad, A. B. Mei, D. G. Schlom, J. Íñiguez, P. García-Fernández, D. A. Muller, L. Q. Chen, J. Junquera, L. W. Martin and R. Ramesh.
  Observation of room-temperature polar skyrmions
  Nature, **568**, 368–372 (2019)

- S. Das, Z. Hong, V. A. Stoica, M. A. P. Gonçalves, E. Parsonnet, S. Saremi, M. R. McCarter, A. Reynoso, D. Meyers, V. Ravi, H. Zhou, Z. Zhang, H. Wen, F. Gómez-Ortiz, P. García-Fernández, J. Bokor, J. Íñiguez, J. Freeland, J. Junquera, L. W. Martin and R. Ramesh.
  Local negative permittivity and topological-phase transition in polar skyrmions
  Submitted to Nature Materials

- M. A. P. Gonçalves, P. García-Fernández, J. Junquera and J. Íñiguez.
  Electric skyrmion phase diagram
  In preparation

Bibliography

[1] Wojdeł, J. C. & Íñiguez, J. Ferroelectric transitions at ferroelectric domain walls found from first principles. *Physical Review Letters* **112**, 247603 (2014).

[2] Nahas, Y. & et al. Discovery of stable skyrmionic state in ferroelectric nanocomposites. *Nature Communications* **6**, 8542 (2015).

[3] Yadav, A. K. e. a. Observation of polar vortices in oxide superlattices. *Nature* **530**, 198–201 (2016).

[4] Aguado-Puente, P. & Junquera, J. Structural and energetic properties of domains in $PbTiO_3$/$SrTiO_3$ superlattices from first principles. *Physical Review B* **85**, 184105 (2012).

[5] Zubko, P. *et al.* Negative capacitance in multidomain ferroelectric superlattices. *Nature* **534**, 524–528 (2016).

[6] Wojdeł, J. C., Hermet, P., Ljungberg, M. P., Ghosez, P. & Íñiguez, J. First-principles model potentials for lattice-dynamical studies: general methodology and example of application to ferroic perovskite oxides. *Journal of Physics: Condensed Matter* **25**, 305401 (2013).

[7] Das, S. *et al.* Observation of room-temperature polar skyrmions. *Nature* **568**, 368–372 (2019).

[8] Shafer, P. *et al.* Emergent chirality in the electric polarization texture of titanate superlattices. *Proceedings of the National Academy of Sciences* **115**, 915–920 (2018).

[9] Hao, X. A review on the dielectric materials for high energy-storage application. *Journal of Advanced Dielectrics* **03**, 1330001 (2013).

[10] Rödel, J. *et al.* Perspective on the development of lead-free piezoceramics. *Journal of the American Ceramic Society* **92**, 1153–1177 (2009).

[11] Muralt, P. Ferroelectric thin films for micro-sensors and actuators: a review. *Journal of Micromechanics and Microengineering* **10**, 136–146 (2000).

[12] Scott, J. F. & Paz de Araujo, C. A. Ferroelectric memories. *Science* **246**, 1400–1405 (1989).

[13] Eerenstein, W., Mathur, N. D. & Scott, J. F. Multiferroic and magnetoelectric materials. *Nature* **442**, 759–765 (2006).

[14] Scott, J. F. *Ferroelectric Memories* (Springer, Berlin, 2000).

[15] Lines, M. E. & Glass, A. M. *Principles and Applications of Ferroelectrics and Related Materials*. Oxford Classic Texts in the Physical Sciences (Clarendon Press, Oxford, 1977).

[16] Rabe, K. M., Ahn, C. H. & Triscone, J. (eds.) *Physics of Ferroelectrics: A Modern Perspective* (Springer Berlin Heidelberg, Berlin, Heidelberg, 2007).

[17] Kwei, G. H., Lawson, A. C., Billinge, S. J. L. & Cheong, S. W. Structures of the ferroelectric phases of barium titanate. *J. Phys. Chem.* **97**, 2368–2377 (1993).

[18] Zhong, W., Vanderbilt, D. & Rabe, K. M. Phase transitions in $BaTiO_3$ from first principles. *Physical Review Letters* **73**, 1861 (1994).

[19] Mitsui, T. *et al. Oxides, Landolt–Börnstein: Numerical Data and Functional Relationships in Science and Technology*, vol. vol. 16 (Springer, Berlin, 1981).

[20] Mitsui, T. *et al. Oxides, Landolt–Börnstein: Numerical Data and Functional Relationships in Science and Technology*, vol. vol. 28 (Springer, Berlin, 1981).

[21] Kuroiwa, Y. *et al.* Evidence for pb-o covalency in tetragonal $\mathrm{pbtio_3}$. *Phys. Rev. Lett.* **87**, 217601 (2001).

[22] García, A. & Vanderbilt, D. First-principles study of stability and vibrational properties of tetragonal $PbTiO_3$. *Physical Review B* **54**, 3817 (1996).

[23] Müller, K. A. & Burkard, H. $\mathrm{Srtio_3}$: An intrinsic quantum paraelectric below 4 k. *Phys. Rev. B* **19**, 3593–3602 (1979).

[24] Fleury, P. A., Scott, J. F. & Worlock, J. M. Soft phonon modes and the 110° K phase transition in $SrTiO_3$. *Physical Review Letters* **21**, 16–19 (1968).

[25] Catalan, G., Seidel, J., Ramesh, R. & Scott, J. F. Domain wall nanoelectronics. *Reviews of Modern Physics* **84**, 119–156 (2012).

[26] Tagantsev, A., Cross, L. E. & Fousek, J. *Domains in Ferroic Crystals and Thin Films* (Springer, 2010).

[27] Salje, E. K. Multiferroic domain boundaries as active memory devices: Trajectories towards domain boundary engineering. *ChemPhysChem* **11**, 940–950 (2010).

[28] Rabe, K. M. & Ghosez, P. First-principles studies of ferroelectric oxides. In *Physics of Ferroelectric: A modern perspective*, vol. 105 of *Topics in Applied Physics*, 117–174 (Springer-Verlag Berlin, 2007).

[29] Ahluwalia, R. *et al.* Manipulating ferroelectric domains in nanostructures under electron beams. *Phys. Rev. Lett.* **111**, 165702 (2013).

[30] McGilly, L. J., Yudin, P., Feigl, L., Tagantsev, A. K. & Setter, N. Controlling domain wall motion in ferroelectric thin films. *Nature Nanotechnology* **10**, 145–150 (2015).

[31] Whyte, J. R. *et al.* Ferroelectric domain wall injection. *Advanced Materials* **26**, 293–298 (2014).

[32] Aird, A. & Salje, E. K. H. Sheet superconductivity in twin walls: experimental evidence of WO_{3-x}. *Journal of Physics: Condensed Matter* **10**, L377 (1998).

[33] Seidel, J. *et al.* Conduction at domain walls in oxide multiferroics. *Nature Materials* **8**, 229–234 (2009).

[34] Farokhipoor, S. & Noheda, B. Conduction through 71° domain walls in $BiFeO_3$ thin films. *Physical Review Letters* **107**, 127601 (2011).

[35] Tagantsev, A. K., Courtens, E. & Arzel, L. Prediction of a low-temperature ferroelectric instability in antiphase domain boundaries of strontium titanate. *Physical Review B* **64**, 224107 (2001).

[36] Scott, J. F., Salje, E. K. H. & Carpenter, M. A. Domain Wall Damping and Elastic Softening in $SrTiO_3$: Evidence for Polar Twin Walls. *Physical Review Letters* **109**, 187601 (2012).

[37] Salje, E. K. H., Aktas, O., Carpenter, M. A., Laguta, V. V. & Scott, J. F. Domains within domains and walls within walls: Evidence for polar domains in cryogenic $SrTiO_3$. *Physical Review Letters* **111**, 247603 (2013).

[38] Schiaffino, A. & Stengel, M. Macroscopic polarization from antiferrodistortive cycloids in ferroelastic $\mathrm{srtio_3}$. *Phys. Rev. Lett.* **119**, 137601 (2017).

[39] Pöykkö, S. & Chadi, D. J. *Ab initio* study of 180° domain wall energy and structure in $PbTiO_3$. *Applied Physics Letters* **75**, 2830–2832 (1999).

[40] Meyer, B. & Vanderbilt, D. Ab initio study of ferroelectric domain walls in $PbTiO_3$. *Physical Review B* **65**, 104111 (2002).

[41] Wu, Z. & Cohen, R. E. Pressure-induced anomalous phase transitions and colossal enhancement of piezoelectricity in $\mathrm{pbtio_3}$. *Phys. Rev. Lett.* **95**, 037601 (2005).

[42] Kornev, I. A. *et al.* Ferroelectricity of perovskites under pressure. *Phys. Rev. Lett.* **95**, 196804 (2005).

[43] Kornev, I. A. & Bellaiche, L. The nature of ferroelectricity under pressure. *Phase Transitions* **80**, 385–413 (2007).

[44] Íñiguez, J. & Vanderbilt, D. First-principles study of the temperature-pressure phase diagram of $BaTiO_3$. *Physical Review Letters* **89**, 115503 (2002).

[45] Tinte, S., Íñiguez, J., Rabe, K. M. & Vanderbilt, D. Quantitative analysis of the first-principles effective hamiltonian approach to ferroelectric perovskites. *Physical Review B* **67**, 064106 (2003).

[46] Rabe, K. M. Theoretical investigations of epitaxial strain effects in ferroelectric oxide thin films and superlattices. *Current Opinion in Solid State and Materials Science* **9**, 122 – 127 (2005).

[47] Schlom, D. G. *et al.* Strain tuning of ferroelectric thin films. *Annual Review of Materials Research* **37**, 589–626 (2007).

[48] Haeni, J. H. *et al.* Room-temperature ferroelectricity in strained srtio$_3$. *Nature* **430**, 758–761 (2004).

[49] Pertsev, N. A., Zembilgotov, A. G. & Tagantsev, A. K. Effect of mechanical boundary conditions on phase diagrams of epitaxial ferroelectric thin films. *Phys. Rev. Lett.* **80**, 1988–1991 (1998).

[50] Dawber, M., Rabe, K. M. & Scott, J. F. Physics of thin-film ferroelectric oxides. *Rev. Mod. Phys.* **77**, 1083–1130 (2005).

[51] Choi, K. J. *et al.* Enhancement of ferroelectricity in strained batio3 thin films. *Science* **306**, 1005–1009 (2004).

[52] Norton, D. P. *et al.* Superconductivity in srcuo$_2$/bacuo$_2$ superlattices: Formation of artificially-layered superconducting materials. *Science* **265**, 2074–2077 (1994).

[53] Tsurumi, T. *et al.* Artificial ferroelectricity in perovskite superlattices. *Appl. Phys.Lett.* **85**, 5016–5018 (2004).

[54] Ohtomo, A. & Hwang, H. Y. A high-mobility electron gas at the laalo$_3$/srtio$_3$ heterointerface. *Nature* **427**, 423 (2004).

[55] Zubko, P., Stucki, N., Lichtensteiger, C. & Triscone, J. M. X-Ray Diffraction Studies of 180° Ferroelectric Domains in $PbTiO_3$/$SrTiO_3$ Superlattices under an Applied Electric Field. *Physical Review Letters* **104**, 187601 (2010).

[56] Zubko, P. *et al.* Ferroelectric domains in $\mathrm{pbtio_3}$/$\mathrm{srtio_3}$ superlattices. *Ferroelectrics* **433**, 127–137 (2012).

[57] Zubko, P. *et al.* Electrostatic Coupling and Local Structural Distortions at Interfaces in Ferroelectric/Paraelectric Superlattices. *Nano Letters* **12**, 2846–2851 (2012).

[58] Ishikawa, K., Yoshikawa, K. & Okada, N. Size effect on the ferroelectric phase transition in $\mathrm{pbtio_3}$ ultrafine particles. *Phys. Rev. B* **37**, 5852–5855 (1988).

[59] Jiang, B., Peng, J. L., Bursill, L. A. & Zhong, W. L. Size effects on ferroelectricity of ultrafine particles of pbtio3. *Journal of Applied Physics* **87**, 3462–3467 (2000).

[60] Fu, H. & Bellaiche, L. Ferroelectricity in barium titanate quantum dots and wires. *Phys. Rev. Lett.* **91**, 257601 (2003).

[61] Naumov, I. I., Bellaiche, L. & Fu, H. Unusual phase transitions in ferroelectric nanodisks and nanorods. *Nature* **432**, 737–740 (2004).

[62] Skyrme, T. A unified field theory of mesons and baryons. *Nuclear Physics* **31**, 556 – 569 (1962).

[63] Berger, L. Emission of spin waves by a magnetic multilayer traversed by a current. *Phys. Rev. B* **54**, 9353–9358 (1996).

[64] Parkin, S. S. P., Hayashi, M. & Thomas, L. Magnetic domain-wall racetrack memory. *Science* **320**, 190–194 (2008).

[65] Cheong, S.-W. & Mostovoy, M. Multiferroics: a magnetic twist for ferroelectricity. *Nature Materials* **6**, 13–20 (2007).

[66] Nagaosa, N. & Tokura, Y. Topological properties and dynamics of magnetic skyrmions. *Nature Nanotechnology* **8**, 8579–8589 (2013).

[67] Bogdanov, A. & Hubert, A. Thermodynamically stable magnetic vortex states in magnetic crystals. *Journal of Magnetism and Magnetic Materials* **138**, 255 – 269 (1994).

[68] Rößler, U. K., Bogdanov, A. N. & Pfleiderer, C. Spontaneous skyrmion ground states in magnetic metals. *Nature* **442**, 797 (2006).

[69] Seki, S. & Mochizuki, M. *Skyrmions in Magnetic Materials* (Springer International Publishing, 2016).

[70] Lin, Y. S., Grundy, P. J. & Giess, E. A. Bubble domains in magnetostatically coupled garnet films. *Applied Physics Letters* **23**, 485–487 (1973).

[71] Dawber, M., Gruverman, A. & Scott, J. F. Skyrmion model of nano-domain nucleation in ferroelectrics and ferromagnets. *Journal of Physics: Condensed Matter* **18**, L71 (2006).

[72] Chen, W. J. & et al. Mechanical switching in ferroelectrics by shear stress and its implications on charged domain wall generation and vortex memory devices. *RSC Advances* **8**, 4434–4444 (2018).

[73] Zhang, Q. & et. al. Nanoscale bubble domains and topological transitions in ultrathin ferroelectric films. *Advanded Materials* **29**, 1702375 (2017).

[74] García-Fernández, P., Wojdeł, J. C., Junquera, J. & Íñiguez, J. Second-principles method for materials simulations including electron and lattice degrees of freedom. *Physical Review B* **93**, 195137 (2016).

[75] Hohenberg, P. & Kohn, W. Inhomogeneous electron gas. *Physical Review* **136**, B864 (1964).

[76] Kohn, W. & Sham, L. J. Self-consistent equations including exchange and correlation effects. *Physical Review* **140**, A1133 (1965).

[77] Perdew, J. P. *et al.* Atoms, molecules, solids, and surfaces: Applications of the generalized gradient approximation for exchange and correlation. *Physical Review B* **46**, 6671–6687 (1992).

[78] Zhong, W., Vanderbilt, D. & Rabe, K. M. First-principles theory of ferroelectric phase transitions for perovskites: The case of $BaTiO_3$. *Physical Review B* **52**, 6301 (1995).

[79] Waghmare, U. V. & Rabe, K. M. Ab initio statistical mechanics of the ferroelectric phase transition in $PbTiO_3$. *Physical Review B* **55**, 6161 (1997).

[80] Rahmedov, D., Wang, D., Íñiguez, J. & Bellaiche, L. Magnetic cycloid of $BiFeO_3$ from atomistic simulations **109**, 037207.

[81] Bhattacharjee, S., Rahmedov, D., Bellaiche, L. & Wang, D. Novel magnetic arrangement and structural phase transition induced by spin-lattice coupling in multiferroics. *MRS Communications* **3**, 213–218 (2013).

[82] Gonze, X. & Lee, C. Dynamical matrices, born effective charges, dielectric permittivity tensors, and interatomic force constants from density-functional perturbation theory. *Physical Review B* **55**, 10355 (1997).

[83] Haun, M. J., Furman, E., Jang, S. J., McKinstry, H. A. & Cross, L. E. Thermodynamic theory of PbTiO3. *Journal of Applied Physics* **62**, 3331–3338 (1987).

[84] Diéguez, O., Rabe, K. M. & Vanderbilt, D. First-principles study of epitaxial strain in perovskites. *Phys. Rev. B* **72**, 144101 (2005).

[85] Bungaro, C. & Rabe, K. M. Epitaxially strained $[001] - (\mathrm{pbtio_3})_1(\mathrm{pbzro_3})_1$ superlattice and $\mathrm{pbtio_3}$ from first principles. *Phys. Rev. B* **269**, 184101 (2004).

[86] Neaton, J. B. & Rabe, K. M. Theory of polarization enhancement in epitaxial $batio_3/srtio_3$ superlattices. *Appl. Phys. Lett.* **82**, 1586 (2003).

[87] Shimuta, T. *et al.* Enhancement of remanent polarization in epitaxial $batio_3/srtio_3$ superlattices with asymmetric structure. *J. Appl. Phys.* **91**, 2290 (2004).

[88] Tian, W. *et al.* Structural evidence for enhanced polarization in a commensurate short-period $batio_3/srtio_3$ superlattice. *Appl. Phys. Lett.* **89**, 092905 (2006).

[89] Junquera, J. & Ghosez, P. Critical thickness for ferroelectricity in perovskite ultrathin films. *Nature* **422**, 506 (2003).

[90] Dawber, M. *et al.* Unusual behaviour of the ferroelectric polarization in pbtio$_3$/srtio$_3$ superlattices. *Phys. Rev. Lett.* **95**, 177601 (2005).

[91] Aguado-Puente, P., Garca-Fernández, P. & Junquera, J. Interplay of couplings between antiferrodistortive, ferroelectric, and strain degrees of freedom in monodomain pbtio$_3$/srtio$_3$ superlattices. *Phys. Rev. Lett.* **107**, 217601 (2011).

[92] Kittel, C. Theory of the structure of ferromagnetic domains in films and small particles. *Phys. Rev.* **70**, 965–971 (1946). URL https://link.aps.org/doi/10.1103/PhysRev.70.965.

[93] Schilling, A. *et al.* Scaling of domain periodicity with thickness measured in $\mathrm{BaTio_3}$ single crystal lamellae and comparison with other ferroics. *Phys. Rev. B* **74**, 024115 (2006). URL https://link.aps.org/doi/10.1103/PhysRevB.74.024115.

[94] Catalan, G., Seidel, J., Ramesh, R. & Scott, J. F. Domain wall nanoelectronics. *Rev. Mod. Phys.* **84**, 119–156 (2012). URL https://link.aps.org/doi/10.1103/RevModPhys.84.119.

[95] Damodaran, A. R. *et al.* Phase coexistence and electric-field control of toroidal order in oxide superlattices. *Nature Materials* **16**, 1003 EP – (2017).

[96] Yadav, A. K. *et al.* Spatially resolved steady-state negative capacitance. *Nature* **565**, 468–471 (2019).

[97] Íñiguez, J., Zubko, P., Luk'yanchuk, I. & Cano, A. Ferroelectric negative capacitances. *Nature Reviews Materials* **4**, 243–256 (2019).

[98] Das, S. *et al.* Local negative permittivity and topological-phase transition in polar skyrmions. *Nature Materials* Submitted (2020).

[99] Kang, W., Huang, Y., Zhang, X., Zhou, Y. & Zhao, W. Skyrmion-electronics: An overview and outlook. *Proceedings of the IEEE* **104**, 2040–2061 (2016).

[100] García, A. & Vanderbilt, D. Electromechanical behavior of batio3 from first principles. *Applied Physics Letters* **72**, 2981–2983 (1998).

[101] García, A. & Vanderbilt, D. Temperature-dependent dielectric response of batio3 from first principles. *AIP Conference Proceedings* **436**, 53–60 (1998).

[102] Rabe, K. M. & Cockayne, E. Temperature-dependent dielectric and piezoelectric response of ferroelectrics from first principles. *AIP Conference Proceedings* **436**, 61–70 (1998).

[103] Ponomareva, I., Bellaiche, L. & Resta, R. Relation between dielectric responses and polarization fluctuations in ferroelectric nanostructures. *Phys. Rev. B* **76**, 235403 (2007).

[104] Neumann, M. Dipole moment fluctuation formulas in computer simulations of polar systems. *Molecular Physics* **50**, 841–858 (1983).

[105] Berg, B. & Lüscher, M. Definition and statistical distributions of a topological number in the lattice o(3) σ-model. *Nuclear Physics B* **190**, 412 – 424 (1981).

[106] Heo, C., Kiselev, N. S., Nandy, A. K., Blügel, S. & Rasing, T. Switching of chiral magnetic skyrmions by picosecond magnetic field pulses via transient topological states. *Scientific Reports* **6**, 27146 (2016).

[107] Papanicolaou, N. & Tomaras, T. Dynamics of magnetic vortices. *Nuclear Physics B* **360**, 425 – 462 (1991).

[108] Pereira Gonçalves, M. A., Escorihuela-Sayalero, C., Garca-Fernández, P., Junquera, J. & Íñiguez, J. Theoretical guidelines to create and tune electric skyrmion bubbles. *Science Advances* **5** (2019).

**

Appendix A

Local polarization

One of the main properties computed from the second-principles simulations is the local polarization. As we shown in Chapter 2 from the second-principles calculation we the homogeneous strain $\boldsymbol{\eta}$ and all the atomic displacements $\{\mathbf{u}_i\}$. Let us start by computing the atomic local electric dipoles within a linear approximation, as

$$d_{i\alpha} = \sum_{\beta} Z^*_{i\beta\alpha} u_{i\beta} \ , \tag{A.1}$$

where $Z^*_{i\beta\alpha}$ is the Born effective-charge tensor of atom i; here, i runs over all atoms in the material (i.e., it runs over both cells and atoms within each cell), and $\alpha, \beta = x, y, z$ label the spatial directions.

Let us note that, for example in $PbTiO_3$, the off-centering of the Pb cations constitutes the greatest contribution to the spontaneous polarization. Hence, we introduce A-centered local modes $\mathbf{v}_l$ at every cell l, defined as a weighted sum of the dipoles $\mathbf{d}_i$ associated to the A atom at cell l and its nearest neighbors (8 B's and 12 O's; see Fig. A.1). Then, we define the A-centered local polarization $\mathbf{P}_l$ as

$$\mathbf{P}_l = \frac{\mathbf{v}_l}{\Omega} \ , \tag{A.2}$$

where Ω is the approximate unit cell volume computed as $\Omega = V/N$, V being the volume of

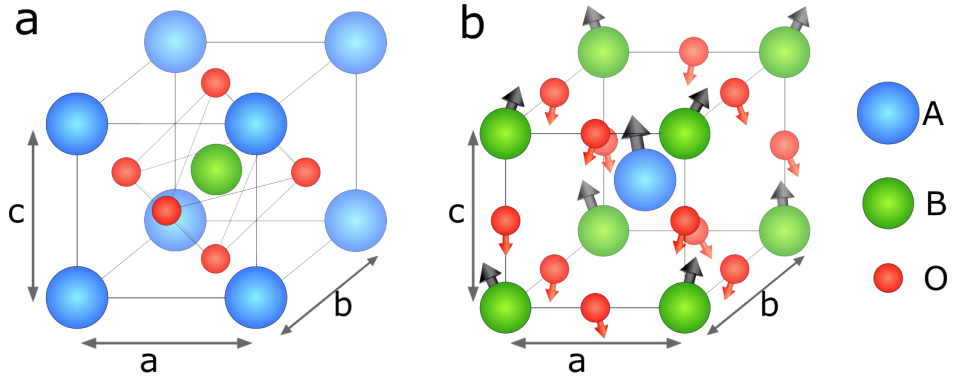

Figure A.1: Sketches of (a) a typical representation of the ideal ABO_3 perovskite structure with the A atoms in the corners of the unit cell and the B atom in the center surrounded by an O's octahedra; (b) is the A-centered unit cell with the nearest neighbors (8 B's and 12 O's). The arrows represent the atomic local dipoles obtained from Eq. A.1.

the simulation supercell (computed taking into account the homogeneous strain) and N is the number of elemental 5-atom unit cells in our supercell. The A-centered local polarization can be presented in a grid when $l \leftrightarrow (x, y, z)$ where the (x, y, z) point coincides with the position of the A atom in the l cell.

Appendix B

Macroscopic dielectric response

The dielectric response describes the linear change of the macroscopic polarization $\mathbf{P}$ due to an external electric field $\boldsymbol{\mathcal{E}}^{\mathrm{ext}}$. So, the elements of the dielectric response tensor are defined by

$$\chi_{\alpha\beta} = \frac{1}{\epsilon_0} \frac{\partial \langle P_\alpha \rangle}{\partial \mathcal{E}_\beta^{\mathrm{ext}}} \,, \tag{B.1}$$

where ϵ_0 is the vacuum permittivity, and α and β label the spatial components of polarization and electric field.

In our Monte Carlo simulations described below, the linear dielectric susceptibility can be obtained from polarization fluctuations of the material at equilibrium, with no electric field applied [100, 101, 102, 103, 104]. The thermal average of $\langle P_\alpha \rangle$ at a temperature T is given by:

$$\langle P_\alpha \rangle = \frac{\sum_s P_\alpha^s e^{-\beta E^s}}{\sum_s e^{-\beta E^s}} \,, \tag{B.2}$$

where $\beta = \frac{1}{k_{\mathrm{B}} T}$ with k_{B} being Boltzmann's constant. E^s and P_α^s are, respectively, the energy and the polarization of a specific configuration s and the sum runs over all possible configurations of the material.

Taking the first derivative of $\langle P_\alpha \rangle$ with respect to the external electric field, we obtain

$$\frac{\partial \langle P_\alpha \rangle}{\partial \mathcal{E}_\beta^{\mathrm{ext}}} = -\beta \left[\left\langle P_\alpha \frac{\partial E}{\partial \mathcal{E}_\beta^{\mathrm{ext}}} \right\rangle - \langle P_\alpha \rangle \left\langle \frac{\partial E}{\partial \mathcal{E}_\beta^{\mathrm{ext}}} \right\rangle \right] . \tag{B.3}$$

The electric field dependence of the energy in our models is given in Chapter 2. Then, the derivative of the energy with respect to the external electric fields is given by

$$\frac{\partial E}{\partial \mathcal{E}_\beta^{\mathrm{ext}}} = -V \frac{\partial(\mathbf{P} \cdot \boldsymbol{\mathcal{E}}^{\mathrm{ext}})}{\partial \mathcal{E}_\beta^{\mathrm{ext}}} = -V P_\beta \ . \tag{B.4}$$

where V is the volume of the simulation supercell. This way, using the Eq. B.3 and Eq. B.4 we can write

$$\chi_{\alpha\beta} = \frac{V\beta}{\epsilon_0}[\langle P_\alpha P_\beta \rangle - \langle P_\alpha \rangle \langle P_\beta \rangle] \ . \tag{B.5}$$

Thus, we obtain that the dielectric response components $\chi_{\alpha\beta}$ are proportional to mean-square averages of the polarization fluctuations.

Appendix C

Local dielectric response

In order to understand the local response of the different regions in the multidomain configuration (domains and NDW), we compute the local dielectric response. In analogy with the definition of the macroscopic dielectric susceptibility Eq. (B.1), we define the local response $\chi_{\alpha\beta}(l)$ as

$$\chi_{\alpha\beta}(l) = \frac{1}{\epsilon_0}\frac{\partial\langle P_\alpha(l)\rangle}{\partial\mathcal{E}^{\text{ext}}_\beta}\ , \tag{C.1}$$

where $\mathbf{P}(l)$ is local polarization of cell l, computed according to the strategy presented in Appendix A.

In principle, the local susceptibility $\chi_{\alpha\beta}(l)$ can be computed from a linear-response fluctuation formula analogous to Eq. (B.5). However, $\mathbf{P}_l$ being a local quantity, collecting sufficient statistics for is very costly computationally, and thus we adopt a different approach. However, since $\mathbf{P}_l$ is a local quantity, collecting sufficient statistics is very expensivecomputationally and therefore, we take a different approach. To compute the local response, it is more practical to perform additional calculations in which the action of a small external electric field $\boldsymbol{\mathcal{E}}^{ext}$ is explicitly simulated. Within the linear regime, we approximate the $\chi_{\alpha\beta}(l)$ as

$$\chi_{\alpha\beta}(l) \approx \frac{1}{\epsilon_0}\frac{\langle P_\alpha(l;+\mathcal{E}^{\text{ext}}_\beta)\rangle - \langle P_\alpha(l;-\mathcal{E}^{\text{ext}}_\beta)\rangle}{2\mathcal{E}^{\text{ext}}_\beta}\ , \tag{C.2}$$

where we compare the result of applying small positive and negative fields to better extract

the linear part of the response.

Appendix D

Topological properties

The topological character of the dipole order in the ND multidomain configuration can be characterized by a so-called *topological charge* given by [66, 69]

$$Q = \int q(x,y)dxdy \ , \tag{D.1}$$

where the Pontryagin density $q(x,y)$ is given by

$$q(x,y) = \frac{1}{4\pi}\mathbf{u}\cdot(\partial_x\mathbf{u}\times\partial_y\mathbf{u}) \ . \tag{D.2}$$

Here $\mathbf{u} = \mathbf{u}(x,y)$ is the normalized polarization field in a plane.

To obtain $\mathbf{u}(x,y)$ from our simulations, we compute the local polarization centered in the A atom following the strategy presented in Appendix A. Then, we define $\mathbf{u}(x,y) = \mathbf{P}_l/|\mathbf{P}_l|$, where the (x,y) point coincides with the position of the A atom in the l cell. Thus, we effectively coarse-grain the ideally continuum field $\mathbf{u}(x,y)$. Finally, for the calculation of the derivatives in Eq. (D.2), and the integral in Eq. (D.1) itself, we find it useful to employ the numerical interpolation scheme proposed in Refs. [105, 106].

Finally, to better characterize our topological solutions with $Q = +1$, we introduce the quantity

$$S_\alpha = \frac{1}{Q}\int r_\alpha q(x,y)dxdy \ , \tag{D.3}$$

designed to track the skyrmion center [107, 108]. Here, $\alpha = x, y$ and $r_x = x$, $r_y = y$.